NUREG/IA-0220

International Agreement Report

Quantitative Code Assessment with Fast Fourier Transform Based Method Improved by Signal Mirroring

Prepared by:
A. Prošek, B. Mavko

Jožef Stefan Institute
Jamova cesta 39
SI-1000 Ljubljana, Slovenia

A. Calvo, NRC Project Manager

Office of Nuclear Regulatory Research
U.S. Nuclear Regulatory Commission
Washington, DC 20555-0001

December 2009

Prepared as part of
The Agreement on Research Participation and Technical Exchange
Under the Thermal-Hydraulic Code Applications and Maintenance Program (CAMP)

Published by
U.S. Nuclear Regulatory Commission

AVAILABILITY OF REFERENCE MATERIALS IN NRC PUBLICATIONS

NRC Reference Material

As of November 1999, you may electronically access NUREG-series publications and other NRC records at NRC's Public Electronic Reading Room at http://www.nrc.gov/reading-rm.html. Publicly released records include, to name a few, NUREG-series publications; *Federal Register* notices; applicant, licensee, and vendor documents and correspondence; NRC correspondence and internal memoranda; bulletins and information notices; inspection and investigative reports; licensee event reports; and Commission papers and their attachments.

NRC publications in the NUREG series, NRC regulations, and *Title 10, Energy*, in the Code of *Federal Regulations* may also be purchased from one of these two sources.

1. The Superintendent of Documents
   U.S. Government Printing Office
   Mail Stop SSOP
   Washington, DC 20402-0001
   Internet: bookstore.gpo.gov
   Telephone: 202-512-1800
   Fax: 202-512-2250
2. The National Technical Information Service
   Springfield, VA 22161-0002
   www.ntis.gov
   1-800-553-6847 or, locally, 703-605-6000

A single copy of each NRC draft report for comment is available free, to the extent of supply, upon written request as follows:

Address: Office of the Chief Information Officer,
Reproduction and Distribution
Services Section
U.S. Nuclear Regulatory Commission
Washington, DC 20555-0001
E-mail: DISTRIBUTION@nrc.gov
Facsimile: 301-415-2289

Some publications in the NUREG series that are posted at NRC's Web site address http://www.nrc.gov/reading-rm/doc-collections/nuregs are updated periodically and may differ from the last printed version. Although references to material found on a Web site bear the date the material was accessed, the material available on the date cited may subsequently be removed from the site.

Non-NRC Reference Material

Documents available from public and special technical libraries include all open literature items, such as books, journal articles, and transactions, *Federal Register* notices, Federal and State legislation, and congressional reports. Such documents as theses, dissertations, foreign reports and translations, and non-NRC conference proceedings may be purchased from their sponsoring organization.

Copies of industry codes and standards used in a substantive manner in the NRC regulatory process are maintained at—

The NRC Technical Library
Two White Flint North
11545 Rockville Pike
Rockville, MD 20852-2738

These standards are available in the library for reference use by the public. Codes and standards are usually copyrighted and may be purchased from the originating organization or, if they are American National Standards, from—

American National Standards Institute
11 West 42nd Street
New York, NY 10036-8002
www.ansi.org
212-642-4900

Legally binding regulatory requirements are stated only in laws; NRC regulations; licenses, including technical specifications; or orders, not in NUREG-series publications. The views expressed in contractor-prepared publications in this series are not necessarily those of the NRC.

The NUREG series comprises (1) technical and administrative reports and books prepared by the staff (NUREG–XXXX) or agency contractors (NUREG/CR–XXXX), (2) proceedings of conferences (NUREG/CP–XXXX), (3) reports resulting from international agreements (NUREG/IA–XXXX), (4) brochures (NUREG/BR–XXXX), and (5) compilations of legal decisions and orders of the Commission and Atomic and Safety Licensing Boards and of Directors' decisions under Section 2.206 of NRC's regulations (NUREG–0750).

DISCLAIMER: This report was prepared as an account of work sponsored by an agency of the U.S. Government. Neither the U.S. Government nor any agency thereof, nor any employee, makes any warranty, expressed or implied, or assumes any legal liability or responsibility for any third party=s use, or the results of such use, of any information, apparatus, product, or process disclosed in this publication, or represents that its use by such third party would not infringe privately owned rights.

NUREG/IA-0220

Quantitative Code Assessment with Fast Fourier Transform Based Method Improved by Signal Mirroring

Manuscript Completed: November 2007
Date Published: November 2009

Prepared by: Andrej Prošek, Borut Mavko

Jožef Stefan Institute
Jamova cesta 39
SI-1000 Ljubljana, Slovenia

A. Calvo, NRC Project Manager

Prepared as part of
The Agreement on Research Participation and Technical Exchange
Under the Thermal-Hydraulic Code Applications and Maintenance Program (CAMP)

Office
U.S. Nuclear Regulatory Commission
Washington, DC 20555-0001

ABSTRACT

In recent years, the number of quantitative comparisons between experimental data and calculated data in the area of nuclear technology has increased. The fast Fourier transform based method (FFTBM) is the tool most widely used to quantify the accuracy of thermal-hydraulic code calculations, which are continuing to improve. However, in preliminary applications of the original FFTBM to a severe accident test, the need for further optimization became evident. Analysts observed that FFTBM favors certain trends (e.g., monotonic increasing function). Thus, the purpose of the present study was to improve this aspect of FFTBM. Improvement was achieved by signal mirroring. Among other improvements, an index for the detection of the time shift between the compared signals was proposed. For the demonstration of improved FFTBM by signal mirroring, the analysis used the Loss of Fluid Test (LOFT) L2-5 test (large-break loss-of-coolant accident). Both qualitative and quantitative analyses were performed, and the conclusions about the quality of reference calculations were compared with those of the Best-Estimate Methods Uncertainty and Sensitivity Evaluation (BEMUSE). The results show that, with improved FFTBM, the analyst can achieve a true picture of the contribution of each discrepancy to the accuracy as judged by FFTBM. Analysis that considers the improved FFTBM tool as a “black box” obtains optimal information, which greatly aids the analyst in making a final judgment about the calculation. “Black box” here is meant that no information of the curve shape is input by the user to the FFTBM tool. The easy-to-use method is best suited to the automated comparison of several calculations of the same test.

CONTENTS

Page

ABSTRACT ..... **iii**

ACKNOWLEDGMENTS ..... **viii**

ABBREVIATIONS ..... **ix**

1. INTRODUCTION **1**

2. COMPLEX REPRESENTATION OF SINUSOIDS **3**

3. FOURIER TRANSFORM OF DISCRETELY SAMPLED DATA **5**
3.1 Discrete Fourier Transform 6
3.2 Fast Fourier Transform for Computing Discrete Fourier Transform 7

4. DESCRIPTION OF ORIGINAL FAST FOURIER TRANSFORM BASED METHOD **9**
4.1 Input Parameters for Fast Fourier Transform 9
4.2 Average Amplitude and Weighted Frequency 10
4.3 Accuracy of Code Calculation 10
4.4 Methodology for Quantifying Code Accuracy 12

5. DESCRIPTION OF EXTENDED ORIGINAL FAST FOURIER TRANSFORM BASED METHOD **13**
5.1 New Proposed Accuracy Measures 13
5.2 Time-Dependent Accuracy Measures 13

6. DESCRIPTION OF FAST FOURIER TRANSFORM BASED METHOD IMPROVED BY SIGNAL MIRRORING **15**
6.1 Signal Mirroring 15
6.2 Calculation of Average Amplitude by Signal Mirroring 16

7. DEMONSTRATION APPLICATION OF THE FAST FOURIER TRANSFORM BASED METHOD IMPROVED BY SIGNAL MIRRORING **19**
7.1 Facility and Test Description 19
7.2 Qualitative Assessment of the Calculations 19
7.3 Quantitative Assessment of the Calculations 21
7.4 Criterion for Using Moving Average 54
7.5 Comparison of Fast Fourier Transform Based Method and Automated Code Assessment Program 56
7.6 Correction Factors 57
7.7 Discussion of the Results 58

8. CONCLUSIONS **61**

9. REFERENCES **63**

Appendices

Page

A. Accuracy Measures for L2-5 Test in Time Interval 0–100 seconds..... A-1

Figures

1. Representation of complex numbers.....3
2. Different signals composed from the original LOFT L2-5 test pressurizer pressure signal....15
3. Intact loop pressure in hot leg (P1) in two different time intervals.....28
4. Intact loop pressure in hot leg (P1)—(a) time trends, (b) AA, (c) AA_m.....29
5. SG pressure, secondary side (P2)—(a) time trends, (b) AA, (c) AA_m 30
6. Accumulator A pressure (P3)—(a) time trends, (b) AA, (c) AA_m 31
7. Pressurizer pressure (P4)—(a) time trends, (b) AA, (c) AA_m.....32
8. Core inlet fluid temperature (P5)—(a) time trends, (b) AA, (c) AA_m 33
9. Core outlet fluid temperature (P6)—(a) time trends, (b) AA, (c) AA_m 34
10. Upper head fluid temperature (P7)—(a) time trends, (b) AA, (c) AA_m.....35
11. SG DC bottom fluid temperature (P8)—(a) time trends, (b) AA, (c) AA_m 36
12. Break flow rate in cold leg (P9)—(a) time trends, (b) AA, (c) AA_m 37
13. Integrated break flow rate in cold leg (P9int)—(a) time trends, (b) AA, (c) AA_m.....38
14. Break flow rate in hot leg (P10)—(a) time trends, (b) AA, (c) AA_m.....39
15. Integrated break flow rate in hot leg (P10int)—(a) time trends, (b) AA, (c) AA_m 40
16. ECCS integral break flow rate (P11)—(a) time trends, (b) AA, (c) AA_m 41
17. Primary side total mass (P12)—(a) time trends, (b) AA, (c) AA_m 42
18. SG pressure drop—UT PS (P13)—(a) time trends, (b) AA, (c) AA_m.....43
19. Primary pump pressure drop (P14)—(a) time trends, (b) AA, (c) AA_m.....44
20. Rod surface temperature in hot rod in hot channel (zone 4) at 2/3 core.....45
21. Rod surface temperature in average rod in average channel (zone 2) at bottom level (P18)—(a) time trends, (b) AA, (c) AA_m.....46
22. Rod surface temperature in average rod in average channel (zone 2) at 2/3 core height (P19)—(a) time trends, (b) AA, (c) AA_m 47
23. Rod surface temperature in average rod in average channel (zone 2) at top level (P20)—(a) time trends, (b) AA, (c) AA_m 48
24. Total accuracy trend obtained with original FFTBM.....49
25. Total accuracy trend obtained with FFTBM improved by signal mirroring 49
26. Time shift of break flow rates 53
27. Accuracy trends for SG pressure drop—UT PS using moving average for the experimental signal.....55
28. Time trends for SG pressure drop—UT PS for initial 5 seconds.....55

Tables

Page

1. Weighting Factor Components for the Analyzed Quantities (Ref. 5) 12
2. The Sum of Amplitudes of Signals Shown in Figure 2 16
3. Participants Performing Calculations 22
4. Variables Used in the BEMUSE Qualitative Analysis 23
5. Additional Derived Variables Available for Quantitative Assessment 23
6. Masses for Mass Balance Verification 26
7. New Accuracy Measures Obtained with Extended Original FFTBM 51
8. New Accuracy Measures Obtained with FFTBM Improved 51
9. Accuracy Contribution from Non-Rod Surface Temperature Variables and Contribution from Rod Surface Temperature Variables 53
10. Average SG Pressure Drops in Time Interval 15–120 Seconds 54
11. Comparison of FFTBM and ACAP Figures of Merit for Pressurizer Pressure (P4) in Time Interval 0–119.5 Seconds 56
12. Comparison of FFTBM and ACAP Figures of Merit for Rod Surface Temperature in the Hot Rod in the Middle of the Core (P16) in Time Interval 0–119.5 Seconds 57
13. Correction Factors for Accuracy Judgment by Original FFTBM 58

ACKNOWLEDGMENTS

The authors acknowledge the support of the Ministry of Higher Education, Science and Technology of the Republic of Slovenia within the program P2-0026 and the research projects J2-6542 and J2-6565. We especially thank our colleague Dr. Matjaž Leskovar for his fruitful ideas and suggestions regarding development of the fast Fourier transform based method (FFTBM) improved by signal mirroring. Finally, we thank the University of Pisa for providing the data and inviting us to perform this analysis.

ABBREVIATIONS

AA	average amplitude
ACAP	Automated Code Assessment Program
ATHLET	Analyses of Thermohydraulics in Leaks and Transients
BEMUSE	Best-Estimate Methods Uncertainty and Sensitivity Evaluation
CATHARE	Code for Analysis of THermalhydraulics during an Accident of Reactor and safety Evaluation
CEA	Commissariat à l'Energie Atomique
CSNI	Committee on the Safety of Nuclear Installations
CWT	continuous wavelet transform
DC	downcomer
DFFT	D'Auria fast Fourier transform
DFT	discrete Fourier transform
DP	differential pressure
ECCS	emergency core cooling system
EDO	Experimental Design Office
FFT	fast Fourier transform
FFTBM	fast Fourier transform based method
GID	EDO "Gidropress"
GRS	Gesellschaft für Anlagen- und Reaktor Sicherheit (GRS) mbH
HPIS	high-pressure injection system
I	time shift indicator
IAEA	International Atomic Energy Agency
IRSN	Institut de Radioprotection et de Sûreté Nucléaire
ISP	International Standard Problem
JNES	Japan Nuclear Energy Safety
JSI	Jožef Stefan Institute
K	acceptability factor
K	kelvin
KAERI	Korea Atomic Energy Research Institute
KFKI	Központi Fizikai Kutató Intézet
kg	kilogram

KINS	Korea Institute of Nuclear Safety
kPa	kilopascal
LOCA	loss-of-coolant accident
LOFT	loss-of-fluid test
LPIS	low-pressure injection system
MARS	Multi-dimensional Analysis of Reactor Safety
MPa	megapascal
MSE	mean square error
MWt	megawatt thermal
N	number of points
ND	number of discrepancies
NRI	Nuclear Research Institute
PCT	peak cladding temperature
PS	primary system
PSI	Paul Scherrer Institute
PWR	pressurized-water reactor
RELAP	Reactor Excursion and Leak Analysis Program
RTA	relevant thermal-hydraulic aspect
s	second
SG	steam generator
SPE	standard problem exercise
TAEK	Türkiye Atom Enerjisi Kurumu
TECH	EDO “Gidropress” code used for large break loss-of-coolant accidents
TRACE	TRAC/RELAP Advanced Computational Engine
TRAC-P	Transient Reactor Analysis Code - Pressurized
UPC	Universitat Politècnica de Catalunya
UPI	University of Pisa
UT	U-tube
VA	variable accuracy
WF	weighted frequency
XCC	cross-correlation coefficient

Subscripts

c	critical

cal	calculated
cut	cut-off
exp	experimental
fix	fixed
i	ith variable
m	mirroring
ma	moving average
max	maximal, maximum
min	minimal
mir	mirrored
norm	normalization
pr	primary pressure
s	sampling
saf	safety
tot	total
var	variable

Superscripts

M	magnitude information of the signal

1. INTRODUCTION

For years, the fast Fourier transform based method (FFTBM) has been used to quantify the accuracy of code calculations. The FFTBM shows the discrepancies between measurements and predictions (accuracy quantification) in the frequency domain. It assists in determining how to conduct objective comparison and identifying improvements needed in the input model.

Recently, an initiative to reduce the uncertainties in severe accident safety issues was started. Generally, the error made in predicting plant behavior is called “uncertainty,” while the discrepancies between measured and calculated trends related to experimental facilities are termed “the accuracy of the prediction.” When FFTBM was applied to the severe accident International Standard Problem (ISP)-46 (Phebus FPT1) (Ref. 1), the need to optimize FFTBM was identified. Specifically, analysts observed that when calculating the accuracy trend, the accuracy changes greatly when the experimental signal sharply increases or decreases (e.g., triangular shape of cladding temperature). When the signal starts to return to its previous value, the accuracy also follows this trend. It is not logical that the still-present discrepancy decreases the accuracy instead of increasing it. This problem was not evident when applying FFTBM to a few time windows and/or time intervals. It was recognized only after the development of FFTBM with the capability to calculate time-dependent accuracy (Ref. 2). Also, analysts found that for monotonically increasing or decreasing functions, the original FFTBM is normally highly accurate. The purpose of this study was, therefore, to improve this aspect of the FFTBM, which is caused by the edge effect. Namely, if the values of the first and last data point differ, then a step function is present in the periodically extended time signal. This step function creates several harmonic components in the frequency domain, thus increasing the sum of the amplitudes. The problem of the edge effect was resolved by signal mirroring.

Section 2 presents the complex representation of the sinusoids. The fast Fourier transform (FFT) is based on complex numbers. As the data are always discrete, the Fourier transform of discretely sampled data is described in Section 3. Readers familiar with Fourier transform can skip Sections 2 and 3, which are important to understanding how FFTBM works. Section 4 describes the original FFTBM, which, as its name suggests, was based on FFT. The Jožef Stefan Institute (JSI) has used the FFTBM since 1994 and was also involved in its testing. JSI performed some later extensions of the original FFTBM, as described in Section 5. Section 6 describes the FFTBM improved by signal mirroring, which eliminates the edge effect between the first and last data point. Finally, Section 7 describes the results of the demonstration application of FFTBM improved by signal mirroring to the loss-of-fluid test (LOFT) L2-5 test, and Section 8 presents the report’s conclusions.

2. COMPLEX REPRESENTATION OF SINUSOIDS

As shown in Figure 1, a complex number C can be expressed in rectangular notation $\mathrm{C} = a + ib$ or polar notation $\mathrm{C} = Me^{i\theta}$.

In rectangular notation, the complex numbers are represented by locations in a two-dimensional plane called the "complex plane." As shown in Figure 1(a), the horizontal axis of the complex plane is the real part of the complex number, and the vertical axis is the imaginary part. The mathematical notation for separating a complex number into its real and imaginary parts uses the operators *Re*() and *Im*().

Complex numbers can also be expressed in polar notation as shown in Figure 1(b). The magnitude *M* is the length of the vector starting at the origin and ending at the complex point, while the phase angle θ is measured between the vector and the positive x-axis. The following equations can convert complex numbers between rectangular and polar notation:

$$M = \sqrt{(Re\,\mathrm{C})^2 + (Im\,\mathrm{C})^2}, \quad \theta = \arctan\left[\frac{Im\,\mathrm{C}}{Re\,\mathrm{C}}\right] \qquad . 1)$$

$$Re\,\mathrm{C} = M\cos(\theta), \quad Im\,\mathrm{C} = M\sin(\theta). \qquad . 2)$$

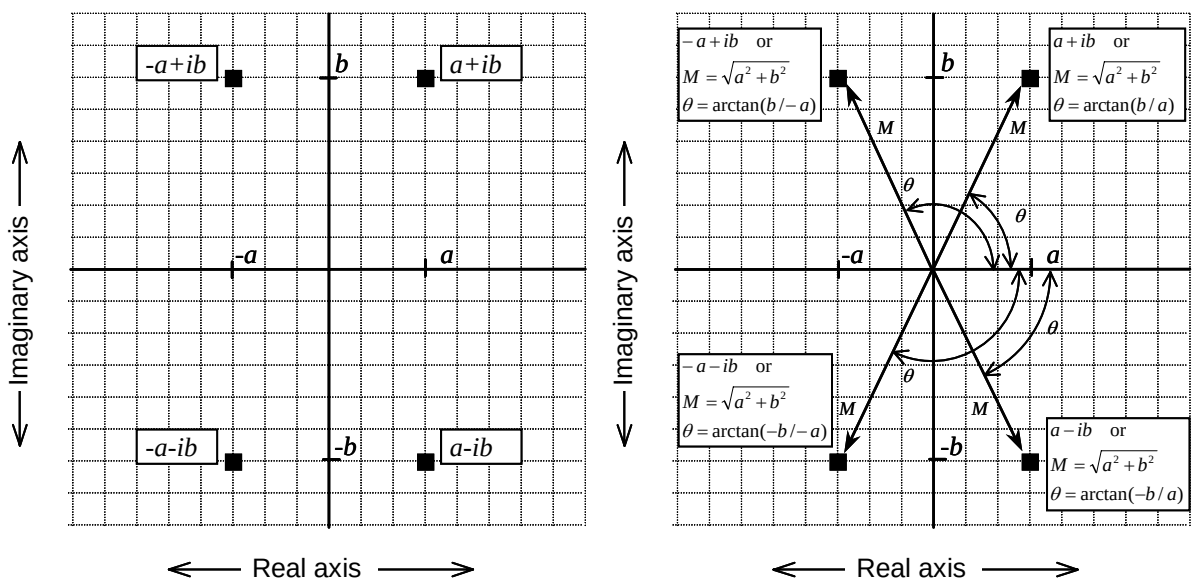

(a) Complex numbers in rectangular form (b) Complex numbers in polar form

Figure 1 Representation of complex numbers

Beginning with a proper complex number $a + ib$ and applying Eq. 2 obtains the following:

$$a + ib = M(\cos\theta + i\sin\theta). \qquad . 3)$$

The expression on the left is the proper rectangular description of the complex number, while the expression on the right is the proper polar description. One of the most important equations in complex mathematics is the Euler's relation:

$$e^{ix} = \cos(x) + i\sin(x). \qquad (4)$$

Rewriting Eq. 3 using the Euler's relation results in the most common way of expressing a complex number in polar notation (i.e., with a complex exponent):

$$a + ib = Me^{i\theta} \qquad (5)$$

This exponential form has the advantage of being convenient for mathematical operations, since it is very simple to multiply and divide complex numbers written in such a form:

$$M_1 e^{i\theta_1} M_2 e^{i\theta_2} = M_1 M_2 e^{i(\theta_1+\theta_2)}, \qquad (6)$$

$$\frac{M_1 e^{i\theta_1}}{M_2 e^{i\theta_2}} = \frac{M_1}{M_2} e^{i(\theta_1-\theta_2)}. \qquad (7)$$

With complex numbers, sine and cosine waves can be represented in a compact way. The conventional way of representing a sinusoid is $M\cos(\omega t - \varphi)$ in polar notation and $A\cos(\omega t) + B\sin(\omega t)$ in rectangular notation, where $A = M\cos(\varphi)$, $B = M\sin(\varphi)$, $M = \left(A^2 + B^2\right)^{1/2}$ and $\varphi = \arctan(B/A)$. Since two parameters are required to represent a single sinusoid (i.e., *A* and *B*, or *M* and φ), the use of complex numbers to represent these important waveforms is a natural solution. Using substitution, the change from the conventional sinusoid representation to a complex number is straightforward. In rectangular form, the substitution is

$$\underset{(\textit{conventional representation})}{A\cos(\omega t) + B\sin(\omega t)} \quad \rightleftarrows \quad \underset{(\textit{complex number})}{a + ib}, \qquad (8)$$

where $A \rightleftarrows a$ *and* $B \rightleftarrows b$. In words, the amplitude of the cosine wave becomes the real part of the complex number, and the sine wave's amplitude becomes the imaginary part. It is important to understand that this is not an equation, but merely a way of letting a complex number represent a sinusoid. This substitution also can be applied in polar form:

$$\underset{(\textit{conventional representation})}{M\cos(\omega t - \varphi)} \quad \rightleftarrows \quad \underset{(\textit{complex number})}{Me^{i\theta}}, \qquad (9)$$

where $M \rightleftarrows M$ and $\varphi \rightleftarrows \theta$. In words, the polar notation substitution leaves the magnitude and the phase angle the same.

3. FOURIER TRANSFORM OF DISCRETELY SAMPLED DATA

A physical process can be described either in the *time domain* as a function of time $F(t)$ or in the *frequency domain* as a function of frequency $\tilde{F}(f)$ (generally a complex number). For many purposes, it is useful to think of $F(t)$ and $F(f)$ as being two different representations of the same function, which indeed they are. One switches between these two representations by means of the Fourier transform equations:

$$\begin{aligned} \tilde{F}(f) &= \int_{-\infty}^{\infty} F(t) e^{-2\pi i f t} dt, \\ F(t) &= \int_{-\infty}^{\infty} \tilde{F}(f) e^{2\pi i f t} df. \end{aligned} \qquad (10)$$

If the angular frequency ω is used instead of the frequency f, Eq. 10 looks like:

$$\begin{aligned} \tilde{F}(\omega) &= \int_{-\infty}^{\infty} F(t) e^{-i\omega t} dt, \\ F(t) &= \frac{1}{2\pi} \int_{-\infty}^{\infty} \tilde{F}(\omega) e^{i\omega t} d\omega, \end{aligned} \qquad (11)$$

where the following relation was considered:

$$\omega \equiv 2\pi f \qquad H(\omega) = H(f)\big|_{f=\omega/2\pi}. \qquad (12)$$

There are fewer factors of 2π to remember if the Fourier transform is written as a function of f, especially in the case of discretely sampled data. In the most common situation, the function $F(t)$ is sampled at evenly spaced intervals in time. Suppose that there are N consecutive sampled values

$$F_k \equiv F(t_k), \quad t_k \equiv k\tau, \quad k = 0, 1, 2, \ldots, N-1, \qquad (13)$$

with the sampling interval τ. For any sampling interval τ, there is also a special frequency f_c, called the Nyquist critical frequency, given by:

$$f_c \equiv \frac{1}{2\tau}. \qquad (14)$$

The Nyquist critical frequency (Ref. 3) is important for two related, but distinct reasons: the sampling theorem and aliasing. The sampling theorem states the conditions under which the samples of a signal (e.g., a function of time) can be used to reconstruct the signal perfectly: “When sampling a bandlimited signal (e.g., through analog to digital conversion) the sampling frequency must be greater than twice the signal’s bandwidth in order to be able to reconstruct the original perfectly from the sampled version.” Aliasing is an effect that causes different continuous signals to become indistinguishable (or to become aliases of one another) when sampled. When this happens, the original signal cannot be uniquely reconstructed from the sampled signal. Critical sampling of a sine wave is two sample points per cycle.

3.1 Discrete Fourier Transform

The Fourier transform of a function can be estimated from a finite number of its sampled points. With N numbers of input, the method, evidently, should be able to produce no more than N independent numbers of output. So, instead of estimating the Fourier transform $\tilde{F}(f)$ at continuous values of f in the range $-f_c$ to f_c, estimates should be made only at discrete values:

$$f_n \equiv \frac{n}{N\tau}, \quad n = -\frac{N}{2},\ldots,\frac{N}{2}. \qquad (15)$$

As the two extreme values of n are equal, this reduces the count to N. The approximation of the integral in Eq. 10 by the discrete sum gives the following:

$$\tilde{F}(f_n) = \int_{-\infty}^{\infty} F(t) e^{-2\pi i f_n t} dt \approx \sum_{k=0}^{N-1} F_k e^{-2\pi i f_n t_k} \tau = \tau \sum_{k=0}^{N-1} F_k e^{-2\pi i k n / N}. \qquad (16)$$

The final summation in Eq. 16 is called the discrete Fourier transform (DFT) of the N points F_k. This is denoted by $\tilde{F}_n$:

$$\tilde{F}_n = \sum_{k=0}^{N-1} F_k e^{-2\pi i k n / N}. \qquad (17)$$

The relation in Eq. 16 between the DFT of a set of numbers and their continuous Fourier transform, when they are viewed as samples of a continuous function sampled at an interval τ, can be written as:

$$\tilde{F}(f_n) \approx \tau \tilde{F}_n. \qquad (18)$$

Until now, it has been assumed that the index n in Eq. 17 varies from $-N/2$ to $N/2$. However, it is evident that Eq. 17 is periodic in n, with period N. Therefore, $\tilde{F}_{-n} = \tilde{F}_{N-n}$ for $n = 1,2,\ldots$. With this conversion in mind, n and $\tilde{F}_n$ are allowed to vary from 0 to N-1 (i.e., one complete period). Then n and k (in F_k) vary exactly over the same range, so the mapping of N numbers into N numbers is manifest. When this convention is followed, the zero frequency corresponds to $n = 0$ and positive frequencies $0 < f < f_c$ correspond to values $1 < n < N/2 - 1$, while negative frequencies $-f_c < f < 0$ correspond to $N/2 + 1 < n < N - 1$. The value n = $N/2$ corresponds to both $f = f_c$ and $f = -f_c$. The following is the formula for the discrete inverse Fourier transform, which recovers the set of F_k's exactly from the $\tilde{F}_n$'s:

$$F_k = \frac{1}{N} \sum_{n=0}^{N-1} \tilde{F}_n e^{2\pi i k n / N}. \qquad (19)$$

The only differences between Eq. 19 and Eq. 17 are the changed sign in the exponent and the division of the expression by N. This means that a code for calculating DFTs can also, with slight modification, calculate the inverse transforms.

The complex transform $\tilde{F}_n$ from Eq. 17 written as a real transform is the following:

$$\mathrm{Re}(\tilde{F}_n) = \sum_{k=0}^{N-1} F_k \cos(2\pi kn / N), \qquad . 20)$$

$$\mathrm{Im}(\tilde{F}_n) = -\sum_{k=0}^{N-1} F_k \sin(2\pi kn / N), \qquad . 21)$$

where $\mathrm{Re}(\tilde{F}_n)$ and $\mathrm{Im}(\tilde{F}_n)$ are cosine and sine amplitudes in the following equation of the real inverse transform:

$$F_k = \frac{2}{N} \sum_{n=0}^{N-1} \left[\mathrm{Re}\left(\tilde{F}_n\right) \cos(2\pi kn / N) - \mathrm{Im}\left(\tilde{F}_n\right) \sin(2\pi kn / N) \right]. \qquad . 22)$$

For the calculation of the figure of merit presented in the next subsections, the absolute values of Fourier transforms are needed; these are the amplitudes (also called magnitudes). Using Eq. 1 produces:

$$\left|\tilde{F}_n\right| = \sqrt{\left(\mathrm{Re}(\tilde{F}_n)\right)^2 + \left(\mathrm{Im}(\tilde{F}_n)\right)^2}. \qquad . 23)$$

To make the (discrete) Fourier transform and inverse (discrete) Fourier transform equations undo each other, a scaling factor must be placed on one or the other equation. In the complex case, the scaling factors are 1/*N* for the discrete case or 1/2π for the continuous case. Since the real transforms do not use the negative frequencies, the scaling factors are twice as large: 2/*N* and 1/π. The above equations of the Fourier transform and its inverse may look different in other publications. The scaling factor multiplying the sum and the sign of the exponent are merely conventions and differ in some treatments. The only important things are that the forward and inverse DFTs have opposite-sign exponents and the product of their normalization factors is 1/*N*. This is the case in the original FFTBM algorithm described in Section 4, where the scaling factor 1/*N* for the complex transform is in front of the (discrete) Fourier transform equation. Using this convention, the zero frequency component represents the mean value of the time signal (in the opposite when not using the scaling factor 1/*N* in front, it would be the sum of the discrete points). Nevertheless, as the sums of the experiment and the difference signal amplitude spectra are divided, the scaling factor has no influence on the accuracy results but the amplitude spectrum changes with the scaling factor (the amplitude spectrum is the optional output of the FFTBM software, when it is needed for detailed analysis of the frequency spectrum).

3.2 Fast Fourier Transform for Computing Discrete Fourier Transform

The DFT can be computed with an algorithm called the FFT, which rapidly computes the DFT. For information on how FFT works, the reader should refer to the literature (Ref. 3).

4. DESCRIPTION OF ORIGINAL FAST FOURIER TRANSFORM BASED METHOD

The FFTBM was developed to identify discrepancies between measurements and predictions of thermal hydraulic codes.

4.1 Input Parameters for Fast Fourier Transform

To apply FFT, the function must be identified by a number of values that is a power with the base equal to 2 (this was a requirement for older FFT algorithms, such as the one used in the original FFTBM). Thus, if the number of points defining the function in the time domain is

$$N = 2^{m+1}, \qquad (24)$$

where m = 0, 1, 2,…, the FFT algorithm gives the transformed function defined in the frequency domain by $2^m + 1$ values corresponding to the frequencies

$$f_n = \frac{N}{T_d}, \qquad (n = 1,2,\ldots,2^m), \qquad (25)$$

where T_d is the transient time duration of the sampled signal.

To use FFTBM, the number of points must be selected for the FFT calculation. This is the same as selecting the sampling frequency. Since the FFT algorithm requires that functions are identified by a number of values (equally spaced), which is a power of 2, an interpolation to satisfy this requirement is necessary. On the other hand, the comparison of the experimental and the calculated signal implies that they have the same time scale. Normally, experimental data are sampled at a different frequency than are the calculated data. The interpolation results in discretely sampled experimental and calculated data at evenly spaced intervals in time (sampling interval). In FFT, the sampling frequency of interpolated data is used; therefore, for FFT, the sampling theorem must be fulfilled.

After selecting the number of points $N=2^{m+1}$, the maximum frequency of transformed functions by FFT is given by:

$$f_{\max} = \frac{f_s}{2} = \frac{1}{2\tau} = \frac{N}{2T_d} = \frac{2^{m+1}}{2T_d} = \frac{2^m}{T_d}, \qquad (26)$$

where T_d is the transient time duration of the sampled signal. The relation in Eq. 26 shows that the number of selected points is strictly connected to the sampling frequency of interpolated data. In the FFTBM algorithm, the minimum number of points is limited to 512. It was decided that, instead of the number of points, the input parameter for FFTBM is the fixed frequency f_{fix}. The number of points increases until f_{max} determined by Eq. 26 is greater than f_{fix} or until the maximum number of points allowed in the algorithm is reached. If f_{fix} for a given time interval of interpolated data gives a number of points lower than the number of experimental and/or

calculated data, some information could be lost. If f_{fix} is selected so that the number of points is too high, little new information is introduced.

The interpolation using a linear method changes the slope, but it was verified that this effect is negligible because these spurious frequencies are at higher frequencies having lower amplitudes than typical frequencies characterizing the signal. To filter this spurious contribution, the cut-off frequency (f_{cut}) was introduced as the second input parameter.

4.2 Average Amplitude and Weighted Frequency

The FFTBM shows the measurement-prediction discrepancies in the frequency domain. For the calculation of these discrepancies, the experimental signal ($F_{exp}(t)$) and the error function $\Delta F(t)$ (difference signal) are needed. The error function in the time domain is defined as

$$\Delta F(t) = F_{cal}(t) - F_{\exp}(t), \qquad (27)$$

where $F_{cal}(t)$ is the calculated signal. The code accuracy quantification for an individual calculated variable is based on amplitudes of the discrete experimental and error signal obtained by FFT at frequencies f_n (see Eq. 25). These spectra of amplitudes are used for the calculation of the average amplitude (AA) that characterizes the code accuracy:

$$AA = \frac{\sum_{n=0}^{2^m} \left| \widetilde{\Delta F}(f_n) \right|}{\sum_{n=0}^{2^m} \left| \widetilde{F}_{\exp}(f_n) \right|}. \qquad (28)$$

A weighted frequency (WF) is defined as the sum of frequencies multiplied (weighted) by error function amplitudes, normalized to the sum of error function amplitudes:

$$\mathrm{WF} = \frac{\sum_{n=0}^{2^m} \left| \widetilde{\Delta F}(f_n) \right| \cdot f_n}{\sum_{n=0}^{2^m} \left| \widetilde{\Delta F}(f_n) \right|}. \qquad (29)$$

In the past, several applications calculated the values of WF (Ref. 4). However, no judgment was based on WF. As will be shown in Sections 5 and 6, only AA was used to derive the new accuracy measures.

4.3 Accuracy of Code Calculation

The overall picture of the accuracy of a given code calculation is obtained by defining average performance indices (i.e., the total weighted AA (total accuracy)):

$$AA_{tot} = \sum_{i=1}^{N_{var}} (AA)_i \cdot (w_f)_i \qquad . 30)$$

and the total WF

$$WF_{tot} = \sum_{i=1}^{N_{var}} (WF)_i \cdot (w_f)_i \qquad . 31)$$

with

$$\sum_{i=1}^{N_{var}} (w_f)_i = 1, \qquad . 32)$$

where N_{var} is the number of the variables analyzed, and $(AA)_i$, $(WF)_i$ and $(w_f)_i$ are the AA, the WF, and the weighting factors for the *i*th analyzed variable, respectively. Each $(w_f)_i$ accounts for the experimental accuracy, the safety relevance of particular variables, and its relevance with respect to pressure (Ref. 5).

Experimental accuracy $(w_{exp})_i$: Experimental trends of thermal-hydraulic variables are characterized by uncertainty because of intrinsic characteristics of the instruments, the measurement method, and different evaluation procedures used to compare experimental measures and the code predictions.

Safety relevance $(w_{saf})_i$: Higher importance is attributed to the accuracy of those calculated variables that are relevant for safety and design (such as pressure and peak clad temperature).

Primary pressure normalization $(w_{norm})_i$: This contribution is given by a factor that normalizes the AA value calculated for the selected variables with respect to the AA value calculated for the primary pressure. This factor has been introduced to consider the physical relations existing between different quantities (i.e., fluid temperature and pressure in case of saturated blowdown must be characterized by the same order of error).

The weighting factor for the *i*th variable is therefore defined as:

$$(w_f)_i = \frac{(w_{exp})_i \cdot (w_{saf})_i \cdot (w_{norm})_i}{\sum_{i=1}^{N_{var}} (w_{exp})_i \cdot (w_{saf})_i \cdot (w_{norm})_i}, \qquad . 33)$$

where w_{exp} is the contribution related to the experimental accuracy, w_{saf} is the contribution that expresses the safety relevance, and w_{norm} is the contribution of primary pressure normalization. Table 1 shows the weighting factors.

The definition of weighting factors introduces a degree of engineering judgment in the development of the FFTBM method. In the later applications of FFTBM, these weighting factors have been fixed. The weights must remain unchanged during each comparison between code results and experimental data concerning the same class of transient.

Table 1 Weighting Factor Components for the Analyzed Quantities (Ref. 5)

Quantity	w_{exp}	w_{saf}	w_{norm}
Pressure drops	0.7	0.7	0.5
Mass inventories	0.8	0.9	0.9
Flow rates	0.5	0.8	0.5
Primary pressure	1.0	1.0	1.0
Secondary pressure	1.0	0.6	1.1
Fluid temperatures	0.8	0.8	2.4
Clad temperatures	0.9	1.0	1.2
Collapsed levels	0.8	0.9	0.6
Core power	0.8	0.8	0.5

4.4 Methodology for Quantifying Code Accuracy

Given a qualified user and qualified nodalization scheme, the code assessment process involves three steps: (1) selection of an experiment from the Committee on the Safety of Nuclear Installations (CSNI) validation matrices (Ref. 6) (or a plant transient), (2) qualitative assessment, and (3) quantitative assessment. The steps in the methodology for quantifying code accuracy, described in more in detail in (Ref. 4), are subdivisions of the scenario into "phenomenological windows"; for each phenomenological window, the methodology requires specification of key phenomena that are distinctive for this class of transients (for example, break flow), identification of the relevant thermal-hydraulic aspects (RTAs) which are particular to each transient (these are events or phenomena consequent to the physical process, such as subcooled blowdown), and selection of variables characterizing the RTAs (for example. average break flow); qualitative assessment of obtained results can be done by visually comparing the experimental and calculated variables trends.

The qualitative assessment gives the first indications about the accuracy of the calculated predictions. The qualitative assessment phase is a necessary prerequisite for a subsequent quantitative phase. It is meaningless to perform this last phase through the FFTBM if any RTA is not predicted.

The quantitative assessment can be managed by applying the FFTBM. Normally. 20 to 25 variables are selected for the accuracy analysis. The most suitable factor for the definition of an acceptability criterion is the total average amplitude, AA_{tot}. With reference to the accuracy of a given calculation, the following acceptability criterion can be defined:

$$AA_{tot} < K, \qquad . 34)$$

where K is the acceptability factor valid for the whole transient and is set to K = 0.4. The previous studies showed the following:

- $AA_{tot} \leq 0.3$ characterizes very good code predictions.
- $0.3 < AA_{tot} \leq 0.5$ characterizes good code predictions.
- $0.5 < AA_{tot} \leq 0.7$ characterizes poor code predictions.
- $AA_{tot} > 0.7$ characterizes very poor code predictions.

In addition, the acceptability factor K = 0.1 has been fixed for the primary pressure, because of its importance.

5. DESCRIPTION OF EXTENDED ORIGINAL FAST FOURIER TRANSFORM BASED METHOD

Since the original FFTBM was developed, JSI has suggested a few improvements. These improvements are new proposed accuracy measures based on variable accuracy and number of discrepancies and the calculation of time-dependent accuracy measures.

5.1 New Proposed Accuracy Measures

The new accuracy measures were tested on IAEA-SPE-4 data (Ref. 7). Let the accuracy of the *i*th variable be

$$VA_i = AA_i \cdot (w_f)_i \cdot N_{\text{var}}, \qquad (35)$$

which shows what the total accuracy would be if all variables contribute to AA_{tot} to the same degree as the *i*th variable. By this definition, the criteria for $AA_{tot,}$ presented in Section 4.4, are also applicable to variable accuracy (VA), and they are even more appropriate than AA for variables, because with VA, the weights are already considered. Therefore, VA is applicable only in conjunction with the AA_{tot} calculation.

Based on VA, three new accuracy measures were proposed: the number of discrepancies (ND) in the calculation, the minimal variable accuracy VA_{min} (see Eq. 36), and the maximal variable accuracy VA_{max} (see Eq. 37). The accuracy is minimal when the value of the accuracy measure is maximal (AA = 0 indicates perfect agreement). The accuracy is maximal when the value of the accuracy measure is minimal. The ND indicates the number of variables with variable accuracy VA_i above the acceptability limit K = 0.4. The minimal variable accuracy is defined as

$$VA_{\min} = \max\{VA_i\};\ i = 1\, to\, N_{\text{var}} \qquad (36)$$

and maximal variable accuracy as

$$VA_{\max} = \min\{VA_i\};\ i = 1\, to\, N_{\text{var}}. \qquad (37)$$

The minimal variable accuracy also represents the hypothetical total accuracy combined from variables all having the same value of AA = VA_{min}. In this way, the variable accuracy can be compared to acceptability limits for AA_{tot}. If the value indicates a very poor prediction, the analyst must refer to the qualitative analysis and check whether the reason for the discrepancy is understood. If this value indicates a very good prediction, this means that all other selected variables are predicted to also be very good. When VA_{min} is below K = 0.4, then ND is 0, according to the definition.

5.2 Time-Dependent Accuracy Measures

The FFTBM requires the qualitative assessment and the subdivision of the transient into phenomenological windows. Normally, the accuracy analysis is performed for time windows and time intervals, where each phenomenological window represents one time window, while time

intervals start at the beginning of the transient and end at each phenomenological window end time.

Instead of a few phenomenological windows, a series of narrow windows (phases) is proposed (around 30 windows for a transient). This makes it possible to check the accuracy of each part of the transient and to measure the time dependency of accuracy. In the quantitative assessment with three to five phenomenological windows, only global trends are available. In the present analysis, the term “moving time window” means a set of equidistant narrow time windows as the transient progresses (like a moving chart strip). The term “increasing time interval” means a set of time intervals each increased for the duration of one narrow time window, where the last time interval is equal to the whole transient duration time. The moving time window shows instantaneous details of $\Delta F(t)$, and consequently, an overall judgment about accuracy cannot be made from it. Instead, the analyst has a picture of instantaneous discrepancies. An integral approach is needed to make an overall judgment about accuracy, and this is achieved by increasing the time interval, which also shows how the accuracy changes with time progression. These time-dependant accuracy measures clearly show when the largest total discrepancy occurs and its influence on total accuracy. They also show how the transient duration selected for the analysis influences the results.

6. DESCRIPTION OF FAST FOURIER TRANSFORM BASED METHOD IMPROVED BY SIGNAL MIRRORING

To make FFTBM applicable for all variables, signal mirroring is proposed to eliminate the edge effect in calculating AA.

6.1 Signal Mirroring

In the case of a function $F(t)$ where $0 \le t \le T_d$ and T_d is the transient time duration, its mirrored function is defined as $F_{mir}(t) = F(-t)$, where $-T_d \le t \le 0$. From these functions, a new function is composed which is symmetrical in regard to the y-axis: $F_m(t)$, where $-T_d \le t \le T_d$. By combining the original signal and its mirrored signal (signal mirroring), a signal without the edge between the first and the last data sample is obtained, which is called a "symmetrized signal." To explain this, Figure 2 shows different signals: the original signal (the LOFT L2-5 test measured intact loop hot leg pressure) together with the shifted original signal (Figure 2(a)), the mirrored original signal (Figure 2(b)), two periods of the original signal (Figure 2(c)), and the symmetrized signal composed from one period of the mirrored signal and one period of the original signal (Figure 2(d)). Only the symmetrized signal is without the edge when treating an aperiodic signal as one period of the periodic signal. The edge is not visible in the plotted signal when the signal is not shifted or not plotted as a periodic signal (see Figure 2(c)). However, in the performance of FFT, the aperiodic signal is treated as a periodic signal, and therefore the edge is part of the signal, which is not physical.

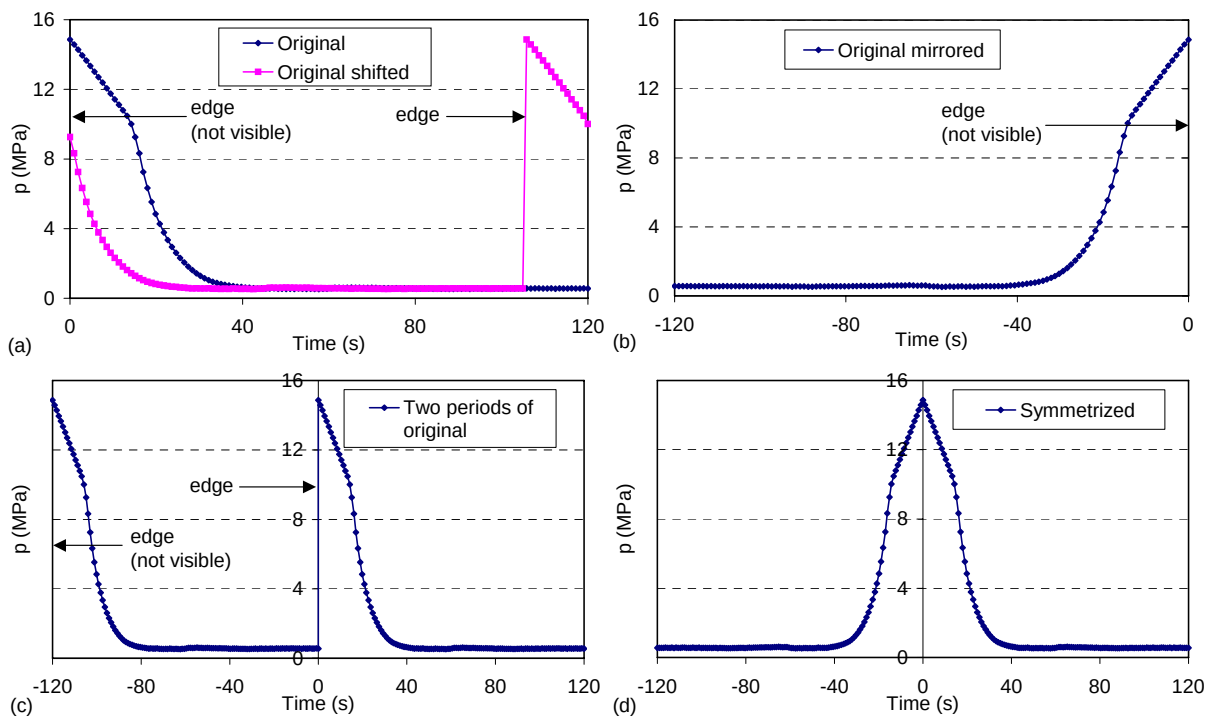

Figure 2 Different signals composed from the original LOFT L2-5 test pressurizer pressure signal

Table 2 shows that, in performance of the FFT, the sum of amplitudes of the original, the original with shift, and the mirrored signal are the same. The Fourier transform of two periods of the original signal is also the same. However, when making the Fourier transform of the symmetrized signal, the sum is less than in the case of the signals where the edge is present. In this way, the edge contribution to the sum can be seen. In this example, the difference in the sum of amplitudes is 9.585 ((25.871 - 16.286) = 9.585). This means that the sum of amplitudes of the experimental signal is 37 percent less when the edge effect is not considered, which increases the AA almost 59 percent. This means that all integral variables and variables dropping to zero value (power, primary pressure during a loss-of-coolant accident (LOCA), etc.) exhibit lower AA values because of the edge in the experimental signal. This also partly explains the generally very high accuracy of these variables compared to other variables in the past applications (Ref. 4).

The edge effect has a similar influence on the difference signal, with the difference that, in this case, the sum is in the numerator for AA calculation and the larger sum of the amplitudes means a larger AA.

Table 2 The Sum of Amplitudes of Signals Shown in Figure 2

Type of Signal	Sum of Amplitudes of the Fourier Transform
original signal	25.871
shifted original signal	25.871
mirrored signal	25.871
two periods of original signal*	25.871
symmetrized signal*	16.286

* The scaling factor 1/*N* is in the DFT equation in FFTBM, while in the case of the Microsoft Excel Fourier analysis, it is in the inverse Fourier analysis. Therefore, when using Microsoft Excel, analysts need to divide the values by the number of points used in order to obtain the same results as obtained by FFTBM.

As the edge effect is eliminated in both the experimental signal amplitude spectrum and in the difference signal amplitude spectrum, the new values of AA may be larger or smaller than D'Auria AA (Eq. (28) applied to original signals with no signal mirroring), depending on how the numerator and the denominator change. Nevertheless, the next section will show that the original FFTBM acceptance criteria for AA at the moment can remain in use and that AA based on mirroring provides a more objective quantitative measure. For calculating the total AA, the primary normalization factors were determined using the AAs with the edge effect. It seems that the primary pressure normalization weight partly compensates for the edge effect. Several calculations are needed to verify this hypothesis, but this is not the objective of this study. Finally, when variables are not equally important or the measurement accuracy is different, the importance (safety relevance in the area of nuclear safety) weighting factors and experimental accuracy factors can further be used for the primary system (PS) calculations.

6.2 Calculation of Average Amplitude by Signal Mirroring

For the calculation of the average amplitude by signal mirroring (AA_m), Eq. (28) is used for the calculation of AA, except that, instead of the original signal, the symmetrized signal is used. The reason to symmetrize the signal was to exclude the edge from the signal. The signal is automatically symmetrized in the program for the FFTBM improved by signal mirroring as is described in (Ref. 1).

As already mentioned, the edge has no physical meaning, but it causes FFT to produce harmonic components. By mirroring, the shapes of the experimental and error signal are symmetric and their spectra are different from the original signals spectra, mainly because they are without nonphysical edge frequency components. Because of different spectra, the sum of the amplitudes changes in both the numerator and the denominator of Eq. (28). For further use in distinguishing between the error and experimental signal edge contribution, two new definitions are introduced for the AA of the error and experimental signal, related to the numerator and denominator of Eq. (28):

$$AA_{err} = \frac{1}{2^m + 1} \sum_{n=0}^{2^m} \left| \tilde{\Delta} F(f_n) \right|, \tag{38}$$

$$AA_{\exp} = \frac{1}{2^m + 1} \sum_{n=0}^{2^m} \left| \tilde{F}_{\exp}(f_n) \right|. \tag{39}$$

When both the original and error signal are without the edge, in principle, different AA_{err} and $AA_{\exp}$ may be obtained by the original FFTBM and the FFTBM improved by signal mirroring. Indeed, AA and AA_m are slightly different measures if the signals are without an edge. The values obtained with the original FFTBM and improved FFTBM by signal mirroring are the same only for symmetrical original signals, but this is not really a deficiency of the proposed improved FFTBM, since it is important only that the method judges the accuracy realistically and that it is consistent within itself.

7. DEMONSTRATION APPLICATION OF THE FAST FOURIER TRANSFORM BASED METHOD IMPROVED BY SIGNAL MIRRORING

The FFTBM improved by signal mirroring was applied to calculations of the ISP-13 test performed in the BEMUSE project. These calculations were selected because they were part of an international activity and the number of calculations was large enough that one can readily see the relationship between variables and quantitative results. The objective of the ISP-13 test (LOFT L2-5 test) was to simulate a LOCA caused by a double-ended, off-shear guillotine cold leg rupture, coupled with a loss of offsite power in the nuclear LOFT test facility. The analysis assumed delayed initiation of the high-pressure injection system (HPIS) and the low-pressure injection system (LPIS) emergency core cooling system (ECCS) (Ref. 9).

7.1 Facility and Test Description

The LOFT Integral Test Facility is a scale model of a pressurized-water reactor (PWR). The facility is used to model the nuclear thermal-hydraulic phenomena that would take place in a PWR during a LOCA. The general philosophy in scaling coolant volumes and flow areas in LOFT was to use the ratio of the LOFT core (50 megawatts thermal (MWt)) to a typical light PWR core (3,000 MWt). For some components, this factor is not applied; however, it is used as extensively as practical. In general, components used in LOFT are similar in design to those of a PWR. Because of scaling and component design, the LOFT LOCA is expected to closely model a PWR LOCA. The LOFT ECCS, which simulates the ECCS of a commercial PWR, consists of two accumulators, an HPIS, and an LPIS.

The experiment was initiated by opening the quick-opening blowdown valves in the broken loop hot and cold legs. The reactor scrammed on low pressure at 0.24 ± 0.01 seconds. Following the reactor scram, the operators tripped the primary coolant pumps at 0.94 ± 0.01 seconds. Accumulator injection of ECCS to the intact loop cold leg began at 16.8 ± 0.1 seconds when the system pressure dropped below 4.2 megapascals (MPa). Delayed emergency core cooling injection from the HPIS and LPIS began at 23.90 ± 0.02 seconds and 37.32 ± 0.02 seconds, respectively. The fuel rod peak cladding temperature of 1,078 ± 13 kelvin (K) was attained at 28.47 ± 0.02 seconds. The accumulator emptied at 49.6 ± 0.01 seconds. The cladding was quenched at 65 ± 2 seconds, following the core reflood. The LPIS injection was stopped at 107.1 ± 0.4 seconds, at which point the experiment was considered complete.

In Phase II of the BEMUSE project, which is the reanalysis of the ISP-13 exercise and posttest calculation of the LOFT L2-5 test, 14 participants provided their calculations. The University of Pisa, the lead organization in Phase II, provided these calculations, together with experimental data. JSI performed an independent quantitative analysis.

7.2 Qualitative Assessment of the Calculations

All steps of qualitative analysis were performed in the framework of BEMUSE, Phase II (Ref. 10), and are briefly described below. The first part of the qualitative analysis entailed visual comparisons between experimental and calculated time trends, with four subjective judgments assigned (excellent, reasonable, minimal, and unqualified). Table 12 in the BEMUSE Phase II

Report (Ref. 10) shows the list of selected variables. Each participant presented detailed comments concerning judgment of the time trends. The unqualified mark was assigned to the steam generator (SG) secondary pressure of the Experimental Design Office (EDO) “Gidropress” (GID) calculation and the core inlet liquid temperature of the Korea Institute of Nuclear Safety (KINS) calculation.

Participants also concluded that a possible unqualified mark might be assigned for the core inlet liquid temperature calculation of Universitat Politècnica de Catalunya (UPC) because of the jump of about 100 K at about 40 seconds and the hot rod temperature calculation (zone 4, bottom level) of UPC because of the absence of dryout (not used in quantitative analysis).

For the purpose of this analysis, the above statements were again verified. Figures 4 through 23 show the plots for time trends. The SG secondary pressure of the GID calculation shown in Figure 5 oscillates significantly, which is not physical. Similarly, the core inlet liquid temperature of the KINS calculation shown in Figure 8 drops to values around 320 K (like the ECCS injection flow temperatures) after 20 seconds.

Table 13 of the BEMUSE Phase II Report (Ref. 10) presents the list of RTAs. The following are the most important considerations identified in Table 13:

- All participants overpredicted the integral break flow rate at 100 s;
- The time of pressurizer emptying was well predicted by each participant;
- All participants underpredicted the time of PCT except for GRS and KAERI;
- In general, the value of PCT was well calculated. The maximum differences with respect to the experimental value of 1,078 K have been obtained by NRI-2 (1250 K) and by KAERI (980 K);
- The upper plenum pressure behavior has been well predicted during all transients, except in correspondence of 20 s when GID, JNES, KINS, and TAEK underpredicted the value of about 1–2 MPa;
- As a consequence of the previous point, GID, JNES, KINS, and TAEK had an early accumulator injection;
- A good agreement has been obtained for the mass injected by the accumulator with the exception of KAERI which overpredicted by about 500 kg;
- The HPIS and LPIS behaviors (time, flow rates and injected masses) were well predicted by all participants, except for GRS for which, due to typing mistakes during the preparation of the input deck, the intervention times were imposed 5 s earlier than in the experiment;
- It shall be noted that experimental values of the primary system mass were not available.

This study verified the RTA considerations listed above through visual observation of Figures 4 through 23. The finding that Japan Nuclear Energy Safety (JNES) break flow integrals were overpredicted could not be verified because the break flow integral calculated by JNES shows

overprediction (see Table 13 of the BEMUSE Phase II Report (Ref. 10), while the JNES break flows in cold and hot leg (Figure 12 and Figure 14) are underpredicted. Section 7.3 and Table 6, which presents results of simple mass balance, give further details. The finding regarding pressurizer emptying was not verified as the time trend of pressurizer level was not available for quantitative analysis.

The consideration regarding PCT can be verified from Figure 20. The Nuclear Research Institute (NRI-M) (labeled NRI-2 in BEMUSE) calculated the highest peak cladding temperature (PCT), while the Korean Atomic Energy Research Institute (KAERI) and JNES calculated the two lowest values (980 K and 973 K, respectively). This means that, in addition to the NRI-M and KAERI calculations, the JNES calculation should be listed among the calculations that show maximum difference with respect to the experimental PCT value.

The upper plenum pressure was not used in quantitative analysis; however, the authors of this report verified that the experimental trend of upper plenum pressure found in data for sensitivity analysis is the same as the experimental hot leg pressure found in quantitative analysis. An examination of hot leg pressure in Figure 4 can verify that GID (GIDROPRESS in BEMUSE), KINS, JNES, and Türkiye Atom Enerjisi Kurumu (TAEK) calculations underpredicted the pressure by about 1 to 2 MPa at 15 seconds. The KAERI calculation is similarly underpredicted. Consequently, all of these five calculations have early accumulator injection, which is evident from the accumulator pressures shown in Figure 6. However, with the knowledge that total HPIS and LPIS injected flow until quenching was less than 200 kilograms (kg) and that the accumulator injection time ranged from 16.8 seconds to 49.6 seconds (Ref. 10), the ECCS integral flow shown in Figure 16 can be used to verify accumulator injection. When the accumulator stops injecting, the plotted lines of the ECCS integral break. At that time, the KAERI calculation shows the largest difference (around 500 kg). The TAEK calculation shows a similar difference. However, it is clear that the data for TAEK should be corrected (the initial value of mass at time 0 should be subtracted). The BEMUSE report (Ref. 10) shows the ECCS integral for TAEK correctly, while the authors plotted the data as received.

This study could not verify the qualitative considerations concerning HPIS and LPIS behavior. However, Figure 16 indicates that the injection by HPIS and LPIS 5 seconds earlier contributes little to the total ECCS mass injection as the accumulator was prevailing at that time. Figure 17 shows the PS mass. Because the BEMUSE Phase II report (Ref. 10) mentions that experimental ECCS integral flow rate and the PS mass are derived from a calculated quantity (experimental data were not available), no further analysis was made.

On the basis of the verification of qualitative evaluation of variables and RTA in BEMUSE Phase II, the quantitative analysis was performed. If strictly following the methodology, quantitative analysis should not be performed for two calculations with an unqualified mark for time trends. However, this report will show that FFTBM was able to detect such variables as the worst predictions.

7.3 Quantitative Assessment of the Calculations

In BEMUSE Phase II, quantitative assessment was performed with original FFTBM. For this report, quantitative assessment was performed using both the original FFTBM and FFTBM improved by signal mirroring. Although the results obtained from the assessment are not part of the BEMUSE final report, some interesting results were found by using the original FFTBM and FFTBM improved by signal mirroring and time-dependent analysis. Table 3 shows information

about the participants in the BEMUSE Phase II study. In total, 13 organizations performed 14 calculations using 6 different codes (9 different code versions). The code used most frequently was RELAP5/MOD3.3.

The time-dependent quantitative analysis was performed for an increasing time interval for each 5 seconds. For the accuracy quantification, all frequencies were used (f_{cut} higher than the maximum frequency was selected). Table 4 shows the variables used in the BEMUSE qualitative analysis. The present study's quantitative analysis used 18 out of 20 available variables to calculate total accuracy, in the same method used in BEMUSE Phase II (see Table 14 in the BEMUSE Phase II Report (Ref. 10)). Table 5 shows some additional variables. The quantitative analysis determined accuracy for the cold and hot leg integrated break flow. However, the calculation of total accuracy did not consider these variables.

Figures 4 through 23 show the results of the accuracy analysis. On each figure is shown the variable (a), D'Auria AA (b), and AA by signal mirroring (c). All AAs are calculated as a function of time. In this way, the contribution of each discrepancy is evident. Also, the single value parameters from qualitative analysis can be verified (e.g., integral break flow rate at 100 seconds). The general difference between the D'Auria AA and the AA of the symmetrized signal is that the symmetrized signal AAs are generally larger (because the edge effect is eliminated from the experimental signal) and are more monotonic increasing functions than D'Auria AAs (if the measure is an integral, it should be a monotonic increasing function in principle). On the other hand, eliminating the edge effect from the difference signal also decreases the value of AA. In this analysis, it very rarely happened that in the whole time interval the edge effect is significant (however, this is not the case for shorter time intervals). Therefore, when ranking participants by values of AA for each variable, the rank remains mostly unchanged for the whole transient duration time interval.

Table 3 Participants Performing Calculations

Organization	Calculation ID	Code Used
Commissariat à l'Energie Atomique (CEA), France	CEA	CATHARE 2.5
EDO "Gidropress" (GID), Russia	GID	TECH-M-97
Gesellschaft für Anlagen- und Reaktorsicherheit mbH (GRS), Germany	GRS	ATHLET1.2C
Institut de radioprotection et de sûreté nucléaire (IRSN), France	IRSN	CATHARE 2.5
Japan Nuclear Energy Safety (JNES), Japan	JNES	TRAC-P 5.5.2
Korea Atomic Energy Research Institute (KAERI), South Korea	KAERI	MARS 2.3
Központi Fizikai Kutató Intézet (KFKI), Hungary	KFKI	ATHLET 2.0A
Korean Institute of Nuclear Safety (KINS), South Korea	KINS	RELAP5/MOD3.3
Nuclear Research Institute (NRI), Czech Republic	NRI-K (Kyncl)	RELAP5/MOD3.3
Nuclear Research Institute (NRI), Czech Republic	NRI-M (Macek)	ATHLET 2.0A
Paul Scherrer Institute (PSI), Switzerland	PSI	TRACE 4.05
Türkiye Atom Enerjisi Kurumu (TAEK), Turkey	TAEK	RELAP5/MOD3.3
Universitat Politècnica de Catalunya (UPC), Spain	UPC	RELAP5/MOD3.3
University of Pisa (UPI), Italy	UPI	RELAP5/MOD3.2

Table 4 Variables Used in the BEMUSE Qualitative Analysis

ID	Description of variable
P1	Intact loop pressure in hot leg
P2	SG pressure—secondary side
P3	Accumulator A pressure
P4	Pressurizer pressure
P5	Core inlet fluid temperature
P6	Core outlet fluid temperature
P7	Upper head fluid temperature
P8	SG DC bottom fluid temperature
P9	Break flow rate in cold leg
P10	Break flow rate in hot leg
P11	ECCS integral break flow rate
P12	Primary side total mass
P13	SG pressure drop—UT PS
P14	Primary pump pressure drop
P15*	Rod surface temperature in hot rod in hot channel (zone 4)—bottom level
P16	Rod surface temperature in hot rod in hot channel (zone 4)—2/3 core height
P17*	Rod surface temperature in hot rod in hot channel (zone 4)—top level
P18	Rod surface temperature in average rod in average channel (zone 2)—bottom level
P19	Rod surface temperature in average rod in average channel (zone 2)—2/3 core height
P20	Rod surface temperature in average rod in average channel (zone 2)—top level

* Not used in FFTBM analysis

Table 5 Additional Derived Variables Available for Quantitative Assessment

ID	Description of variable
intP9*	Integrated break flow rate in cold leg
intP10*	Integrated break flow rate in hot leg
PN3+	Total integrated break flow

* Calculated by JSI from data flow rates and not used in FFTBM analysis
\+ Received from University of Pisa; not used in FFTBM analysis

Nevertheless, in comparisons of the accuracy of variables as the transient progresses, their rank changes with time. Because of the elimination of the edge effect from the signals, the mean of the total AA of calculations increases from 0.27 to 0.37. Figures 4 through 23 also show that variables with AA values close to 1 and above are very inaccurate from the very beginning of the transient (examples are P9, P10, P13, and P14). These are mostly break flows and pressure drops where the gradient of changes is very large. For example, in integrations of the break flow, the AA is 2 to 3 times lower; however, the weights are 3 times higher, resulting in a similar accuracy of the variable. It is obvious that these weights favor the mass lost through the break or injected into the system rather than the exact prediction of flows. However, because of weighting, the AAs of different variables cannot be directly compared; therefore, VAs were proposed. This approach is acceptable for one class of transients, although the FFTBM becomes a less general method if the definition of weights is required for each class of transients.

Figure 4 shows the hot leg pressure at the beginning of the accident. FFTBM indicates that, in several calculations, the discrepancy is already evident in the first seconds. A detailed investigation revealed that the experimental pressure drop occurred in 0.1 seconds, while several calculations (those of CEA, KINS, IRSN, NRI-K, NRI-M, PSI, TAEK, and UPI) provided data with a time step of 0.5 seconds. This discrepancy has the most impact on accuracy. After the first time interval of 0–5 seconds, the accuracy of some calculations (those of GID, JNES, KINS, KAERI, and TAEK), further decreases. Qualitative analysis also identified these calculations. This is a good example of the ability of time-dependent accuracy analysis to give information useful in understanding the discrepancies. For example, FFTBM suggests a detailed investigation in the beginning of the transient; therefore, hot leg pressure was plotted in the time interval 0–1 second (see Figure 3(a)). After that, it become evident that more calculated data would be needed to describe the fast pressure drop. Finally, Figure 3(b) fully supports the BEMUSE qualitative conclusion regarding the pressure underprediction and quantitative results.

Figure 5 shows that, in the case of the JNES calculation of SG pressure on the secondary side, the AA is reduced because of the larger edge effect in the difference signal than in the experimental signal. In other cases, the contribution of the elimination of the edge effect from the experimental signal is larger than the contribution from the difference signal. Note that the very large AA value of the GID calculation is the result of several oscillations present in the signal, which are not physical, and the variable was therefore judged as unqualified in the BEMUSE qualitative analysis.

Figure 6(a) shows the accumulator pressure. In general, the injection occurs earlier in the calculations than in the experiment as the setpoint pressure is reached earlier (see Figure 3(a)). Discrepancies also appear in the second part of the transient when in some calculations (GID, UPC, NRI-K) the accumulator was isolated. Figures 6(b) and 6(c) show that the trend for D'Auria AA is not monotonic because of the large edge effect contribution during the pressure decrease. On the other hand, the AA obtained by mirroring clearly shows that the major reason for discrepancies is the earlier start of the pressure drop. It is also evident that accuracy in the second part of the transient decreases (the AA is larger) only for the calculations with increasing discrepancies. Finally, it can be seen that the elimination of the edge effect from the experimental signal almost doubles the value of AA_m.

Figure 7(a) shows the pressurizer pressure dropping to the containment pressure. The predicted pressure drop is faster than in the experiment. The trend of D'Auria AA (Figure 7(b)) and AA_m (Figure 7(c)) obtained by signal mirroring is similar to the trend of accumulator pressure, while the pressurizer pressure prediction is slightly more accurate than the prediction of accumulator pressure.

The visual agreement between the calculated and the experimental core inlet coolant temperature (see Figure 8(a)) for most calculations is good. The exception is the KINS calculation, which is also predicted by FFTBM. Figure 8(b) shows the large contribution of the edge effect to the difference signal in the case of the KINS calculation and, in part, the JNES calculation between 10 and 30 seconds. This contribution is eliminated in the case of signal mirroring, as shown in Figure 8(c). The BEMUSE qualitative analysis judged the KINS calculation of core inlet temperature as unqualified. FFTBM very clearly confirms this conclusion. The reason for the rather poor prediction in the case of the JNES calculation is the mismatch in the initial core inlet temperature, which is 50 K higher than the temperature in the experiment (hardly visible from the graph) and almost equal to the core outlet temperature, the earlier temperature drop, and the two heatups between 40 and 50 seconds. The detected wrong

initial temperature needs clarification. Finally, the elimination of the edge effect from the experimental signal increases the AA_m values by approximately 50 percent.

The visual observation of the core outlet temperature shown in Figure 9(a) reveals the largest discrepancies for the CEA, GRS, and NRI-M calculations. The quantitative results shown in Figures 9(b) and 9(c) confirm this observation. The BEMUSE qualitative analysis does not comment on these discrepancies.

No calculation predicted the behavior of the upper head fluid temperature shown in Figure 10(a). As shown, the calculations follow the trend of the core outlet fluid temperature. Because of this mismatch, the AAs shown in Figure 10(c) are larger than in the case of core inlet and outlet fluid temperatures. The BEMUSE qualitative analysis does not comment on this finding.

The differences in the SG fluid temperatures in the bottom downcomer are rather small (see Figure 11(a)); therefore the accuracy is also high. As the edge effect is small, the differences between the D'Auria AA and the AA obtained by mirroring are also small.

The experimental cold leg break flow shown in Figure 12(a) was largest in the initial 4 seconds, contributing almost half of the inventory lost. Therefore, the correct prediction during this period is the most important. One source of discrepancies is that, in the experiment, the break flow starts at 0.32 seconds, while in the calculations, it begins at 0 seconds. Second, in some calculations, the data are available only every 0.5 seconds, thereby slightly mitigating the effect of this delay (ramp function instead of step function). As shown in Figure 12(c), AA_m is then practically constant, and the value slightly decreases as the zero amplitude contributing to AA_m decreases as the transient progresses. Nevertheless, in the integration of break flows and making plots (see Figure 13(a)), FFTBM correctly ranks the calculations regarding cold leg break prediction.

The hot leg break flow (see Figure 14(a)) is smaller than the cold leg break flow. In the calculations, the exceptions were the UPC calculation (which shows just the opposite) and the JNES flow (in some periods negative). In spite of this, the GRS calculation was judged to be less accurate than the UPC and JNES calculations (Figures 14(b) and 14(c)) because of the initial flow spike, which contributed almost nothing to the mass lost through the break. An additional study of the mass balance in the PS revealed that the data for the GRS calculations of break flows are incorrect, as shown by Table 6.

The total integrated flow PN3 calculated by GRS is different from the sum of discharged masses calculated from the flow rate (P9, P10) also provided by GRS, while the mass balance for GRS is correct when using the GRS calculation of total break flow. At the end of the transient, the remaining PS mass is equal to PS initial mass ($P12_0$) plus the mass injected by the ECCS (P11) minus the mass discharged through the break (PN3). The mass balance check (without mass error) shows that the JNES flow rate data are also wrong. In the UPC calculations, the PS mass is not consistent with the calculated injected and discharged flow. Also, the break flows are quite different from the experimental data. It is also strange that more PS mass was discharged through the hot leg side of the break (the opposite of the situation in the experiment and most of the calculations). The CEA, GRS, and KFKI calculations obtained perfect mass balance, when considering the data received for the integral of total break flow. Besides the UPC calculation, the KAERI calculation also obtained rather poor mass balance, as judged by FFTBM. Finally, Figure 14(c) shows that FFTBM clearly distinguishes the GRS, JNES, and UPC flow rates (all suspicious data) from other calculations.

Table 6 Masses for Mass Balance Verification

	Mass (kg)									
	P11	$P12_0$	P12	intP9	intP10	cal1P12	cal1P12-P12	PN3	cal2P12	cal2P12-P12
EXP	2019	5330	1862	3833	1602	1914	53	NA	NA	NA
CEA	2305	5639	1115	5177	1404	1364	248	6829	1116	0
GID	1677	5568	791	5119	1425	702	-89	6558	687	-104
GRS	1849	6019	1437	6480	1819	-431	-1868	6431	1437	0
IRSN	2303	5865	1237	5136	1458	1573	336	6595	1573	336
JNES	1840	5515	1127	2062	-105	5397	4270	6428	926	-201
KAERI	2479	5645	1556	4843	892	2388	832	5823	2301	745
KFKI	1859	5566	1147	4631	1562	1233	86	6278	1147	0
KINS	2430	5283	842	5292	1702	720	-122	6429	1285	443
NRI-K	1953	5675	1742	3836	1341	2451	709	5375	2253	512
NRI-M	1960	5565	1709	4625	1500	1401	-308	5907	1618	-91
PSI	1989	5388	957	4885	1753	739	-218	6873	505	-453
TAEK	2602	5533	2497	3371	940	3824	1327	5349	2786	289
UPC	2168	5290	1571	1974	5900	-416	-1986	7874	-416	-1986
UPI	2169	5342	1666	4006	1662	1844	177	5634	1877	211

Note: $P12_0$ = initial PS mass, cal1P12 = (P11+$P12_0$-intP9-intP10), cal2P12 = (P11+$P12_0$-PN3)

The conclusions concerning accuracy, as judged with FFTBM for hot leg break flow, are different from the conclusions obtained for integrated hot leg break flows, shown in Figure 15. The reason is that the accuracy of break flows depends too much on the first few seconds (later the rank remains practically unchanged); therefore, the KAERI calculation was judged to be the most accurate. For the integrated break flow, the NRI-M calculation was the best. The NRI-M calculation was also the best for the ECCS integrated flow rate shown in Figure 16(a), as it resulted in the best prediction of the primary side total mass (see Figure 17(a)). For mass balance, the difference is also small (Table 6). Because of the definition of AA (normalization with experimental signal), the values of AA and AA_m are very large (Figures 16(b) and 16(c)). This results from the occurrence of the calculated accumulator injection earlier than in the experiment. After the accumulator empties, the mass trend (injected mass) becomes similar to that in the experiment, thus slightly increasing the accuracy of the ECCS injected mass. The accuracy (Figures 17(b) and 17(c)) of the primary side total mass shown in Figure 17(a) seems reasonable.

The pressure drop shown in Figure 18(a) is an oscillating variable. The AA is also oscillating (see Figures 18(b) and (c)), which is explained in more detail in Section 7.4. As the edge effect in the difference signal is overwhelmed by oscillations, the D'Auria AA and AA obtained by mirroring become rather similar. The AA values are close to or vary around value one because both AA_{err} and AA_{exp} depend on the oscillatory behavior of the experimental signal, and the calculated values are close to 0. Depending on all contributions to the AA, this value may be smaller or larger than 1. Because of an inherent feature of FFTBM, which is sensitive to oscillations, the results of AA are very limited for quantitative assessment. Nevertheless, such time functions of accuracy show the analyst that such results do not consider integrally the discrepancies and, therefore, the results are not appropriate for the calculation of total accuracy. Similar conclusions apply to the variable primary pump pressure drop shown in Figure 19. Without further treatment, such signals do not give a fair figure of merit. The weighting factors (see Table 1) have rather small values; therefore, this inconsistency is less pronounced in past

applications of the original FFTBM. Finally, the original FFTBM study in the framework of BEMUSE did not consider the variable primary pump pressure drop in the qualitative analysis but only in the quantitative analysis. The study reported that participants used an AA value close to or larger than 1.0 for the primary pump pressure drop. That conclusion is correct. However, without describing the reason (as given above), such a statement could be misleading as the value is close to or larger than 1.0 throughout the transient because of the highly oscillating experimental signal and the inability of the original FFTBM to make a fair quantitative assessment of such signals.

Figure 20(a) shows the rod surface temperature in the hot rod in the middle of the core. The largest mismatch occurs when core quench takes place earlier or later than in the experiment. The values of AA obtained by mirroring (Figure 20(c)) seem reasonable and are similar to D'Auria AA at the end of the transient (Figure 20(b)). However, in the uncertainty analysis, the time period before core quench is more important. The BEMUSE Phase III report (Ref. 11) cites the GRS, KAERI, KINS, and UPI calculations as good reference calculations of maximum cladding temperatures. Table 14 of the BEMUSE Phase II report (Ref. 10) seems to contradict the above statement, as the GRS prediction of hot rod temperature was judged to be the worst. The explanation for this is that the GRS calculation in the first 35 seconds was in good agreement with the experimental data, as Figure 20 shows for both trend and accuracy measures. This was probably the meaning intended in the Phase III BEMUSE report. Nevertheless, when considering just the result for the whole time interval, the reader may get the impression that the GRS calculation of rod surface temperature is the least accurate. To resolve such problems, use of the FFTBM with the capability to calculate accuracy as a function of time is advantageous.

In general, the calculated rod surface temperatures in the average rod at the bottom (Figure 21(a)), middle (Figure 22(a)), and top (Figure 23(c)) overpredict the core heatup. There are a few exceptions, such as the calculations of KAERI, IRSN, and UPC in Figure 21(c); IRSN and KAERI in Figure 22(c); and CEA, KAERI, IRSN, UPC, and UPI (no heatup) in Figure 23(c). The BEMUSE qualitative analysis was oriented to the difference in PCT and the time of PCT, which is complementary information not directly obtainable from quantitative analysis. In the quantitative analysis, the most important factor is the time of core quench, as discrepancies in these values contribute much to AA. For this reason, the KAERI, NRI-M, and UPI calculations of rod surface temperature in the hot rod in the middle of the core were judged to be the best, while the BEMUSE qualitative analysis stated that the NRI-M and KAERI calculations show the maximum difference with respect to experimental PCT. This example illustrates why the quantitative analysis should not be separated from the qualitative analysis.

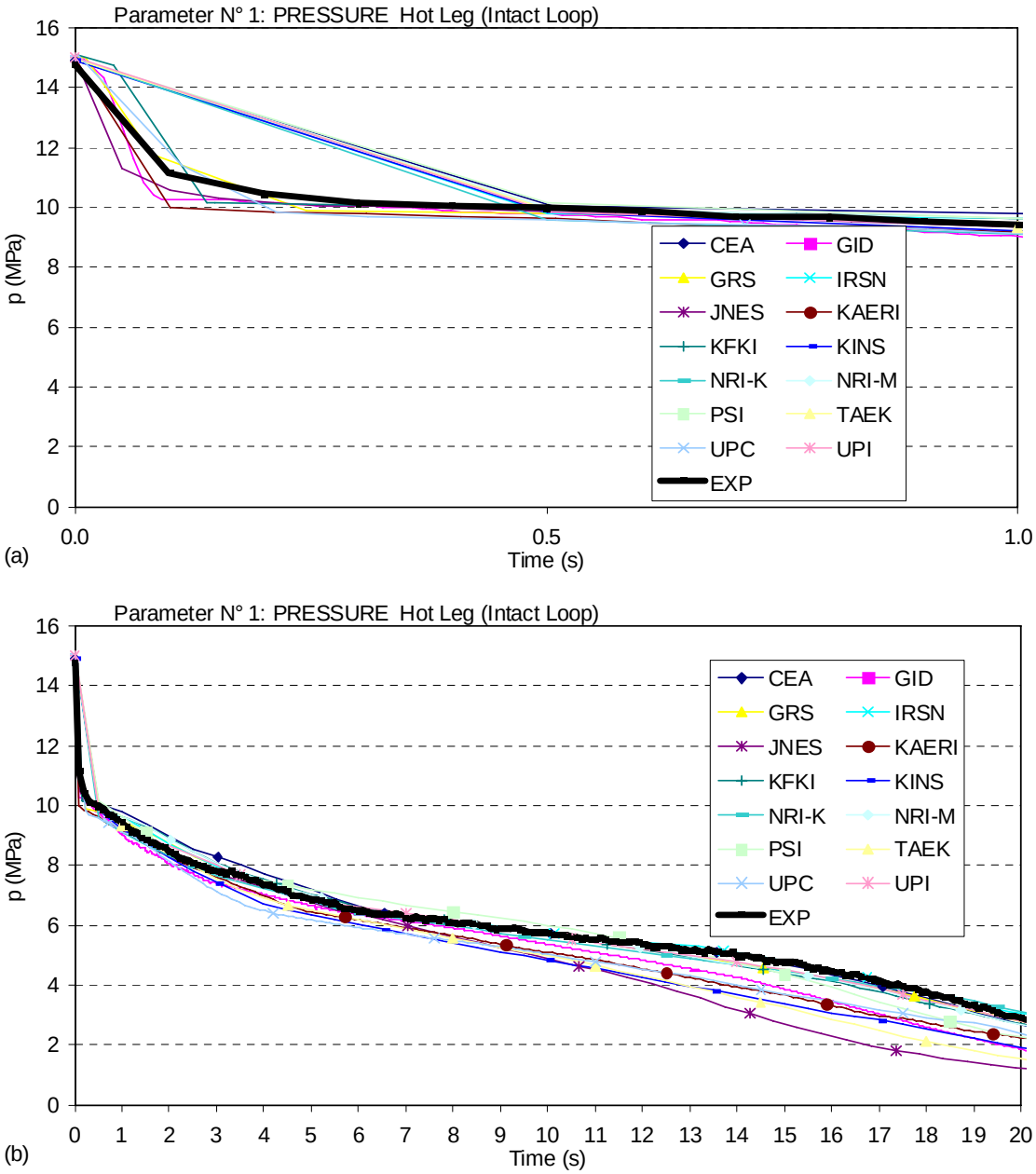

Figure 3 Intact loop pressure in hot leg (P1) in two different time intervals

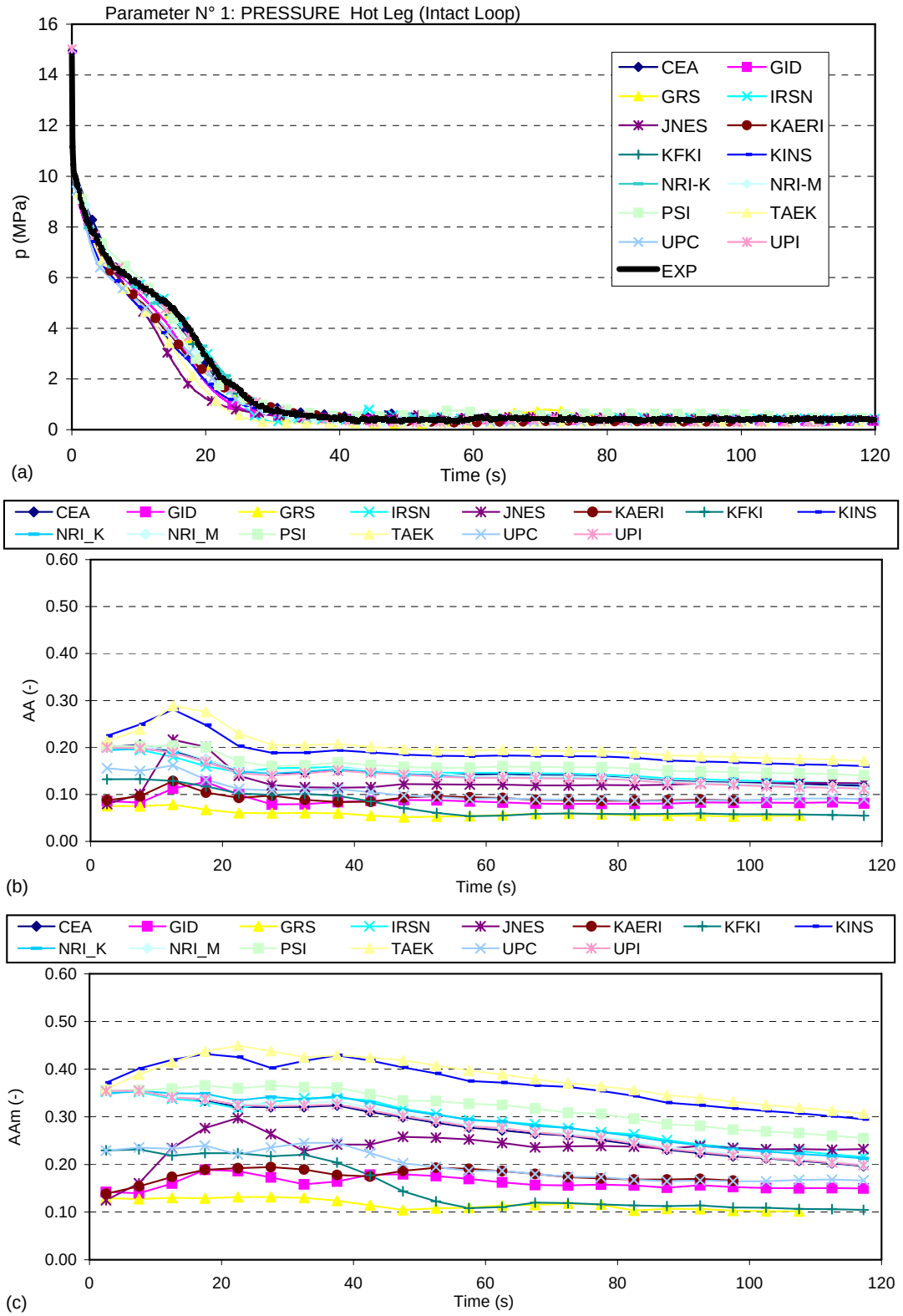

Figure 4 Intact loop pressure in hot leg (P1)—(a) time trends, (b) AA, (c) AA_m

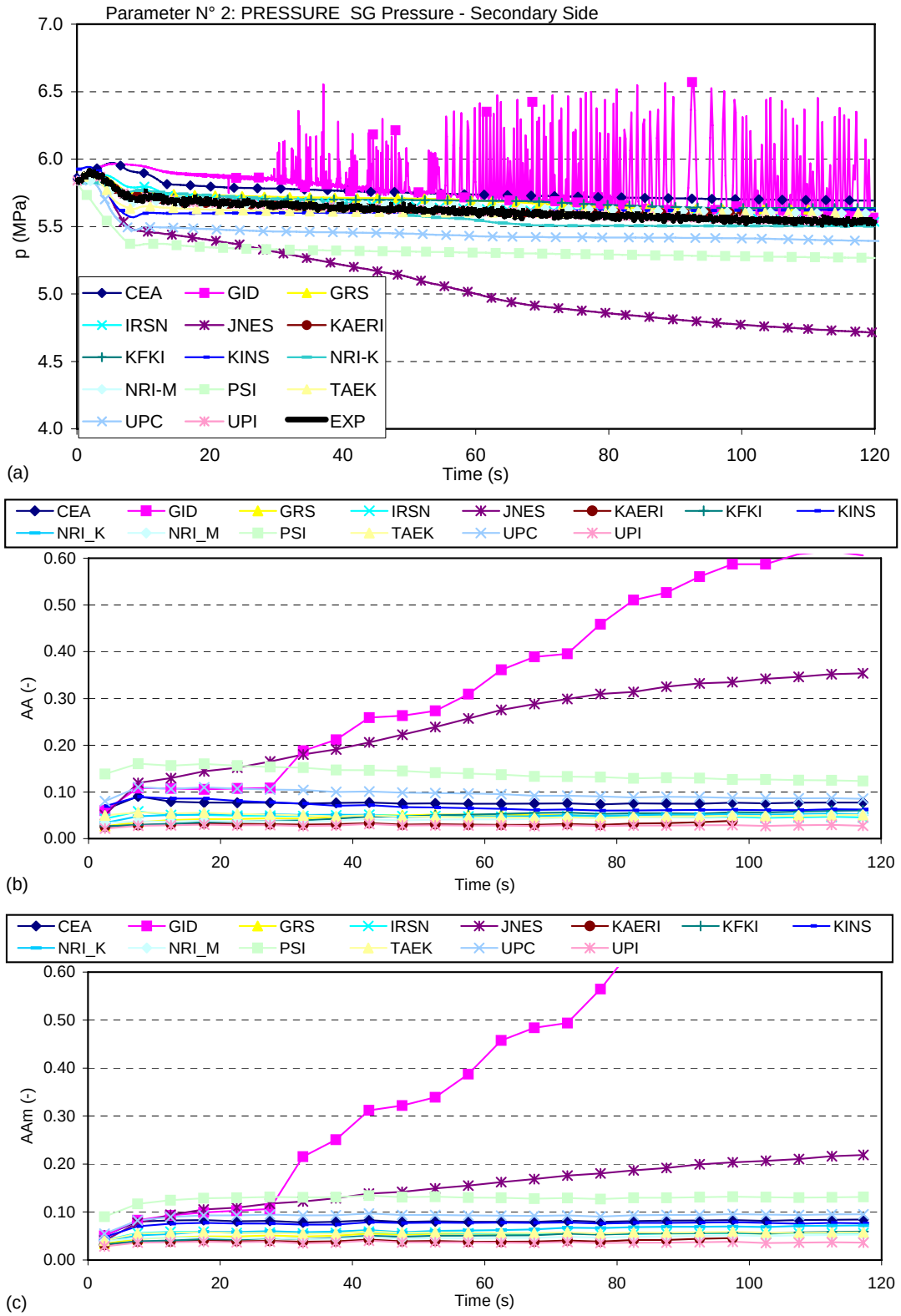

Figure 5 SG pressure, secondary side (P2)—(a) time trends, (b) AA, (c) AA_m

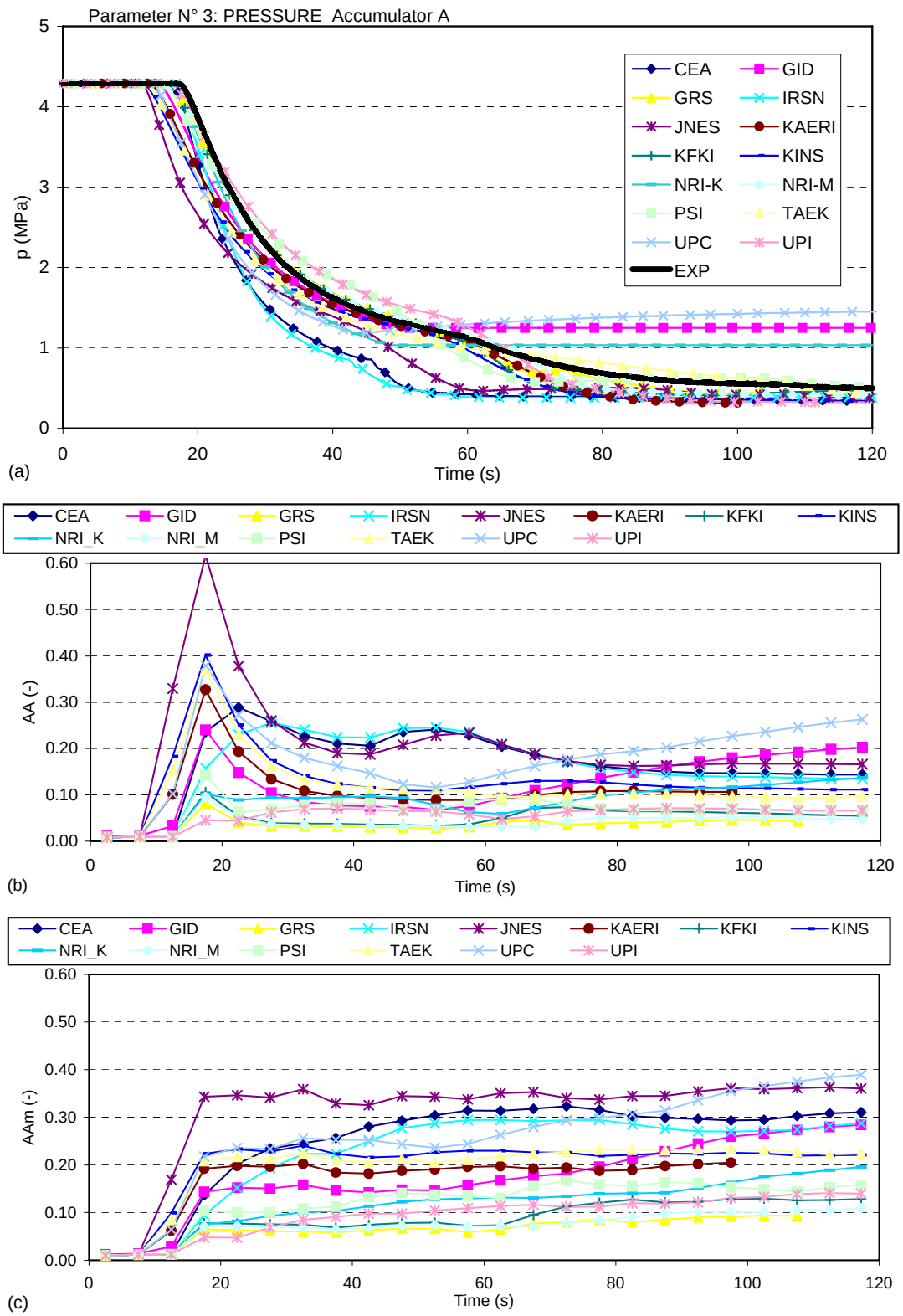

Figure 6 Accumulator A pressure (P3)—(a) time trends, (b) AA, (c) AA_m

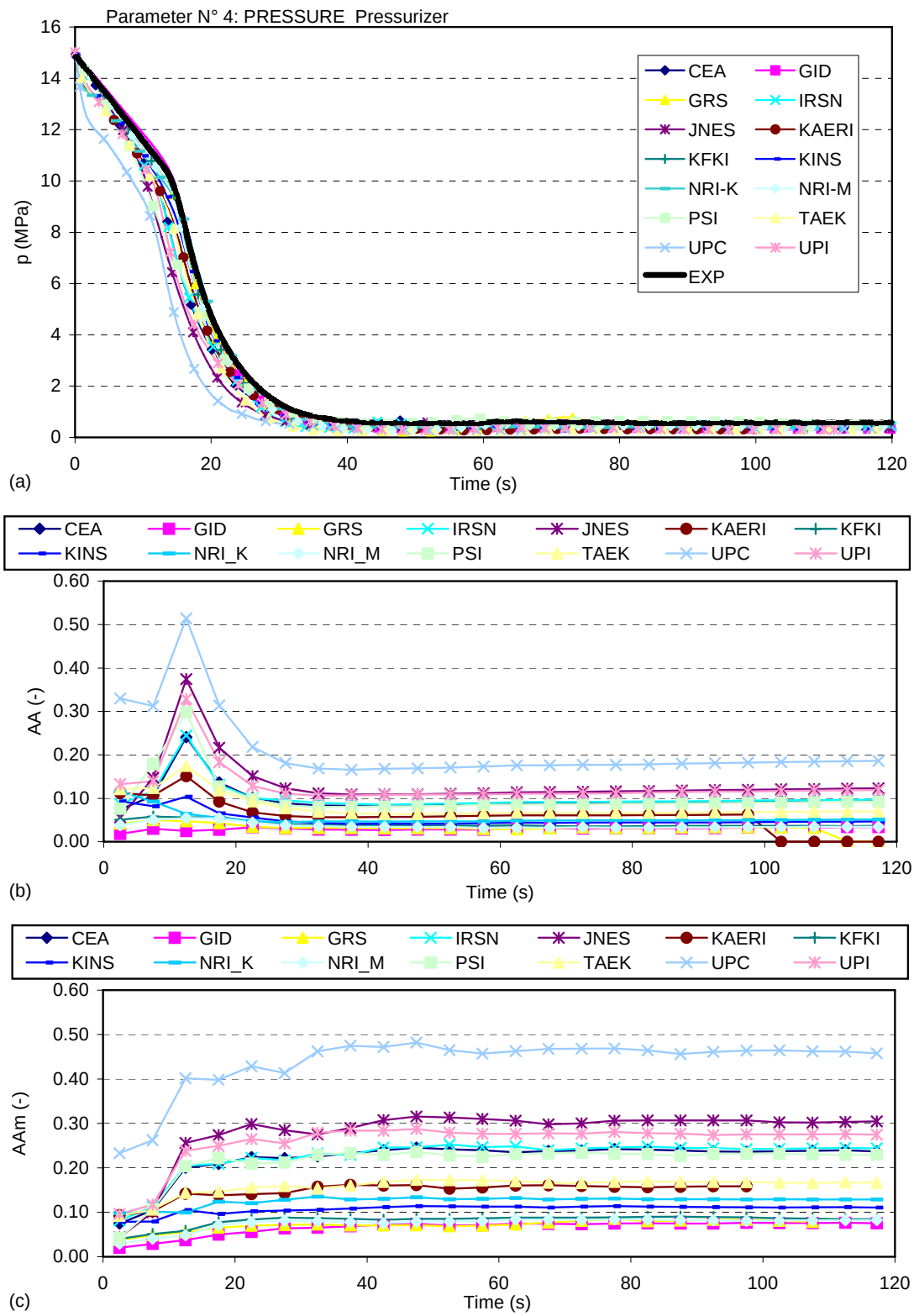

Figure 7 Pressurizer pressure (P4)—(a) time trends, (b) AA, (c) AA_m

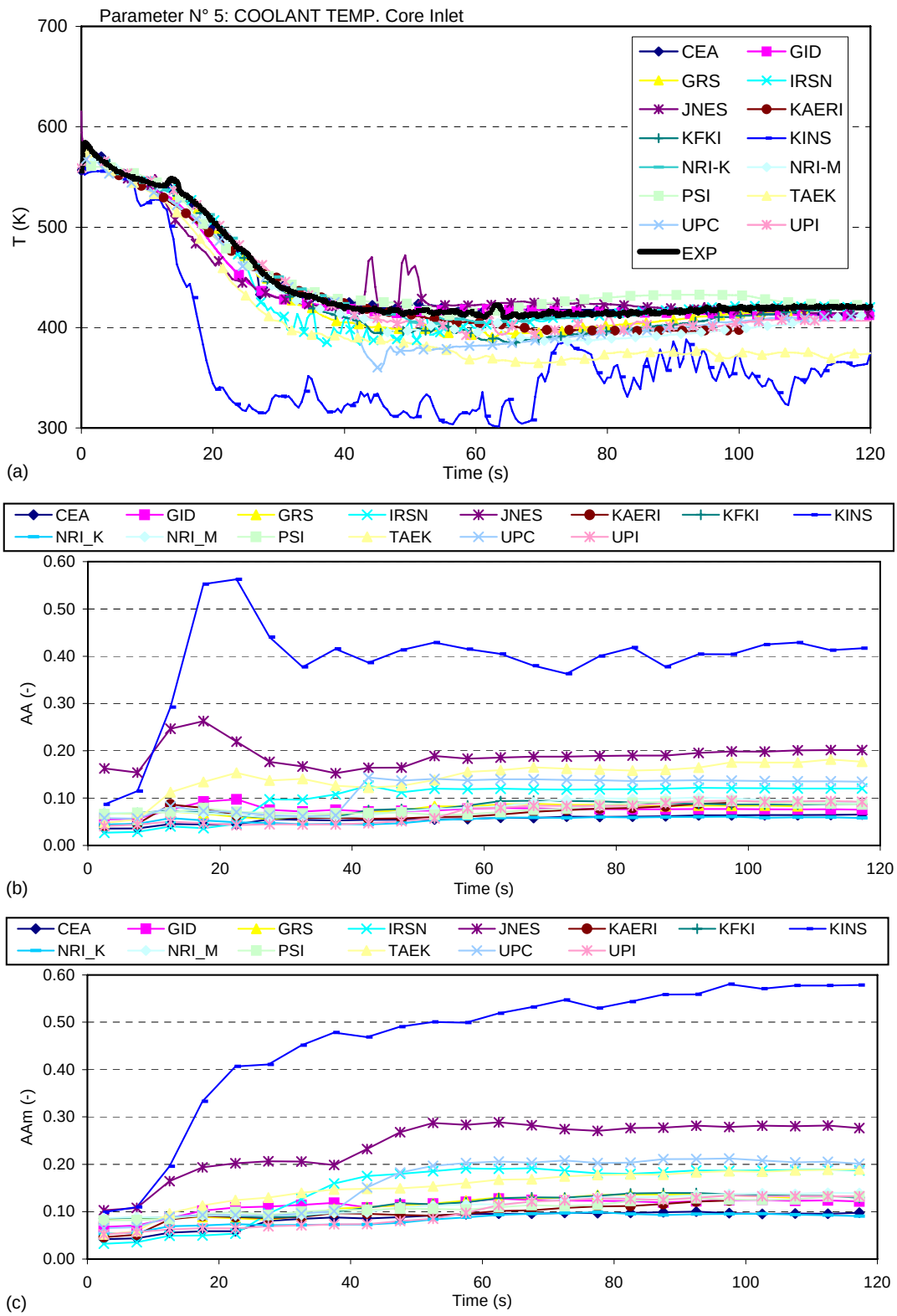

Figure 8 Core inlet fluid temperature (P5)—(a) time trends, (b) AA, (c) AA_m

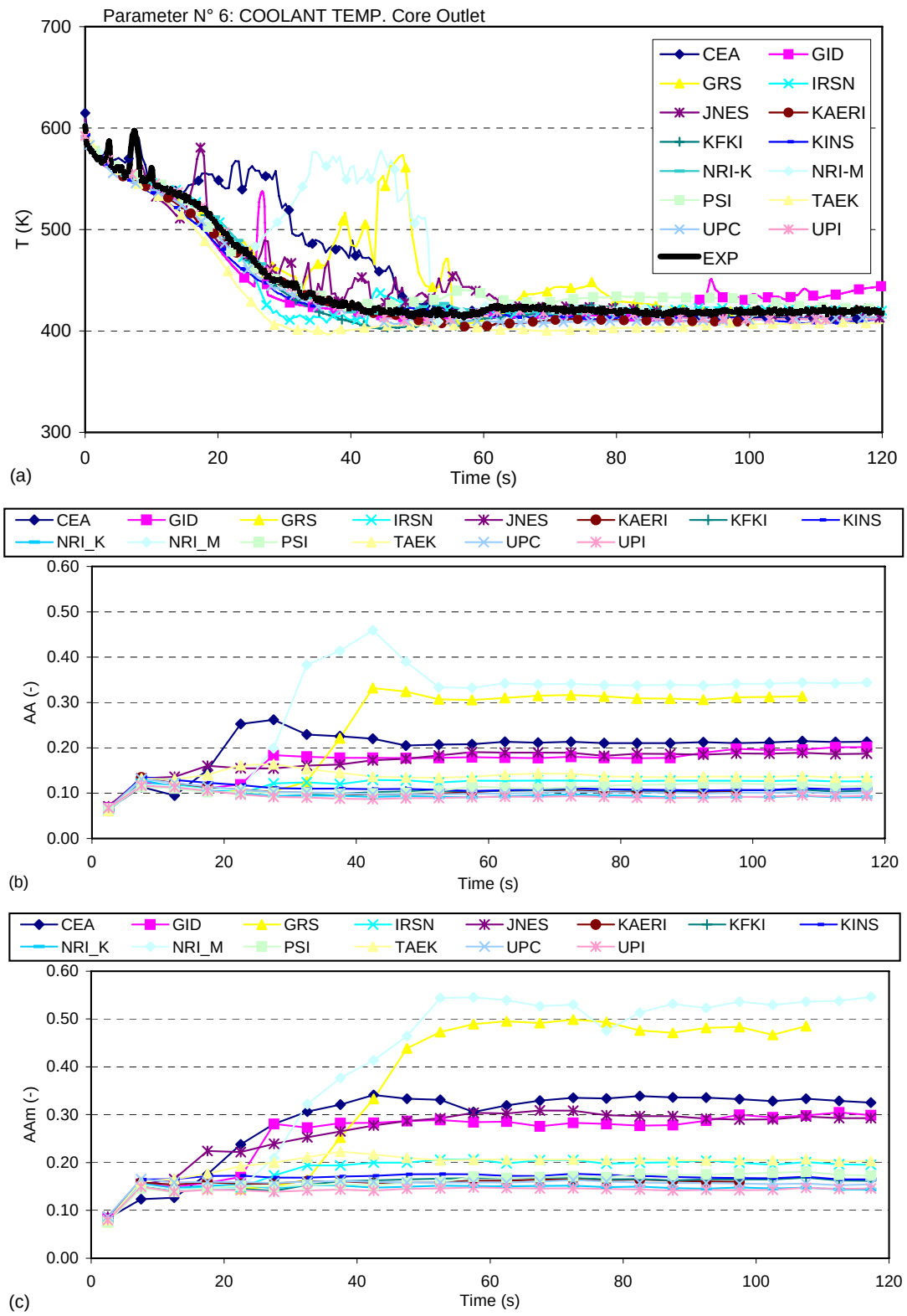

Figure 9 Core outlet fluid temperature (P6)—(a) time trends, (b) AA, (c) AA_m

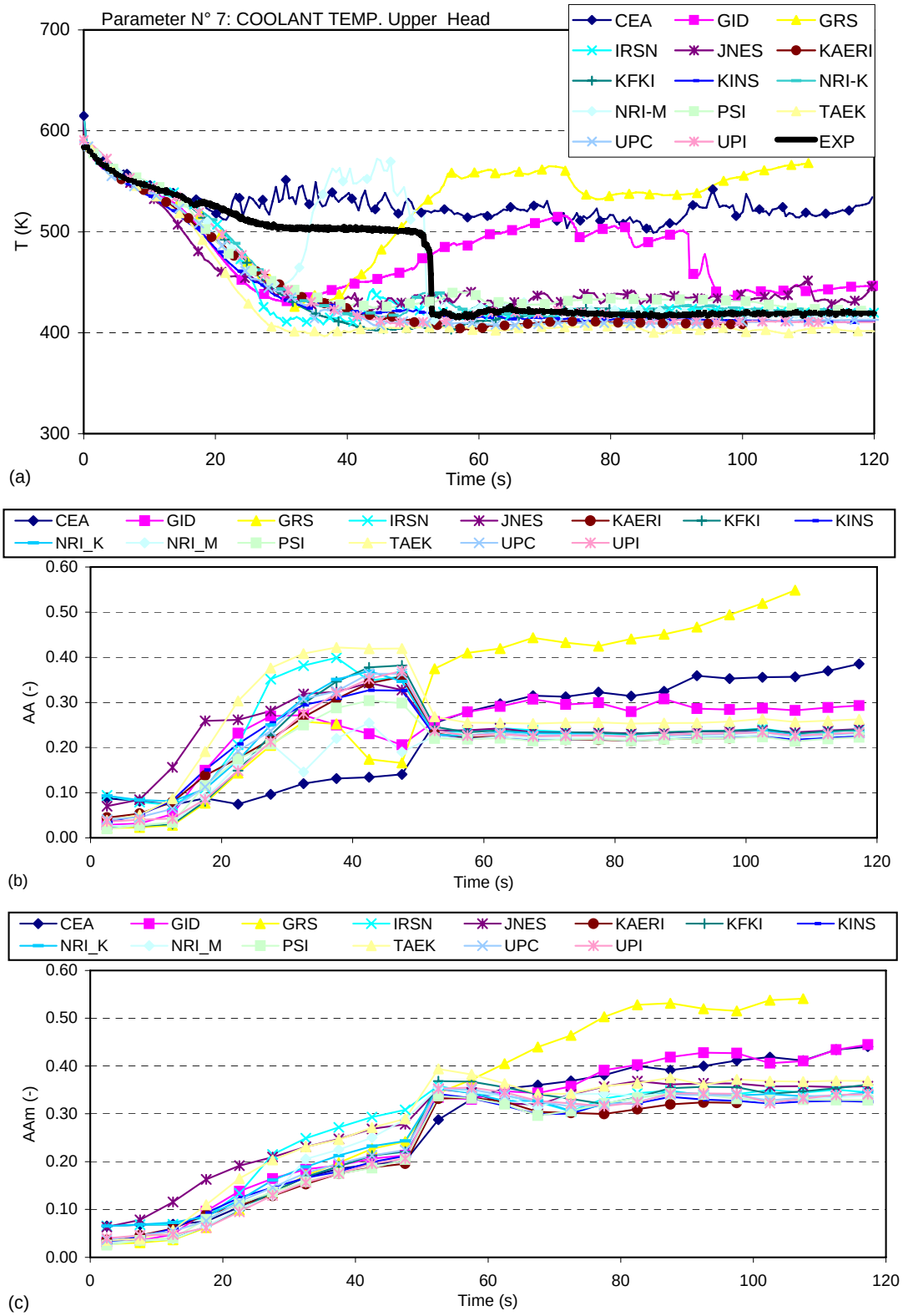

Figure 10 Upper head fluid temperature (P7)—(a) time trends, (b) AA, (c) AA_m

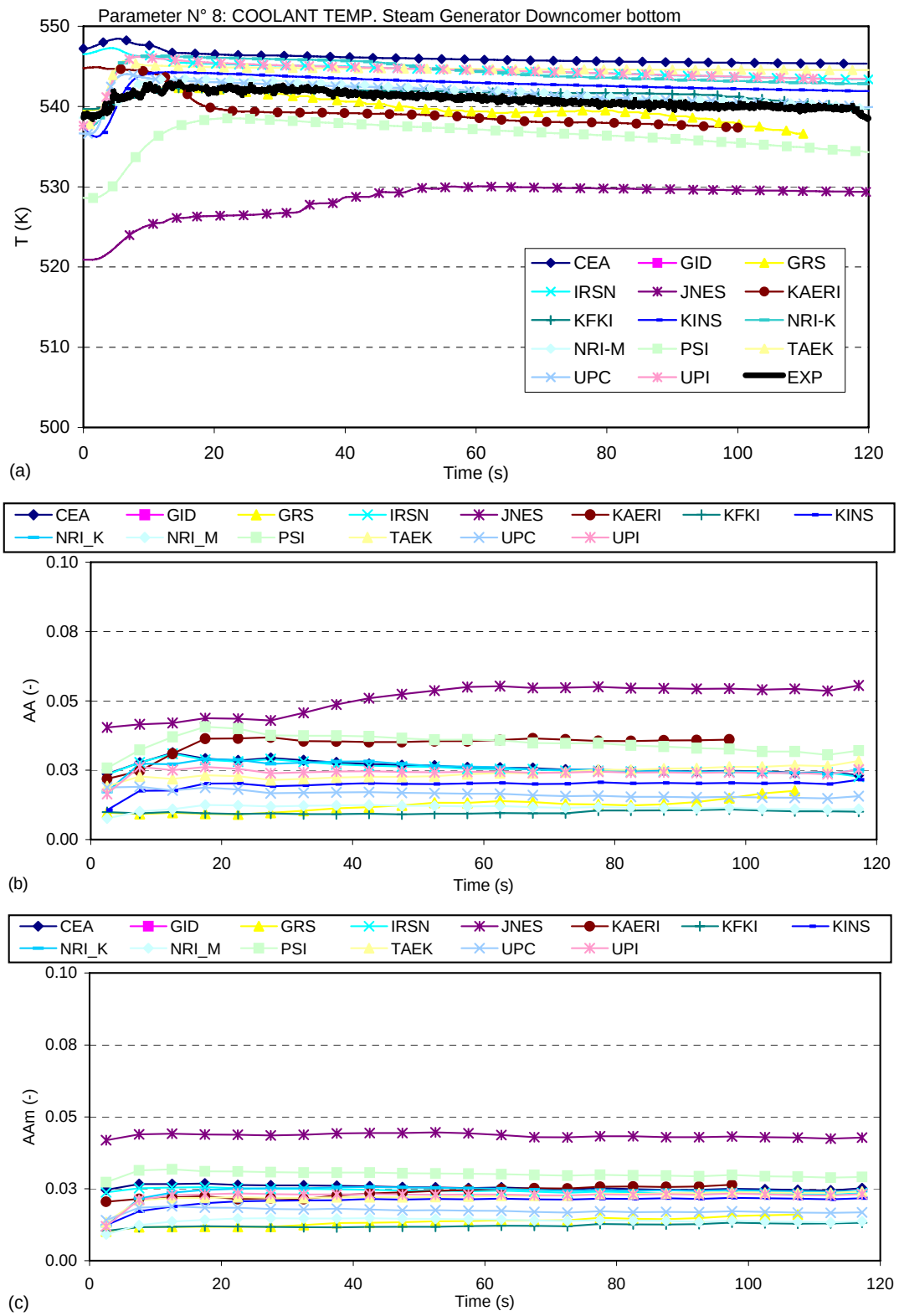

Figure 11 SG DC bottom fluid temperature (P8)—(a) time trends, (b) AA, (c) AA_m

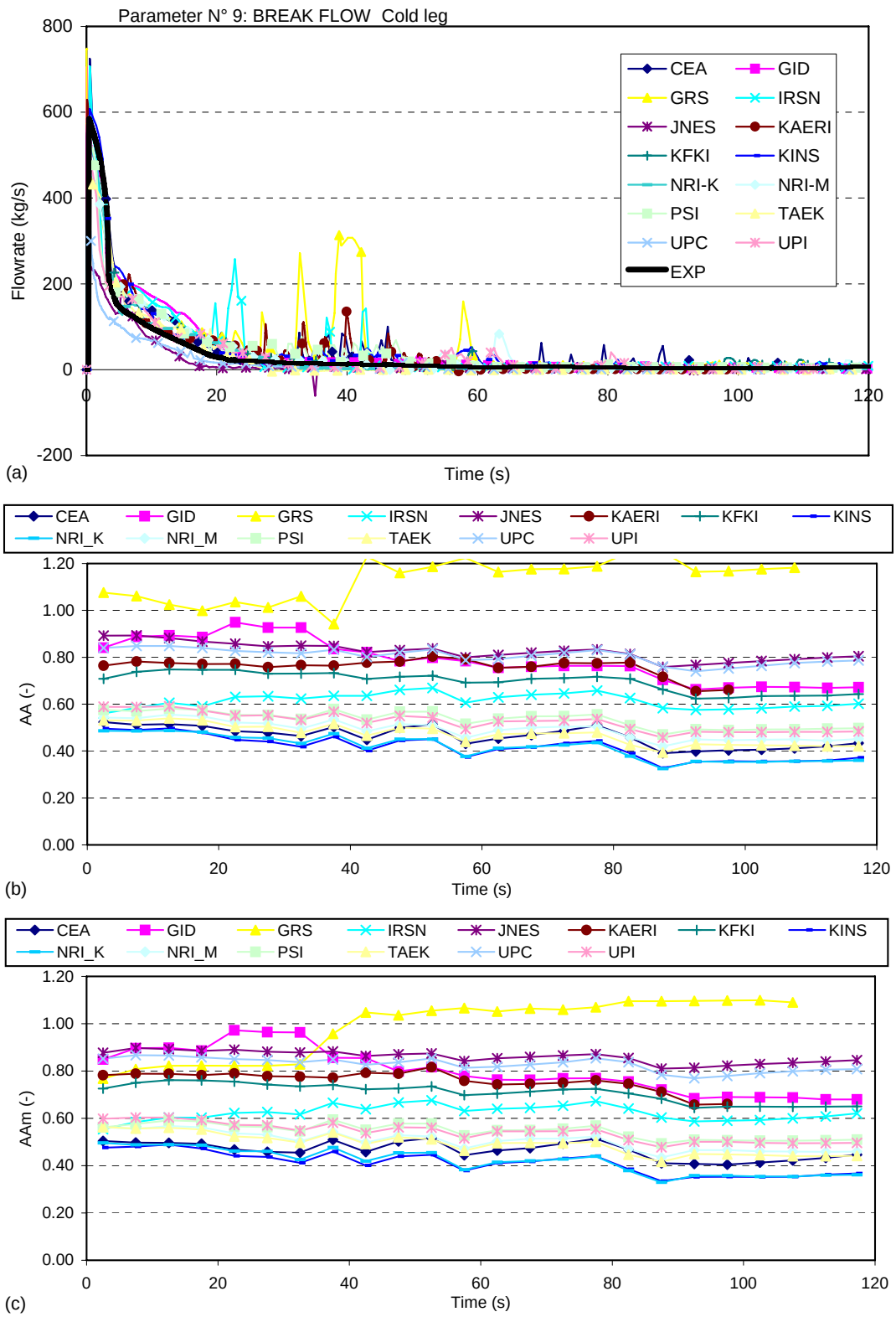

Figure 12 Break flow rate in cold leg (P9)—(a) time trends, (b) AA, (c) AA_m

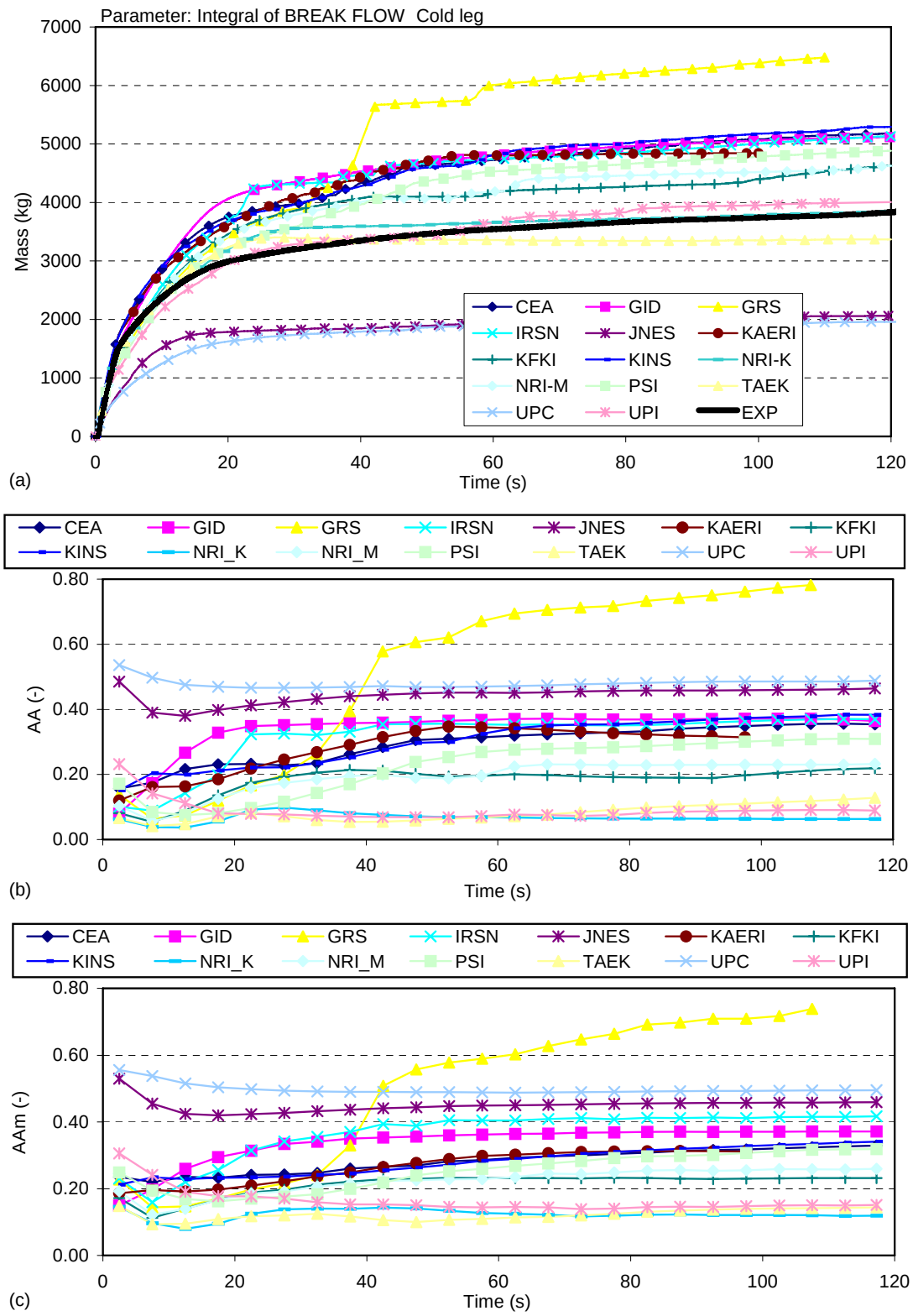

Figure 13 Integrated break flow rate in cold leg (P9int)—(a) time trends, (b) AA, (c) AA_m

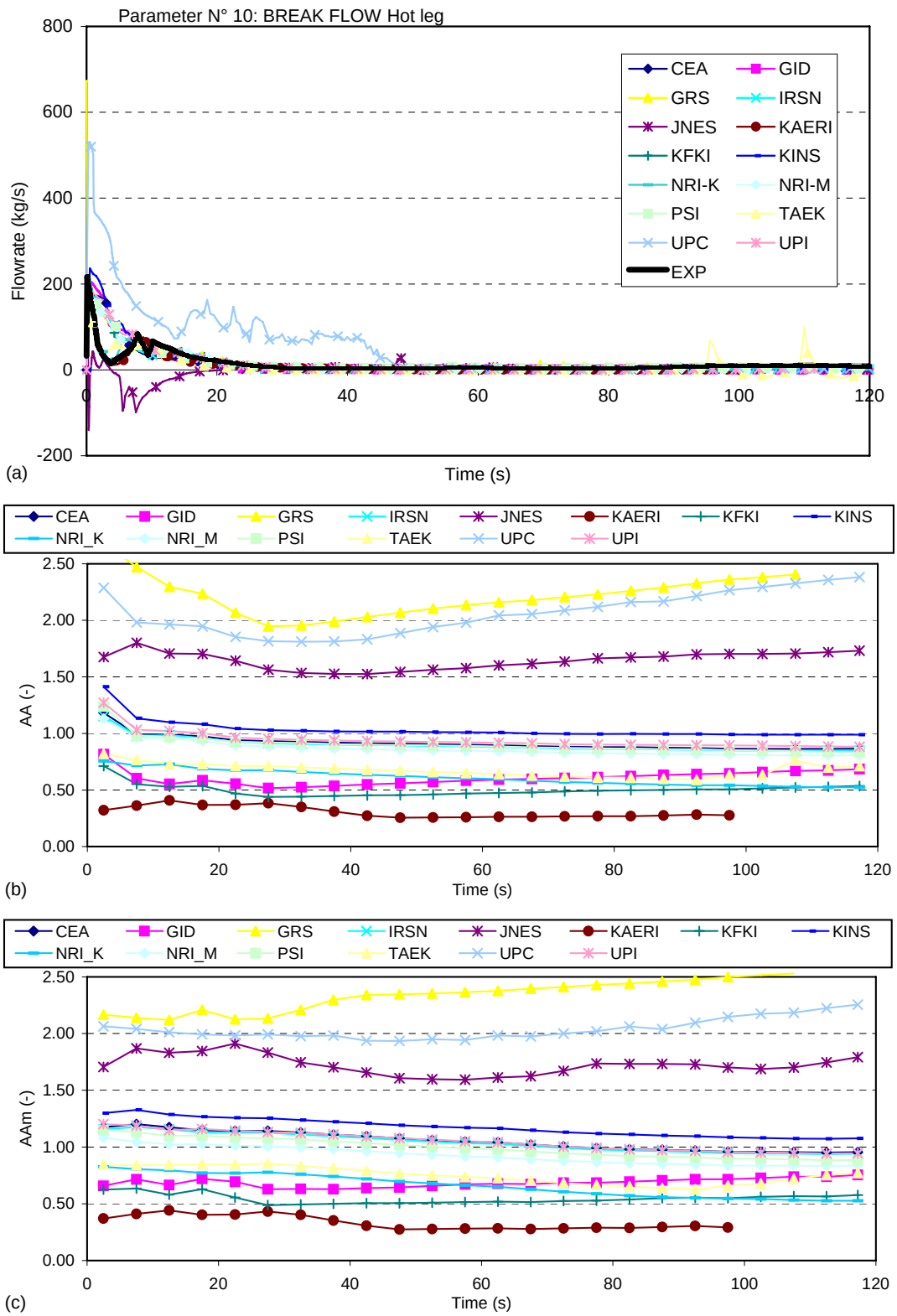

Figure 14 Break flow rate in hot leg (P10)—(a) time trends, (b) AA, (c) AA_m

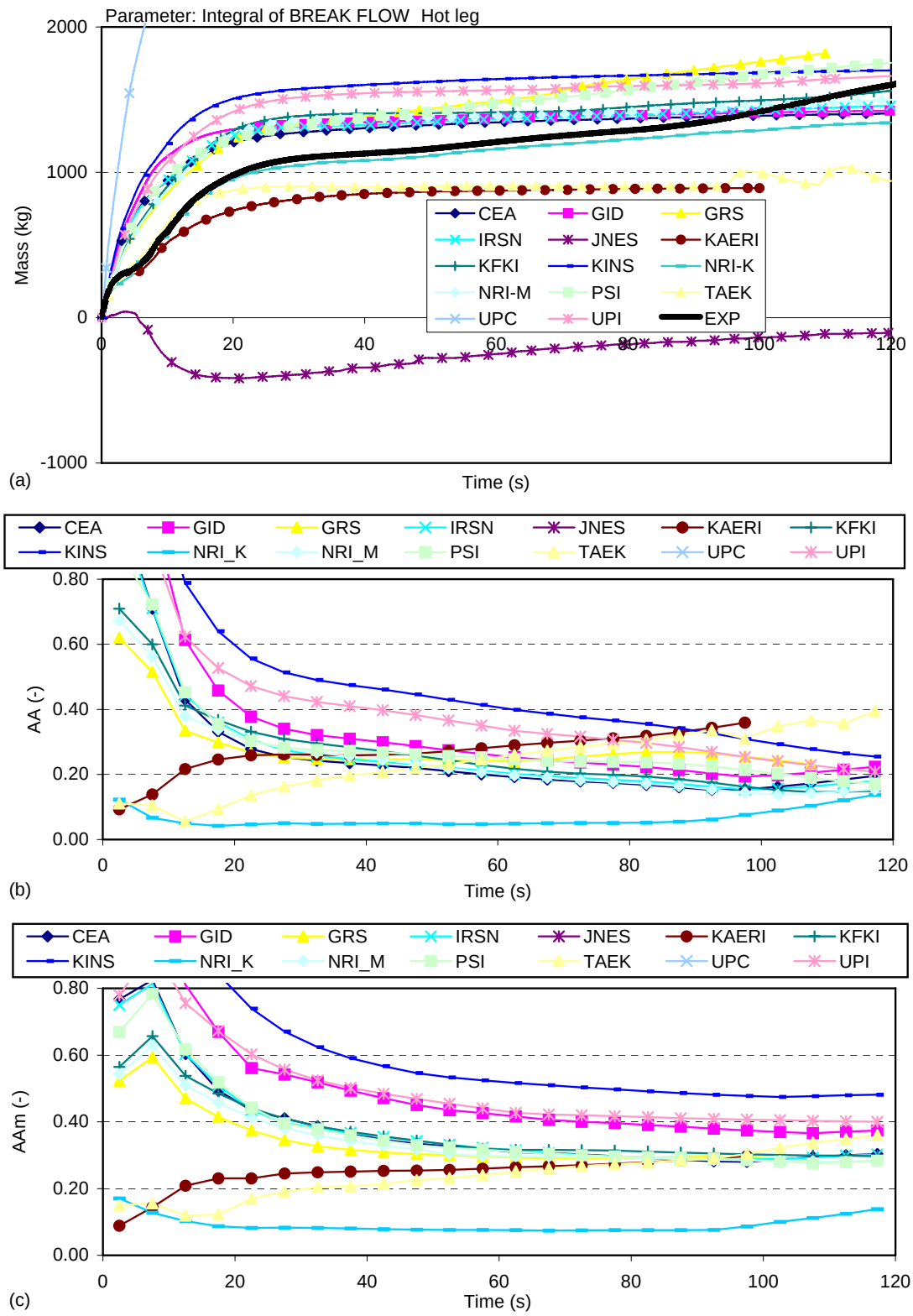

Figure 15 Integrated break flow rate in hot leg (P10int)—(a) time trends, (b) AA, (c) AA_m

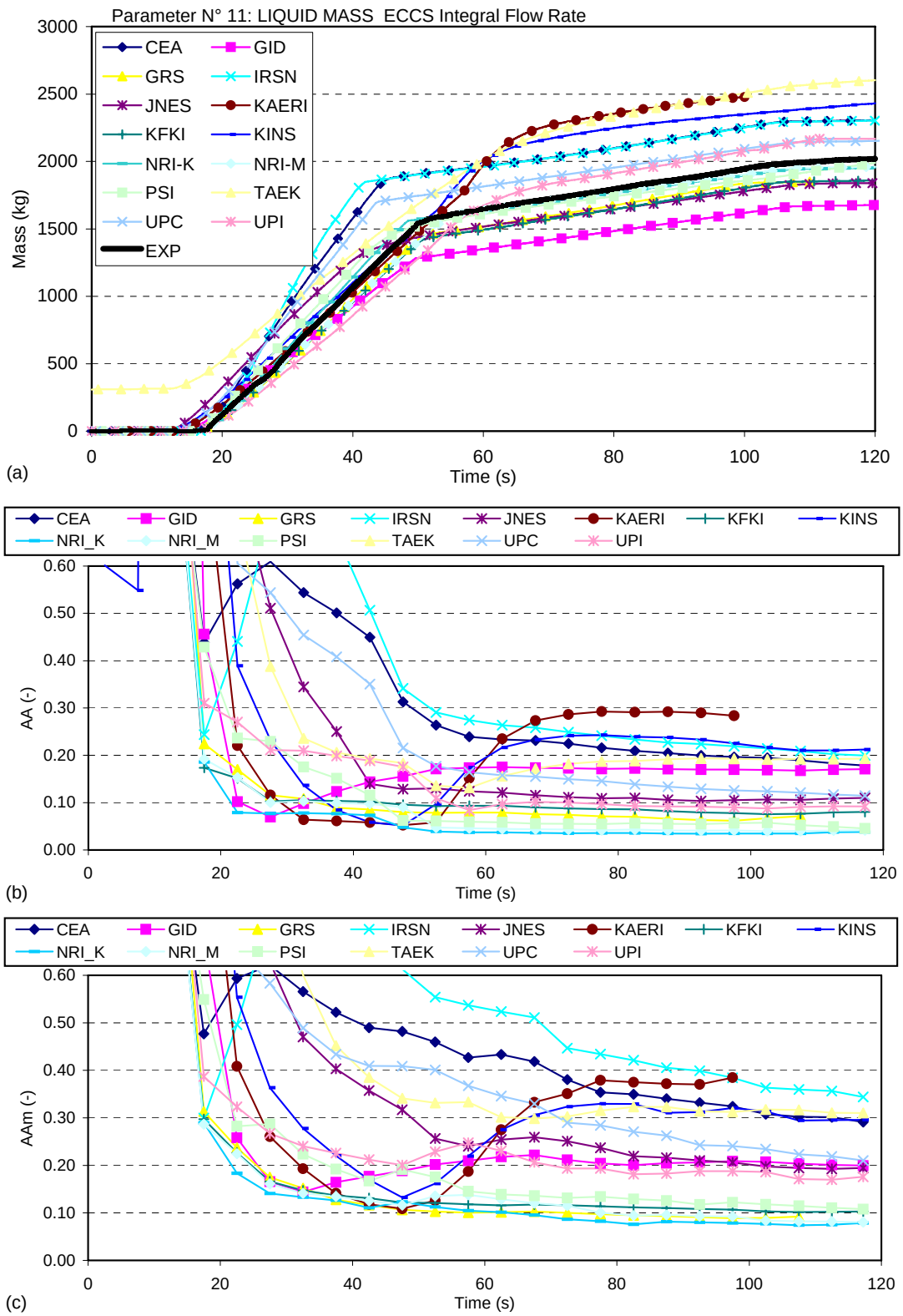

Figure 16 ECCS integral break flow rate (P11)—(a) time trends, (b) AA, (c) AA_m

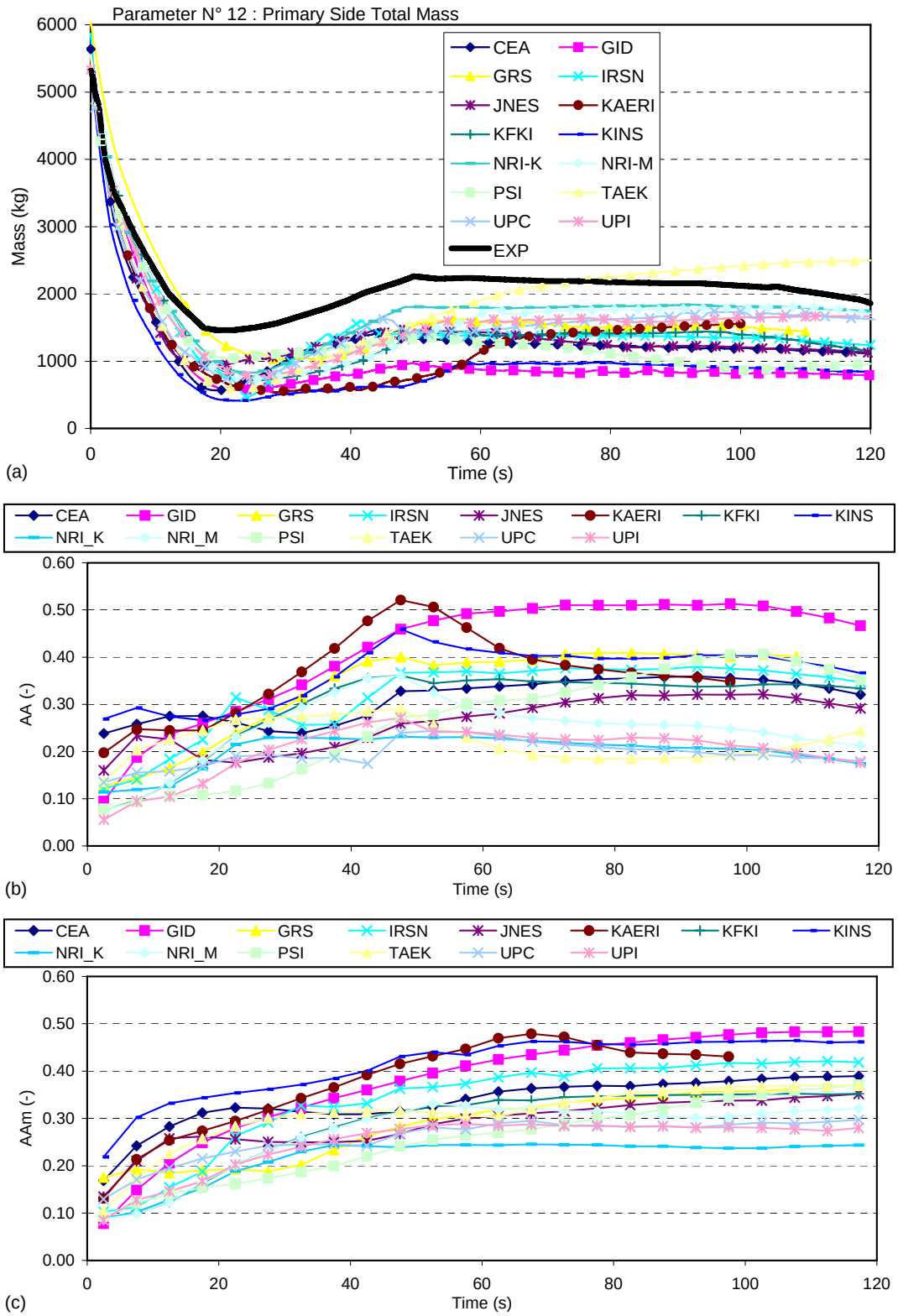

Figure 17 Primary side total mass (P12)—(a) time trends, (b) AA, (c) AA_m

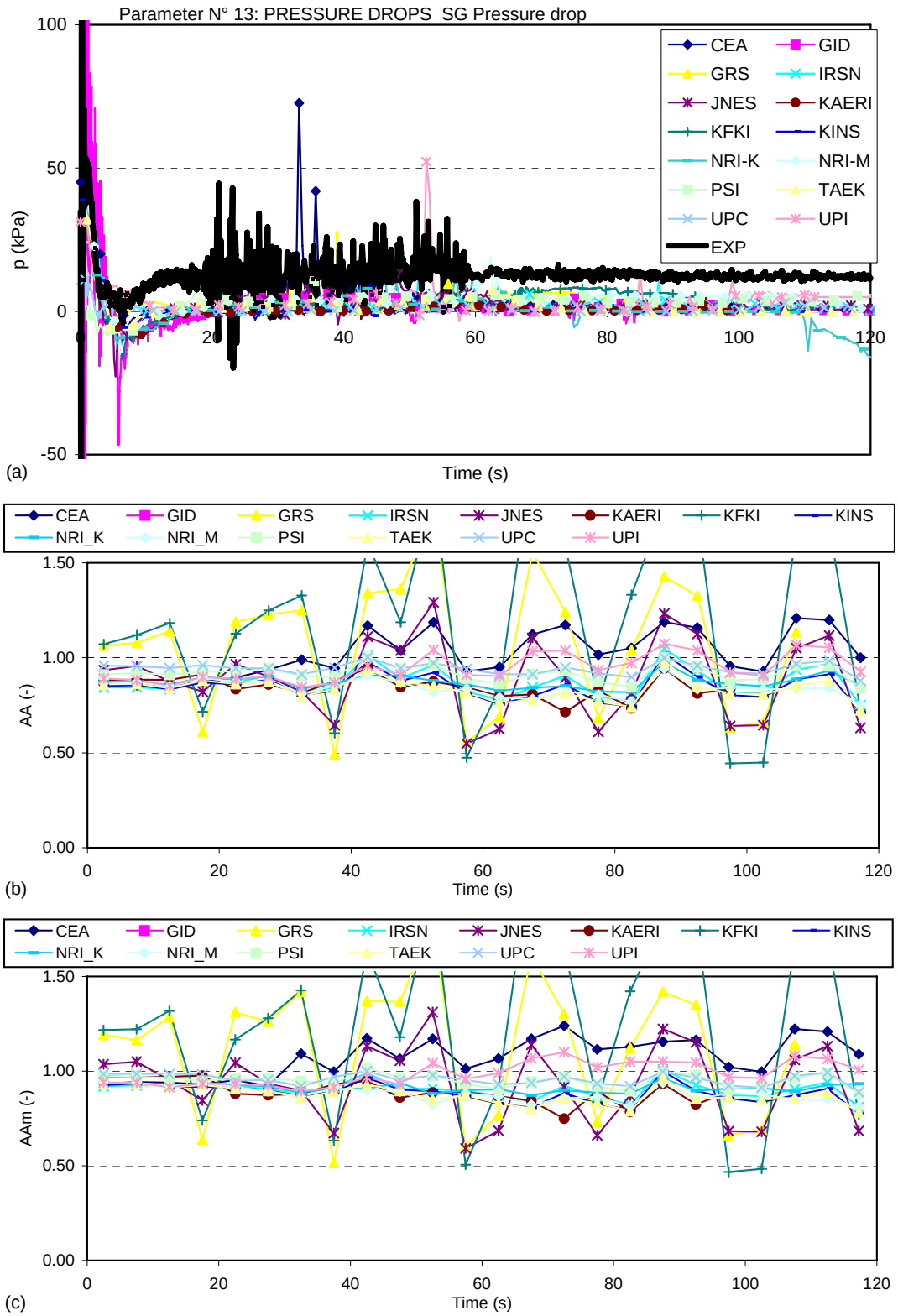

Figure 18 SG pressure drop—UT PS (P13)—(a) time trends, (b) AA, (c) AA_m

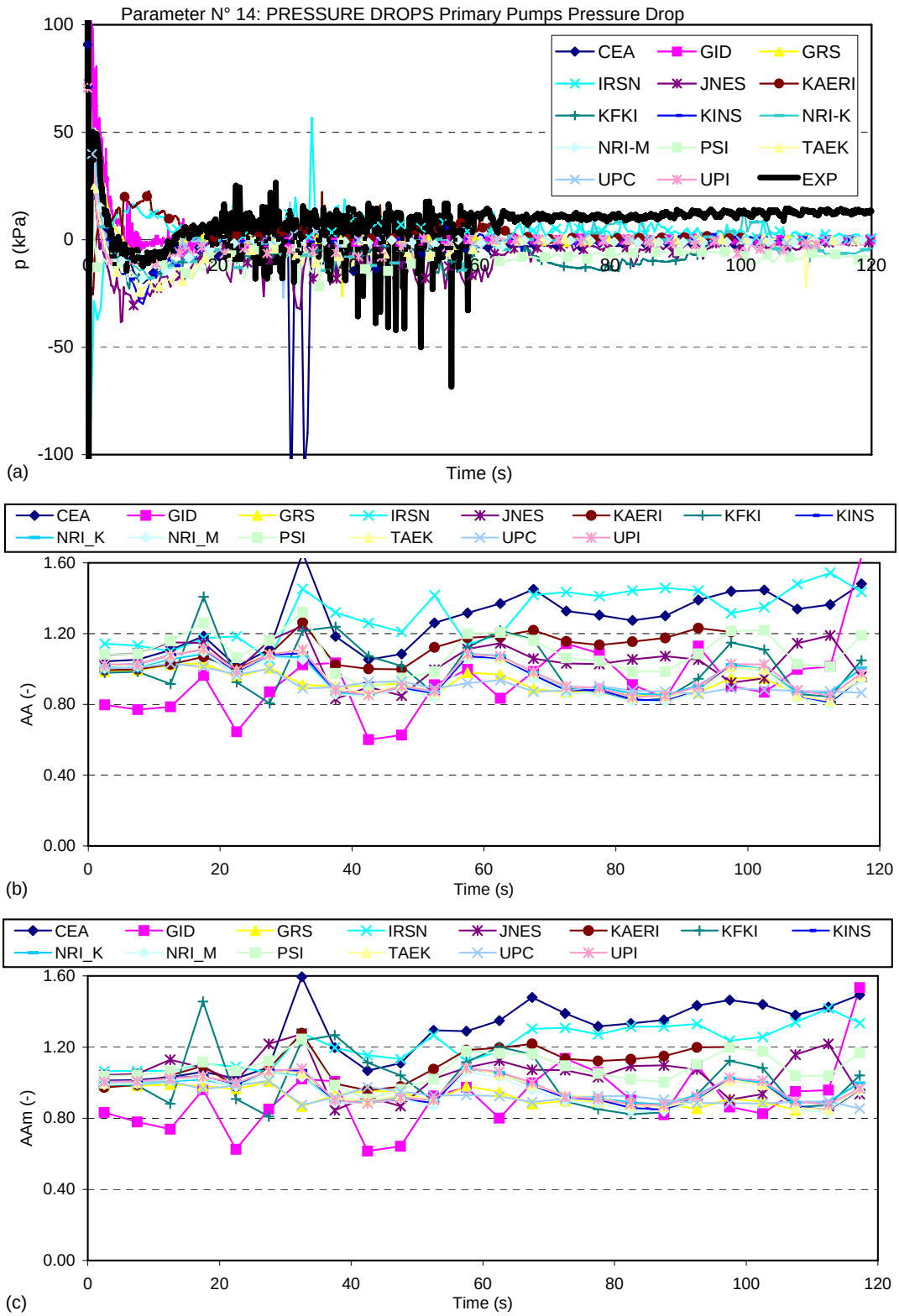

Figure 19 Primary pump pressure drop (P14)—(a) time trends, (b) AA, (c) AA_m

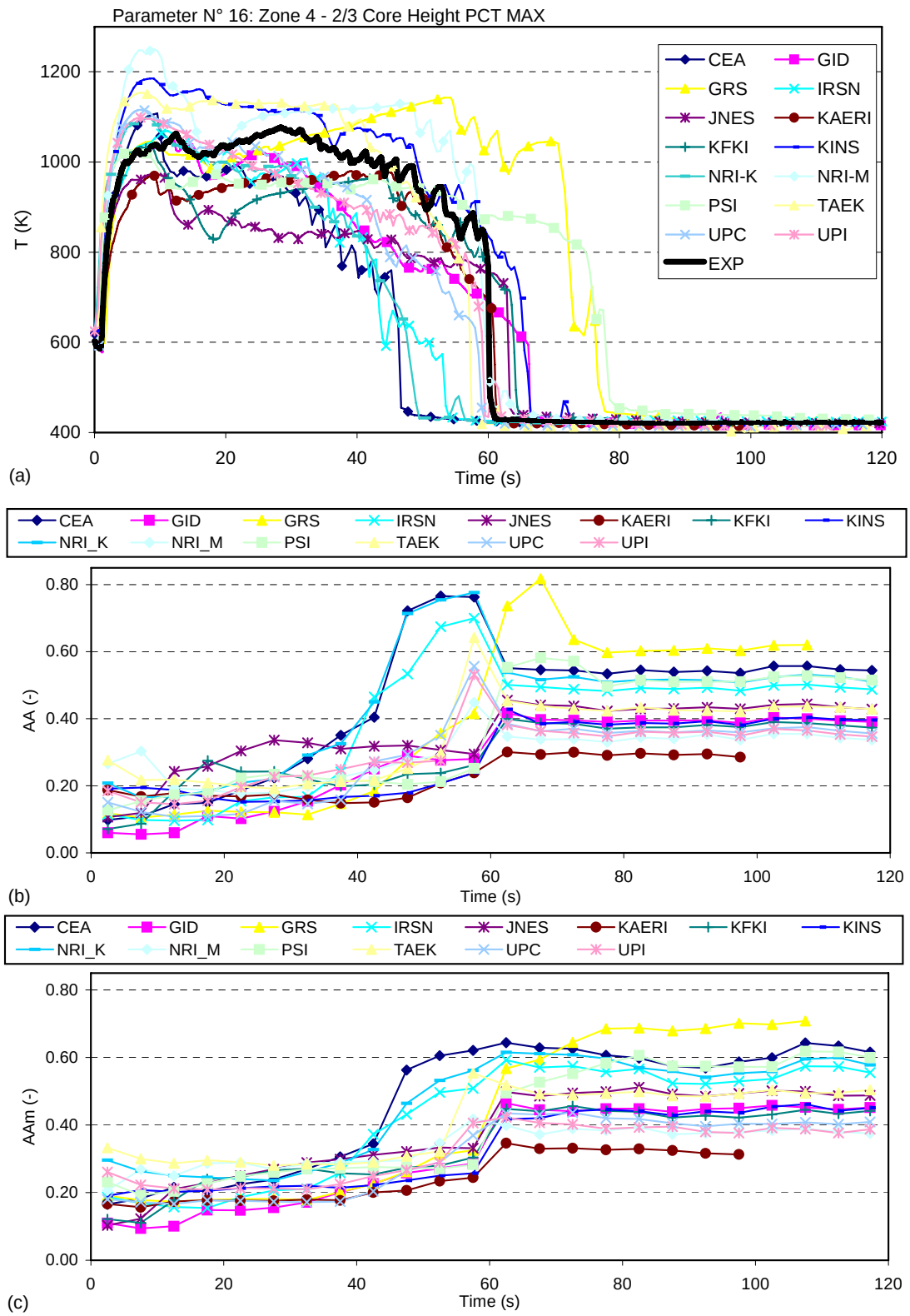

Figure 20 Rod surface temperature in hot rod in hot channel (zone 4) at 2/3 core height (P16)—(a) time trends, (b) AA, (c) AA_m

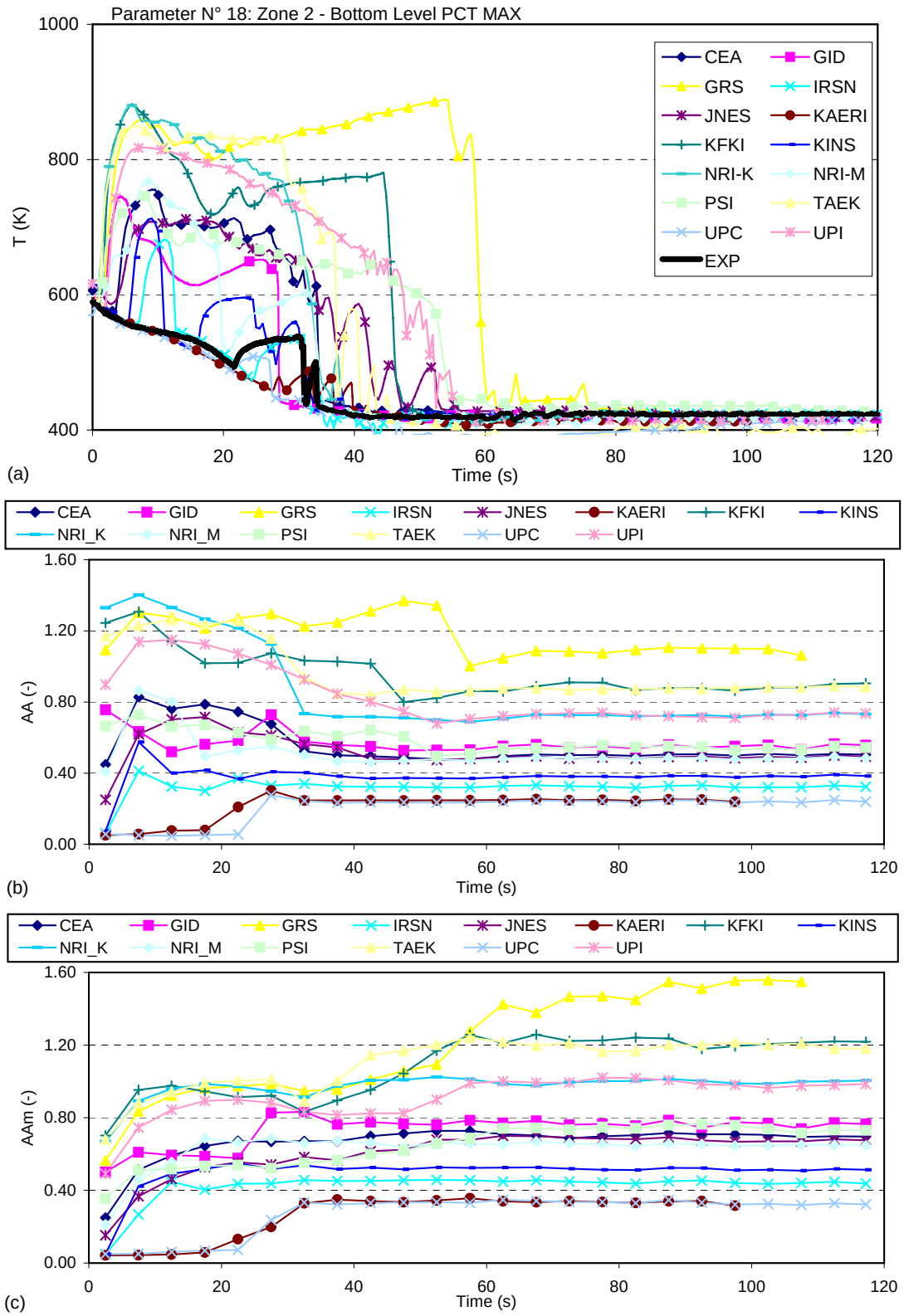

Figure 21 Rod surface temperature in average rod in average channel (zone 2) at bottom level (P18)—(a) time trends, (b) AA, (c) AA_m

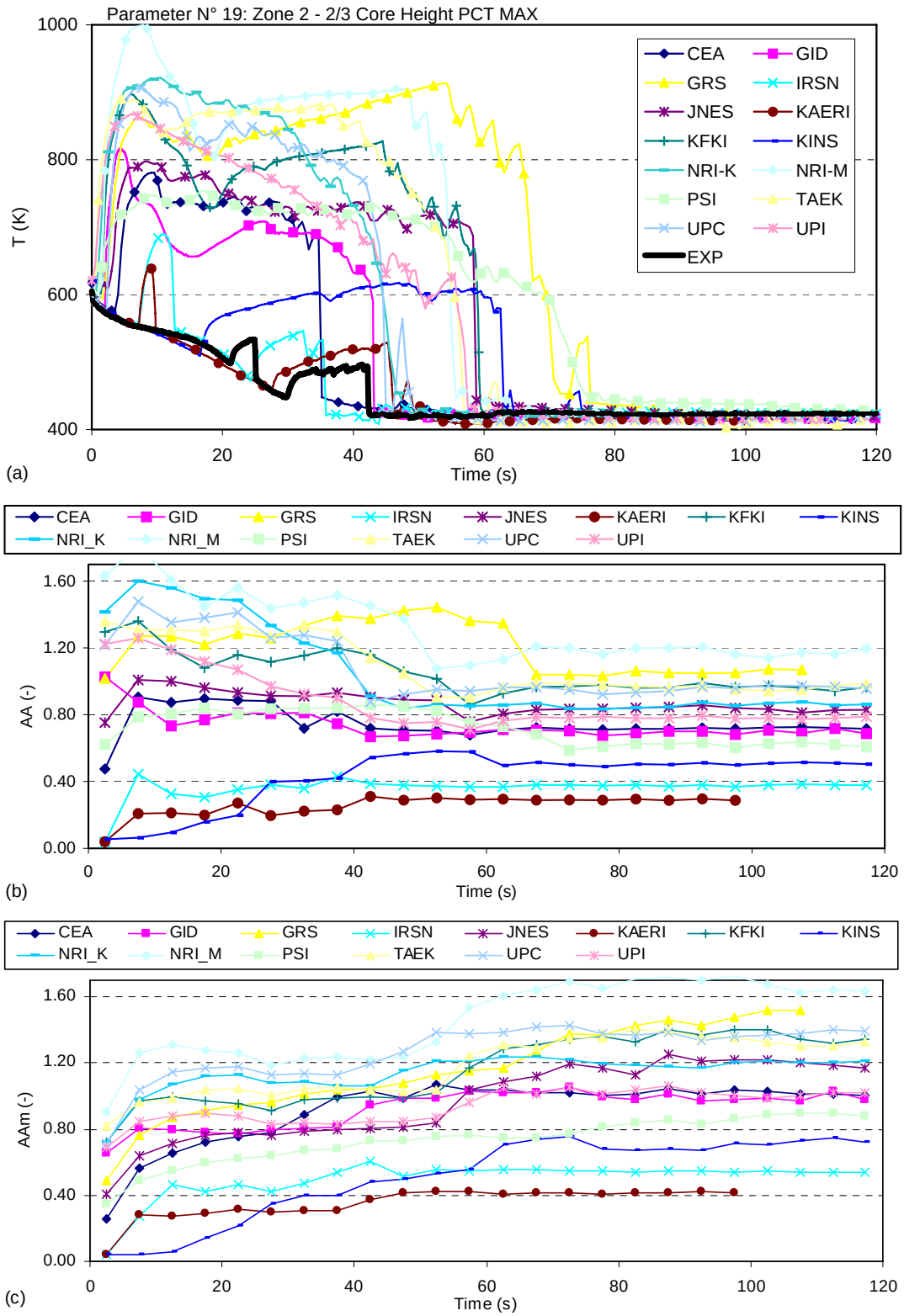

Figure 22 Rod surface temperature in average rod in average channel (zone 2) at 2/3 core height (P19)—(a) time trends, (b) AA, (c) AA_m

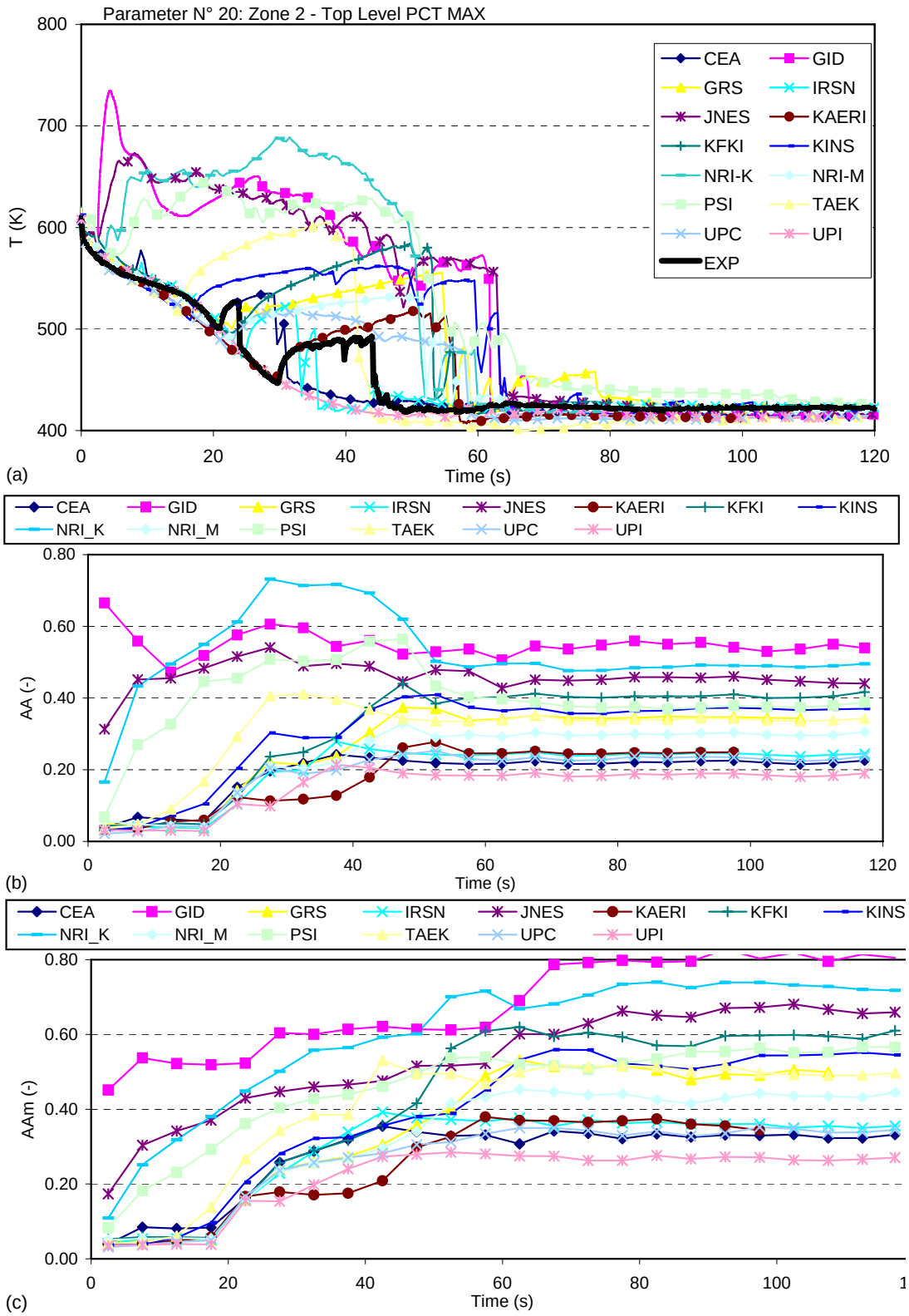

Figure 23 Rod surface temperature in average rod in average channel (zone 2) at top level (P20)—(a) time trends, (b) AA, (c) AA_m

Figures 24 and 25, respectively, show the total accuracy time trends obtained by the original FFTBM and the FFTBM improved by signal mirroring. As shown, GID total accuracy is significantly oscillating. The reason for this oscillation is that variable P13 with very high values of AA contributes much to AA_{tot}. Quantitative assessment does not find such high values acceptable. However, as already mentioned, variable P13 requires treatment with the moving average to give consistent results. Section 7.4 discusses this in more detail.

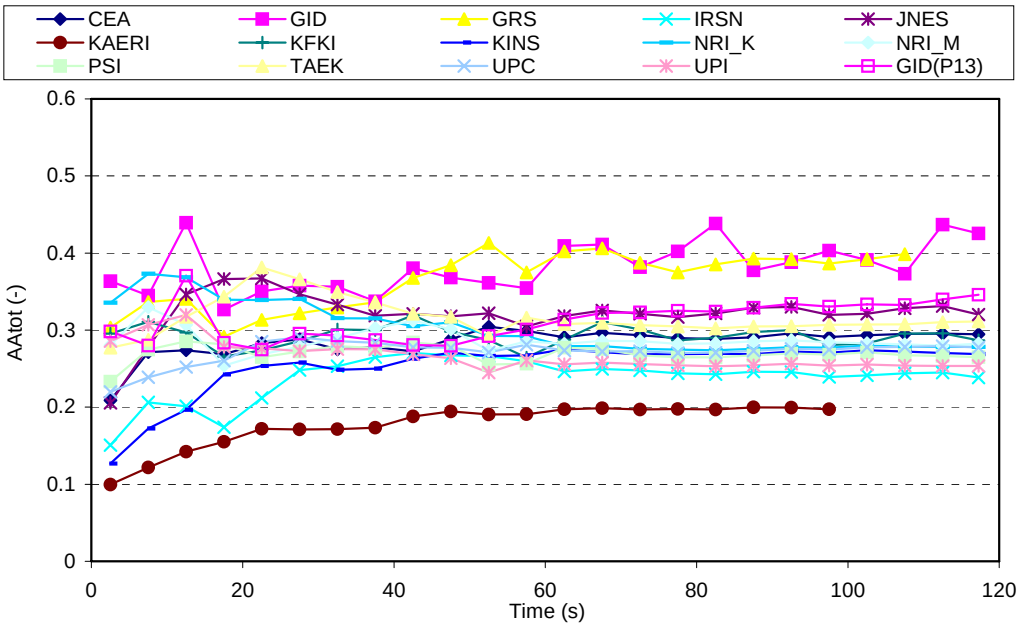

Figure 24 Total accuracy trend obtained with original FFTBM

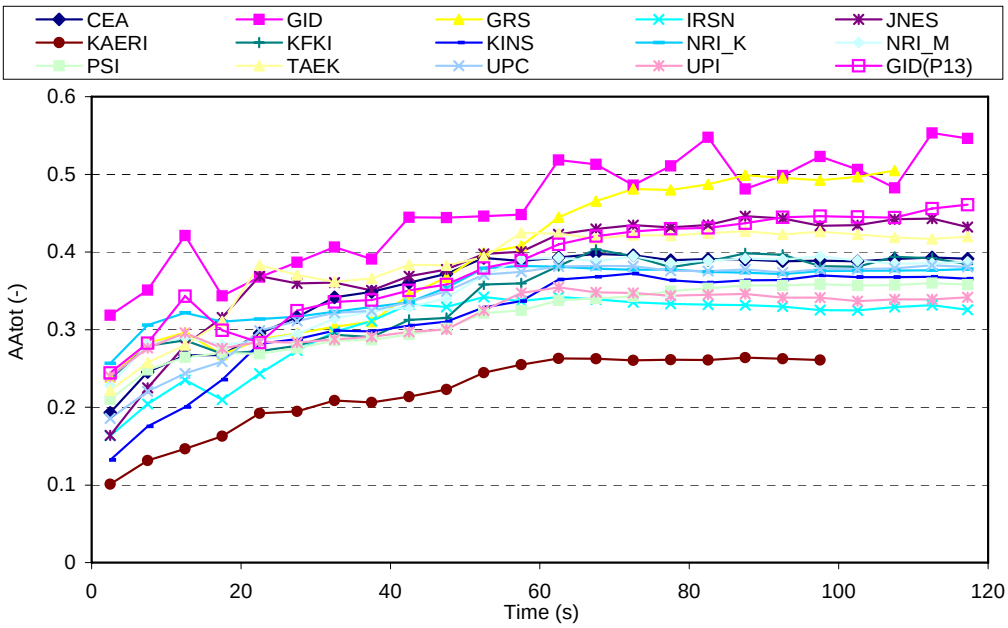

Figure 25 Total accuracy trend obtained with FFTBM improved by signal mirroring

To show that P13 contributes to oscillations, total accuracy without consideration of P13 was calculated (labeled GID(P13) in Figures 24 and 25). The figures show that the GID calculation is not still oscillating and that the accuracy is comparable to that of the lower ranked calculations. The second calculation judged to be poor is the GRS calculation. The quantitative assessment in Phase II of the BEMUSE program also reached this conclusion. The primary reason for this is the rod surface temperature calculation, even though the reference calculation of the GRS maximum temperature was considered to be good in the framework of BEMUSE Phase III. Not considering the rod surface temperatures in the total accuracy analysis, the GRS calculation is again comparable to the lower ranked calculations (e.g., those of JNES and TAEK). On the other hand, without the consideration of rod surface temperature in the total accuracy analysis, the KAERI calculation is comparable to the upper ranked calculations. This means that, in principle, the calculations are thermal-hydraulically very close to each other, and the curves are bundled together, with no calculation showing clear superiority or significantly deviating in accuracy.

This finding indicates that the rod surface temperature variables are the major contributors to inaccuracy. However, these variables are also the most sensitive and uncertain. This makes it difficult to judge the uncertainty based on reference calculations, as the uncertainty bounds are probably different for different codes and users. In principle, the reference calculations with narrow uncertainty bounds should be more accurate, in order to bound the experimental data, than those calculations with larger uncertainty bounds. The case described above actually happened in the uncertainty analysis performed later in BEMUSE Phase III (Ref. 11). According to results from Table 10 of the BEMUSE Phase III report (Ref. 11), the GRS, PSI, and UPC have a narrow width of uncertainty band, and the reference calculations for PSI and UPC were underestimated with respect to maximum cladding temperature, while the GRS calculation was slightly underestimated before 30 seconds and overestimated after 30 seconds. The PSI and UPC calculations were the only ones out of 10 calculations that did not envelop the experimental data. This is another example of the usefulness of quantitative results in analyzing the calculated data.

Although the accuracy trend is important, the final judgment of the code calculation accuracy is normally based on values for the whole transient time intervals. Tables 7 and 8, respectively, collect the accuracy measures based on D'Auria AA (extended original FFTBM) and AA_m obtained by mirroring. The tables show that the number of variables with discrepancies more or less corresponds to the ranking of calculations. The smallest contributors to inaccuracy in most cases were the SG downcomer bottom fluid temperatures. The largest contributors to inaccuracy were clad temperatures. The exception is the GID calculation by P13 because the signal was not properly prepared in the time domain. In the case of the KINS calculation, the largest contributor to inaccuracy is P5, as Figure 8 clearly shows. This variable has also been marked as unqualified in the BEMUSE qualitative analysis. In the KAERI calculation, the largest contributor to inaccuracy is the variable P7. The KAERI value of VA_{min} is the smallest among all calculations.

A comparison of AA_{tot} values in Tables 7 and 8 reveals that the absolute values of D'Auria AA_{tot} and AA_{tot} obtained by mirroring are different. However, the ranking between the calculations remains unchanged. The results also show that the differences in accuracy between different calculations are small except for the KAERI, GID, and GRS calculations as mentioned above. The KAERI calculation is judged as better than the others because of the rod surface temperatures. The reason for selecting more surface temperatures in the quantitative analysis

was to emphasize the three-dimensional rod surface distribution. BEMUSE participants agreed on this selection.

Table 7 New Accuracy Measures Obtained with Extended Original FFTBM

	Time Interval 0–119.5 s					
Calculations	AA_{tot}	VA_{max}	Variable with VA_{max}	VA_{min}	Variable with VA_{min}	ND
CEA	0.295	0.039	P8	0.854	P19	5
GID	0.437	0.037	P4	1.389	P13	9
GRS	0.398	0.030	P8	1.274	P19	7
IRSN	0.239	0.033	P2	0.581	P16	3
JNES	0.320	0.079	P11	0.988	P19	5
KAERI	0.197	0.028	P2	0.374	P7	0
KFKI	0.287	0.017	P8	1.149	P19	5
KINS	0.269	0.037	P8	0.707	P5	5
NRI-K	0.278	0.027	P11	1.028	P19	4
NRI-M	0.282	0.019	P8	1.425	P19	4
PSI	0.265	0.032	P11	0.724	P19	4
TAEK	0.311	0.037	P2	1.175	P19	5
UPC	0.277	0.026	P8	1.140	P19	3
UPI	0.254	0.020	P2	0.940	P19	3

Table 8 New Accuracy Measures Obtained with FFTBM Improved by Signal Mirroring

	Time Interval 0–119.5 s					
Calculations	AA_{tot}	VA_{max}	Variable with VA_{max}	VA_{min}	Variable with VA_{min}	ND
CEA	0.391	0.043	P8	1.196	P19	6
GID	0.560	0.084	P4	1.514	P13	10
GRS	0.505	0.027	P8	1.847	P18	7
IRSN	0.326	0.040	P8	0.661	P16	5
JNES	0.432	0.073	P8	1.398	P19	7
KAERI	0.261	0.033	P2	0.547	P7	3
KFKI	0.384	0.022	P8	1.601	P19	5
KINS	0.366	0.037	P8	0.981	P5	6
NRI-K	0.378	0.041	P8	1.440	P19	5
NRI-M	0.387	0.023	P8	1.948	P19	6
PSI	0.358	0.049	P8	1.044	P19	5
TAEK	0.420	0.041	P8	1.584	P19	5
UPC	0.381	0.028	P8	1.657	P19	7
UPI	0.341	0.027	P2	1.216	P19	4

However, an examination of the non-rod temperature variable contribution to the total accuracy based on VA reveals that, as shown in Table 9, the KFKI, NRI-K, and UPI calculations are even better than the KAERI calculation, while those of NRI-M and PSI are comparable. If considering just the rod-temperature contribution, the KAERI calculation obtained the highest accuracy, and only the IRSN calculation is comparable. This also explains why the KAERI calculation was judged as the best and IRSN as the second best (both with D'Auria AA_{tot} and AA_{tot} obtained by

mirroring). Nevertheless, the selection of variables is based on subjective judgment, as is, at least in part, the selection of the weights (fixed in the analysis). For the uncertainty evaluation, it is very important that the reference calculations are correct, as the uncertainty bounds are added to the reference calculation. In this respect, the KAERI and IRSN calculations would be expected to have the best reference calculations of rod surface temperatures and are the best candidates to bound the experimental data when adding uncertainty bounds (Table 10 in the BEMUSE Phase III report (Ref. 11) confirms this for both, except that in the case of IRSN, the width of the uncertainty band is medium, and therefore, at around 50 seconds the IRSN upper bound is slightly lower than the experimental data). As Figure 17 shows, the opposite occurs in the case of the primary side total mass where the KAERI calculation is among the least accurate during rod heatup. However, the KAERI calculation accurately predicts a small heatup of average rod temperatures, while most participants predicted a significant core heatup (see Table 8). This establishes the superiority of the KAERI calculation, but it is less important in terms of the uncertainty analysis for the maximum rod surface temperature in the hot rod.

The third parameter treated in the sensitivity analysis was the upper plenum pressure, which was not selected for the FFTBM analysis. Nevertheless, the pressure trend is practically the same as the trend for hot leg pressure (the data for upper plenum pressure was obtained separately for sensitivity analysis). In a comparison of the accuracy of the hot leg pressure, the KAERI calculation is comparable to the GID calculation (i.e., the best and the worst calculations produce comparable results). This example illustrates that, besides the total accuracy, the accuracies of variables selected for the uncertainty analysis are important. The appendix to this report shows the obtained values of accuracy measures for the time interval 0–100 seconds. The results differ slightly from the results for the whole time interval. However, as KAERI provided data for 100 seconds, these data are presented for direct comparison purposes. Appendix Tables I-1 through I-14 show accuracy measures obtained by the original FFTBM, while Tables II-1 through II-14 show results obtained with FFTBM improved by signal mirroring. Each table presents results for one calculation. Shown are the values of AA, VA, *I* for time shift detection, based on AA^M (Ref. 1), AMMIN (AA^M is AA based on magnitudes, not considering phase (Ref. 1)), fraction A0 (contribution of zero frequency component in percentage), AA_{exp} and AA_{dif}. Dividing AA_{dif} by AA_{exp} produces the value for AA (see Eq. 28). The information for WF is not shown, as those data are not useful when all frequency components are used for the AA calculation (there is no frequency cut). The time shift was indicated by index*I* only in the case of break flow rate (P9) for three calculations (GRS, GID, and KAERI). Figure 26 shows the break flow predictions in the first 5 seconds. The experimental break flow is delayed 0.32 seconds even though the break opens at 0 seconds. The time shift is small, but it has a large influence on the accuracy. For the other calculations, the time shift in the break flow is not detected because the data were given every 0.5 seconds, causing only a ramp increase of the flow instead of a step increase in the flow rate, which is only half of the experimental flow rate (JNES, UPC). This example shows the need for a sufficient number of data points to more precisely quantify the accuracy when some important phenomena occur rapidly.

Table 9 Accuracy Contribution from Non-Rod Surface Temperature Variables and Contribution from Rod Surface Temperature Variables

	D'Auria				Mirroring			
	sum VA		average VA		sum VA		average VA	
	P1-P14	P16, P18-P20	P1-P14	P16, P18-P20	P1-P14	P16, P18-P20	P1-P14	P16, P18-P20
CEA	2.93	1.99	0.209	0.497	3.88	2.65	0.277	0.662
GID	4.34	2.17	0.310	0.543	5.33	3.00	0.380	0.751
GRS	3.48	3.09	0.249	0.774	3.99	4.27	0.285	1.068
IRSN	2.59	1.43	0.185	0.358	3.61	1.89	0.258	0.472
JNES	3.15	2.19	0.225	0.548	4.21	3.00	0.300	0.749
KAERI	2.29	1.06	0.163	0.265	3.05	1.38	0.218	0.346
KFKI	1.99	2.66	0.142	0.665	2.61	3.61	0.186	0.903
KINS	2.87	1.65	0.205	0.414	3.92	2.23	0.280	0.557
NRI-K	1.91	2.60	0.137	0.650	2.62	3.51	0.187	0.877
NRI-M	2.32	2.32	0.165	0.581	3.28	3.10	0.234	0.775
PSI	2.32	2.05	0.166	0.513	3.13	2.77	0.224	0.693
TAEK	2.45	2.64	0.175	0.661	3.37	3.51	0.241	0.878
UPC	2.86	1.79	0.204	0.448	3.91	2.47	0.279	0.617
UPI	2.11	2.06	0.151	0.515	2.97	2.66	0.212	0.666

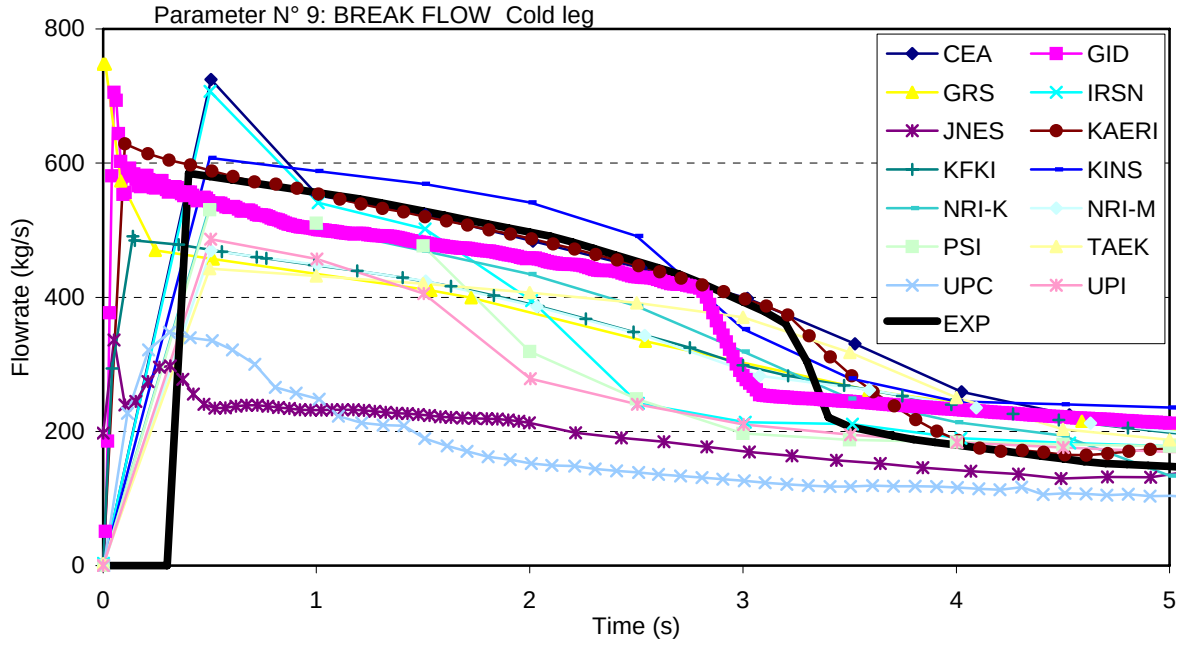

Figure 26 Time shift of break flow rates

7.4 Criterion for Using Moving Average

When trends oscillate greatly (e.g., the pressure drops in P13), special treatment is needed. To correctly reproduce the experimental signal by linear interpolation, many points are needed. This is achieved by increasing the maximum frequency component of the signal. However, it makes no sense to increase the number of points, as some cases have a sampling frequency 30 times smaller than the calculated data. When many points are used, the main contribution to the amplitude spectrum comes from the oscillations (very often noise) in the experimental signal for which the calculated data have no information. The correct procedure is therefore to smooth the data. Smoothing data removes random variations and shows trends and cyclic components. The simplest way to smooth data is by taking averages. This is done by use of the moving average of the experimental signal. Mathematically, the moving average is an example of a convolution of the input signal with a rectangular pulse having an area of 1.

Without use of the moving average, AA varies around a certain value. In the presented case for P13, the value of AA is close to 1 (see Figure 18) because the calculated values are much smaller than the experimental values. Variations in AA are the consequence of inappropriately prepared experimental data for the FFTBM analysis. The problem of the oscillatory signal was less significant in the past, because the original FFTBM limited the number of data points to 1,000, and data reduction was needed when this value was exceeded. Thus, data reduction is another possibility for use in partially smoothing the signal and thereby increasing the accuracy by eliminating some noise. However, as shown by Figure 4(e) in (Ref. 12), the D'Auria AA still varies because the moving average was not used. The reason is that, by increasing the time interval and not increasing the number of points, the amplitude spectrum changes as the signal between two consecutive data points is not a monotonic function (it oscillates). This gives a different amplitude spectrum of the experimental and difference signal. When moving average was used in the case of the P13 experimental signal, the AA values no longer oscillate in phase because of AA_{exp}, as shown in Figure 27. This suggests that the observation of oscillations being in phase in the calculated AAs indicates that moving average should be used. Figures 27(a) and 27(b) show a sudden increase in AA in the CEA and JNES calculations. The reason for this increase is the pressure spikes clearly shown in Figure 18. Each spike significantly deteriorates the results. Finally, FFTBM was able to detect the deviation in the NRI-K calculation at the end of the transient.

Another important finding is that the mismatch between the experimental data and the calculations for variable P13 is present from the very beginning of the transient, as shown in Figure 28. Only the GID calculation reproduced the frequency of oscillations in the first second. However, because the peaks were too high, the calculation was not very accurate. Use of moving average removes the large oscillations from the experimental signal (EXP(ma)), while in the GID(ma) calculation, the oscillations still remain in the beginning of the transient. Later (at approximately 15 seconds), the pressure drop stabilizes and the values oscillate around their mean values. This means that the transient related to the pressure drop has more or less ended. Table 10 shows that the mean values are well below the experimental value and justify an AA above 0.5, as shown in Figure 27.

Table 10 Average SG Pressure Drops in Time Interval 15–120 Seconds

Average Pressure Drop (kPa)														
EXP	CEA	GID	GRS	IRSN	JNES	KAERI	KFKI	KINS	NRI-K	NRI-M	PSI	TAEK	UPC	UPI
13.07	2.65	1.46	2.61	2.25	2.93	0.65	3.44	0.37	1.05	4.34	4.33	1.75	0.67	3.23

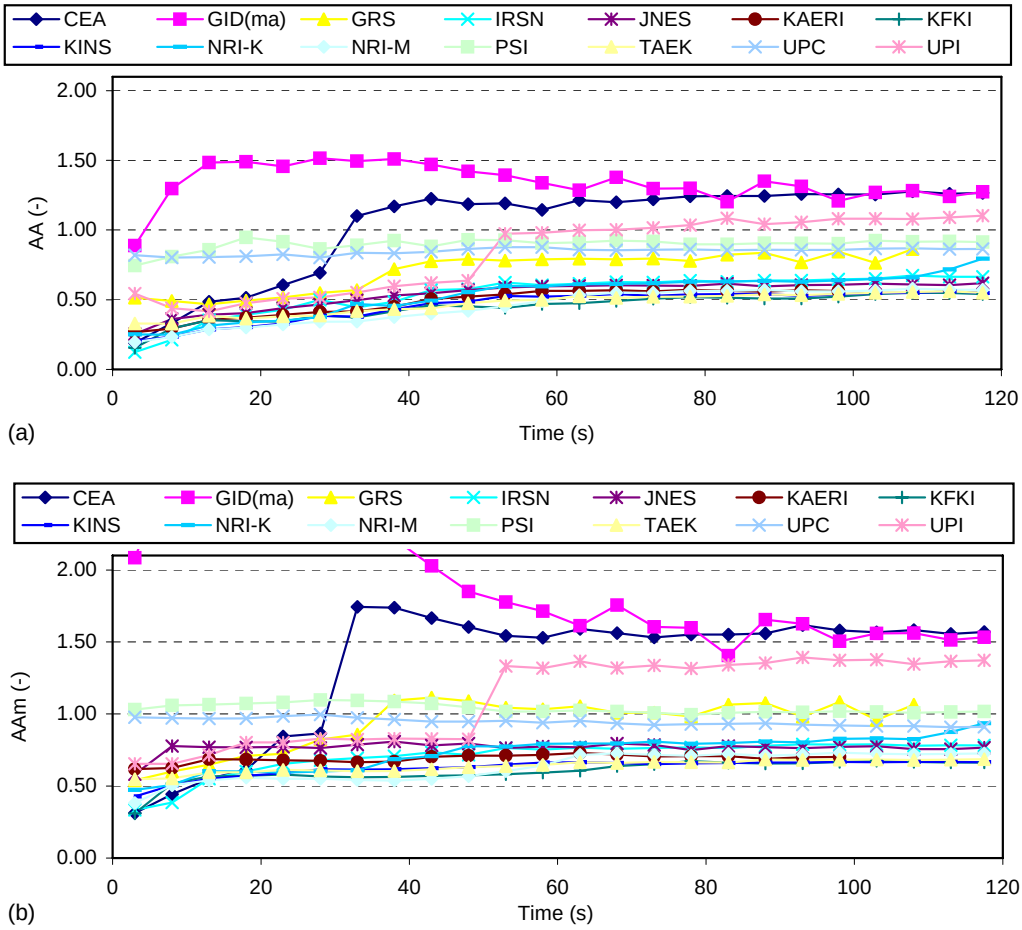

Figure 27 Accuracy trends for SG pressure drop—UT PS using moving average for the experimental signal

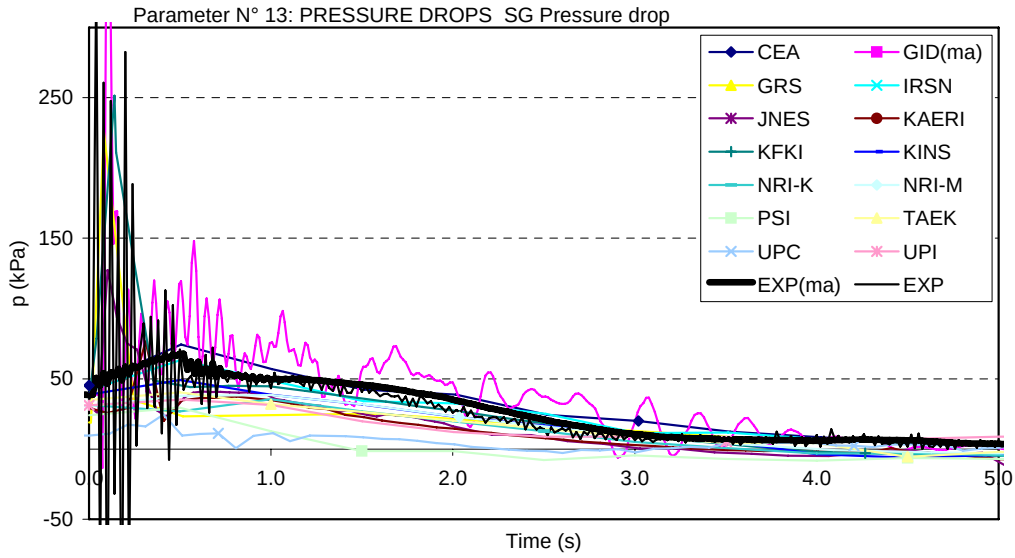

Figure 28 Time trends for SG pressure drop—UT PS for initial 5 seconds

7.5 Comparison of Fast Fourier Transform Based Method and Automated Code Assessment Program

Tables 11 and 12 show the comparison of FFTBM and Automated Code Assessment Program (ACAP) (Ref. 13) figures of merit for the pressurizer pressure (P4) and the hot rod temperature (P16). This comparison was made for the independent assessment that FFTBM provides for consistent figures of merit. The calculations are sorted according to AA_m in ascending manner. For pressurizer pressure, it can be seen that AA_m, AA, mean square error (MSE), and cross-correlation coefficient (XCC) figures of merit agree well. The only difference is that MSE and XCC indicate that all calculations of pressurizer pressure are very good, while FFTBM shows that some are not so accurate and some do not even fulfill the original FFTBM primary pressure criterion. As the pressure criterion was developed without consideration of the edge effect, care must be taken in its use, as indicated by the ACAP results.

Finally, D'Auria fast Fourier transform (DFFT) and continuous wavelet transform (CWT) figures of merit do not help much in this case. For hot rod temperature, AA_m, AA, MSE, and XCC figures of merit agree well. The XCC figure of merit is in especially good agreement with the AA_m. When comparing the UPC and TAEK calculations, FFTBM slightly favors the UPC calculation, while ACAP gives comparable values. The qualitative analysis of dryout occurence reported in Table 13 of the BEMUSE Phase II Report (Ref. 10) showed, that the UPC calculation receives three excellent and one minimal mark, while the TAEK calculation receives two excellent, one reasonable, and one minimal mark. One parameter representing dryout occurrence is peak cladding temperature and for it the UPC calculation is qualitatively judged better than TAEK calculation. These BEMUSE results support the FFTBM judgments for cladding temperature. Examination of AA_m in Figure 20(c) shows that, in the initial period of 40 seconds, the UPC calculation is significantly better because of the TAEK calculation's large overprediction of cladding temperature.

Table 11 Comparison of FFTBM and ACAP Figures of Merit for Pressurizer Pressure (P4) in Time Interval 0–119.5 Seconds

P4	FFTBM		ACAP			
Calculation	AA_m	AA	DFFT	MSE	XCC	CWT
GID	0.076	0.034	0.194	1.000	1.000	0.154
GRS (110 s)	0.079	0.032	0.132	1.000	0.999	0.008
NRI-M	0.082	0.034	0.173	1.000	0.999	0.116
KFKI	0.085	0.036	0.223	1.000	0.999	0.059
KINS	0.111	0.047	0.173	0.999	0.999	0.148
NRI-K	0.129	0.051	0.194	1.000	0.999	0.179
KAERI (100 s)	0.159	0.062	0.168	0.999	0.999	0.008
TAEK	0.167	0.070	0.134	0.998	0.997	0.126
PSI	0.230	0.093	0.082	0.998	0.993	0.006
CEA	0.237	0.096	0.129	0.998	0.994	0.140
IRSN	0.244	0.097	0.128	0.998	0.995	0.220
UPI	0.275	0.119	0.110	0.997	0.992	0.069
JNES	0.305	0.123	0.089	0.996	0.983	0.091
UPC	0.458	0.186	0.096	0.991	0.972	0.053

AA—average amplitude, m—mirroring, DFFT—D'Auria fast Fourier transform, MSE—mean square error, CWT—continuous wavelet transform, XCC—cross-correlation coefficient

Table 12 Comparison of FFTBM and ACAP Figures of Merit for Rod Surface Temperature in the Hot Rod in the Middle of the Core (P16) in Time Interval 0–119.5 Seconds

P16	FFTBM		ACAP			
Calculation	AA_m	AA	DFFT	MSE	XCC	CWT
KAERI (100 s)	0.313	0.285	0.245	0.989	0.992	0.020
NRI-M	0.375	0.337	0.197	0.984	0.987	0.193
UPI	0.388	0.347	0.228	0.988	0.973	0.171
UPC	0.409	0.356	0.206	0.982	0.960	0.106
KFKI	0.442	0.374	0.203	0.983	0.968	0.006
KINS	0.451	0.396	0.182	0.980	0.972	0.010
GID	0.452	0.391	0.208	0.982	0.962	0.055
JNES	0.488	0.429	0.181	0.968	0.962	0.055
TAEK	0.504	0.429	0.207	0.981	0.967	0.004
IRSN	0.555	0.487	0.158	0.948	0.883	0.043
NRI-K	0.578	0.511	0.150	0.938	0.853	0.049
PSI	0.600	0.515	0.152	0.940	0.832	0.000
CEA	0.616	0.544	0.151	0.929	0.841	0.055
GRS (110 s)	0.708	0.620	0.149	0.901	0.780	0.000

AA—average amplitude, m—mirroring, DFFT—D'Auria fast Fourier transform, MSE—mean square error, CWT—continuous wavelet transform, XCC—cross-correlation coefficient

7.6 Correction Factors

The acceptability criteria for the proposed FFTBM improved by signal mirroring need to be defined based on several calculations. The obtained results suggest slightly higher acceptability limits than for the original FFTBM. Section 4.4 presents the criteria for the original FFTBM. The criteria for the improved FFTBM do not currently exist, but, for now, the following approach can be taken: correct the AA, calculated with the original FFTBM, using the correction factors obtained by comparing AA and AA_m for the whole time interval (see Table 13), and use the traditional acceptability limits of the original FFTBM method.

Using this method, no special and more restrictive criterion for the primary pressure would be needed (this criterion was difficult to satisfy for transients where the edge was not present). The restrictive pressure criterion may have been set based on pressure trends during small-break LOCAs in facilities simulating typical PWRs (high initial pressure and large pressure drop and, therefore, high edge). When tests of different facilities were simulated, there were difficulties in satisfying the primary pressure criterion. The first example is the accuracy quantification of four standard problem exercises (SPEs) organized by the International Atomic Energy Agency (IAEA) (Ref. 14). Among the conclusions of this study, which considers only the PS pressure, was that in the case of SPE-3, the calculation is clearly unacceptable (the AA was 0.31) and that more complex transients lead to worse results than does the simple transient. As the report on this IAEA study (Ref. 14) shows no plots, no further conclusion can be reached except that the pressure drop (edge) is smaller than in a typical PWR. In other words, the initial pressure in this test is lower than in the typical PWR test. By lowering the pressure edge, the values of AA increase. This is better illustrated in the recent application of FFTBM to heavy-water reactors. In the study (Ref. 12), all participants satisfied the acceptance criterion for the total accuracy $K<0.4$, while the primary pressure criterion was not met. In the blind accuracy calculation, the AA value for primary pressure was 0.117 in the best calculation. The header 7 pressure with initial pressure around 10 MPa was selected as a variable representing the primary pressure. In the open accuracy analysis, a representative from Italy proposed the header 6 pressure. The

initial value of this pressure was around 12 MPa. For most of the participants, the value of AA was below 0.1, primarily because of the higher pressure edge effect (the best AA was 0.074).

Table 13 shows that the largest correction factors are for P1, P3, and P4 (all pressures) and P11 (flow integral). For all other variables, the difference was ±20 percent.

Table 13 Correction Factors for Accuracy Judgment by Original FFTBM for LOFT L2-5 Test

Variable/ Calc.	P1	P2	P3	P4	P5	P6	P7	P8	P9	P10	P11	P12	P13	P14	P16	P18	P19	P20
CEA	1.4	0.9	1.8	2.1	1.2	1.3	0.9	0.9	0.9	0.9	1.4	1.0	0.9	0.8	0.9	1.1	1.2	1.2
GID	1.5	1.1	1.2	1.9	1.3	1.2	1.3	0.8	0.8	0.9	1.0	0.9	0.9	0.8	1.0	1.1	1.2	1.2
GRS[a]	1.5	0.9	1.8	2.0	1.3	1.3	0.8	0.8	0.8	0.9	1.1	0.7	0.8	0.8	0.9	1.2	1.2	1.2
IRSN	1.5	1.0	1.8	2.1	1.3	1.3	1.2	0.9	0.9	0.9	1.4	1.0	0.9	0.8	0.9	1.1	1.2	1.2
JNES	1.6	0.5	1.8	2.1	1.1	1.3	1.2	0.6	0.9	0.9	1.5	1.0	0.9	0.8	0.9	1.1	1.2	1.2
KAERI[b]	1.6	1.0	1.6	2.1	1.1	1.3	1.2	0.6	0.8	0.9	1.1	1.0	0.9	0.8	0.9	1.1	1.2	1.1
KFKI	1.6	0.8	1.9	1.9	1.2	1.3	1.3	1.1	0.8	0.9	1.1	0.9	0.9	0.8	1.0	1.1	1.2	1.2
KINS	1.5	1.0	1.6	2.0	1.2	1.2	1.2	0.8	0.8	0.9	1.2	1.0	0.9	0.8	0.9	1.1	1.2	1.2
NRI-1	1.6	1.1	1.2	2.1	1.3	1.3	1.2	0.8	0.8	0.8	1.7	1.2	0.9	0.8	0.9	1.1	1.2	1.2
NRI-2	1.4	0.9	1.9	2.0	1.3	1.3	1.2	1.0	0.8	0.9	1.6	1.2	0.9	0.8	0.9	1.1	1.1	1.2
PSI	1.5	0.9	2.0	2.1	1.3	1.2	1.2	0.8	0.8	0.9	2.0	0.9	0.9	0.8	1.0	1.1	1.2	1.2
TAEK	1.5	0.9	1.9	2.0	0.9	1.2	1.2	0.7	0.9	0.9	1.3	1.3	0.9	0.8	1.0	1.1	1.1	1.2
UPC	1.5	0.9	1.2	2.0	1.2	1.3	1.2	0.9	0.9	0.8	1.5	1.4	0.8	0.8	1.0	1.1	1.2	1.2
UPI	1.5	1.1	1.7	1.9	1.2	1.3	1.2	0.8	0.9	0.9	1.6	1.3	0.9	0.8	0.9	1.1	1.1	1.2
average	1.5	0.9	1.7	2.0	1.2	1.3	1.2	0.8	0.8	0.9	1.4	1.1	0.9	0.8	0.9	1.1	1.2	1.2

[a] For time interval 0–110 s

[b] For time interval 0–100 s

7.7 Discussion of the Results

The FFTBM improved by signal mirroring was used in the LOFT L2-5 test to demonstrate the consistent judgment of code calculations. For the LOFT L2-5 test calculation, the original FFTBM and the FFTBM improved by signal mirroring reach similar conclusions. Nevertheless, this holds only for the time interval of the whole transient duration. A time-dependent analysis clearly shows the differences between AA and AA_m. In the analysis using the original FFTBM, the edge effect has too much impact on the results, as it first increases and then decreases value (triangular shape), while in the analysis using the FFTBM improved by signal mirroring, the edge effect is eliminated. Generally, the AA increases when there are discrepancies. Once the calculated results begin to approach the experimental values, the AA slowly decreases. However, if the experimental signal approaches steady-state conditions while the calculated signal still changes its shape, the AA does not decrease.

The quantitative analysis performed in this study supports most of the conclusions reached independently in the BEMUSE program. First, the BEMUSE qualitative conclusions are in agreement with the quantitative judgment. FFTBM judged both calculated variables designated as unqualified in the BEMUSE qualitative analysis (i.e., the SG secondary pressure of the GID calculation and the core inlet liquid temperature of the KINS calculation), to be very poor calculations.

The quantitative results also confirm and clarify the conclusions for RTA from the qualitative analysis in BEMUSE Phase II. A good example is the comparison of the UPC and TAEK calculations of hot rod temperature (P16). FFTBM slightly favors the UPC calculation, while ACAP shows comparable values. It also becomes clear that extending FFTBM with the capability to calculate accuracy as a function of time is indispensable in such studies. The analyst can see the contribution of each discrepancy to the AA. In the case of hot rod temperature, the most important contributor to AA is the time of core quench. When not calculating accuracy as a function of time, the reasons for discrepancies can be misleading if the analyst looks only at the results for the whole time interval. For example, the BEMUSE Phase III Report (Ref. 11) mentions that GRS, KAERI, KINS, and UNIPI had good reference calculations of maximum cladding temperatures. However, the quantitative analysis results of BEMUSE Phase II (Ref. 10] seem to contradict that statement, as the GRS prediction of hot rod temperature was judged to be the least accurate. However, the AA_m for the GRS calculation in the present study shows that the GRS calculation of hot rod temperature was in good agreement in the time period before quench, while later agreement declined because the time of core quench was not accurately predicted. Also, in BEMUSE Phase III, GRS provided a calculation with improved prediction of core quench time.

The results also show that the average contribution to AA is 55 percent for non-rod surface temperature variables and 45 percent for rod surface temperature variables. This finding indicates that the rod surface temperature variables are the major contributors to inaccuracy. However, these are also the most sensitive and uncertain variables. Therefore, it is difficult to judge the uncertainty based on reference calculations, as the uncertainty bounds may differ for different codes and users. In principle, the reference calculations with narrow uncertainty bounds should be more accurate (in order to bound the experimental data) than the calculations with larger uncertainty bounds. The results of BEMUSE Phase III confirm this hypothesis.

Finally, the reason for selecting more surface temperatures in the quantitative analysis was to emphasize the three-dimensional rod surface distribution. BEMUSE participants agreed to this selection. The KAERI calculation, as well as those of GRS, KINS and UPI, for hot rod calculation were judged as good reference calculations in BEMUSE Phase III. The BEMUSE qualitative analysis even found that the maximum differences with respect to the experimental value of 1,078 K were obtained by NRI-M (1,250 K) and by KAERI (980 K). However, the KAERI calculation better predicted a small heatup of average rod temperatures than the calculations of most other participants, which predicted a significant core heatup (see Table 8). This established the superiority of the KAERI calculation, but it is less important in the uncertainty analysis for the maximum rod surface temperature in the hot rod only. As noted in Figure 17, for the primary-side total mass, the KAERI calculation was among the least accurate during rod heatup. This example illustrates that both qualitative and quantitative analyses are needed for objective judgment about the quality of a calculation.

8. CONCLUSIONS

Two decades ago, under the aegis of CSNI, work began on the development of methods for code accuracy quantification. In an attempt to develop the figure of merit to characterize the accuracy of code prediction and to compare two or more calculations, the original FFTBM was proposed. The FFTBM became widely used for code accuracy quantification of PS thermal-hydraulic codes and was also included in the ACAP tool developed for U.S. Nuclear Regulatory Commission code consolidation purposes. However, a new figure of merit was proposed based on AA and WF. Recently, it was observed that the judged accuracy obtained by the original FFTBM was, in general, unreasonably high for monotonic variable trends (pressure blowdown, break flow integral) in comparison with other trends. Similarly, in calculating the time-dependent accuracy with the extended original FFTBM, the accuracy changed greatly during a fast increase or decrease in variables. The reason for this was identified as the nonphysical edge effect (influence of difference between the first and the last data point), which produces several harmonic amplitudes. Signal mirroring was proposed to eliminate the edge effect, which is a deficiency in the original FFTBM.

The FFTBM improved by signal mirroring was applied to the large-break LOCA test LOFT L2-5. The results show that the improved FFTBM judges the accuracy of variables reliably and consistently. For the LOFT L2-5 test, the results for the entire transient time interval obtained by the original FFTBM and by the FFTBM improved by signal mirroring qualitatively agree except for monotonic variables. The results for time-dependent accuracy with the FFTBM improved by signal mirroring show that the analyst can now find accurate information on how the discrepancies influence the accuracy. This information is needed to verify and clarify the conclusions made in the BEMUSE program.

The results obtained with FFTBM improved by signal mirroring have been useful in systematic evaluation of several code calculations. The method eliminates the nonphysical edge influence on accuracy, detects the time shifts between calculated and experimental data, detects the unqualified variables from the qualitative analysis, helps to independently verify the qualitative conclusions, and aids the analyst in judging the quality of code predictions. The method also contributes to uncertainty analysis, as a good reference calculation is as important as the determination of uncertainty bounds. The capability to calculate time-dependent accuracy helps the analyst to identify the variables that need further treatment in the time domain before the signal is quantitatively assessed. These findings lead to the conclusion that the FFTBM improved by signal mirroring realistically judges accuracy and is a generally applicable tool for quantitative assessment.

9. REFERENCES

1. Prošek, A., and Leskovar, M., "Application of FFTBM to Severe Accidents," *Int. Conf. Nuclear Energy for New Europe 2005*, Bled, Slovenia, September 5–8, 2005.
2. Prošek, A., and Mavko, B., "Quantitative assessment of time trends: Influence of time window selection," *Proc. 5th Int. Conf. on Nuclear Option in Countries with Small and Medium Electricity Grids*, Dubrovnik, Croatia, May 16–20, 2004.
3. Press, W.H., Teukolsky, S.A., Vetterling, W.T., and Flannery, B.P., *Numerical Recipes in Fortran 77: The Art of Scientific Computing*, Vol. 1, Chapter 12: "Fast Fourier transform," Second Edition, 2001, ISBN 0-521-43064-X.
4. Prošek, A., D'Auria, F., and Mavko, B., "Review of quantitative accuracy assessments with fast Fourier transform based method (FFTBM)," *Nuclear Engineering and Design*, 217 (1–2), 179–206, 2002.
5. D'Auria, F., Leonardi, M., and Pochard, R., "Methodology for the evaluation of thermal-hydraulic codes accuracy," *Proc. Int. Conf. on New Trends in Nuclear System Thermohydraulics*, Pisa, May 30–June 2, 1994.
6. Aksan, S.N., Bessette, D., Brittain, I., D'Auria, F., Gruber, P., Holmström, H.L.O., Landry, R., Naff, S., Pochard, R., Preusche, G., Reocreux, M., Sandervag, O., Städtke, H., Wolfert, K., and Zuber, N., "CSNI Code Validation Matrix of Thermo-Hydraulic Codes for LWR LOCA and Transients," CSNI Report No. 132, 1987.
7. Prošek, A., "Accuracy assessment of IAEA-SPE-4 predictions with improved FFTBM," presented at 2002 Winter Meeting of the American Nuclear Society, November 17–21, 2002, Washington. *Trans. Am. Nucl. Soc.*, Vol. 87, 199–201, 2002.
8. Prošek, A., and Leskovar, M., "Improved FFTBM by signal mirroring," IJS Report, Jožef Stefan Institute, IJS-DP-9336, Ljubljana, 2006.
9. Organisation for Economic Co-operation and Development/Nuclear Energy Agency (OECD/NEA), "CSNI International Standard Problems (ISP), Brief descriptions (1975–1999), NEA/CSNI/R(2000)5, OECD/NEA, Paris, France, 2000.
10. BEMUSE Phase II Report, "Re-Analysis of the ISP-13 Exercise, Post Test Analysis of the LOFT L2-5 Test Calculation," NEA/CSNI/R(2006)2, OECD/NEA, Paris, France, 2006, <http://www.nea.fr/html/nsd/docs/2006/csni-r2006-2.pdf>.
11. BEMUSE Phase III Report, "Uncertainty and Sensitivity Analysis of the LOFT L2-5 Test," NEA/CSNI/R(2007)4, OECD/NEA, Paris, France, 2007, <http://www.nea.fr/html/nsd/docs/2007/csni-r2007-4.pdf>.
12. Prošek, A., D'Auria, F., Richards, D.J., and Mavko, B., "Quantitative assessment of thermal-hydraulic codes used for heavy water reactor calculations," *Nuclear Engineering and Design* 236, 295–308, 2006.
13. Kunz, R.F., Kasamala, G.F., Mahaffy, J.H., and Murray, C.J., "On the automated assessment of nuclear reactor systems code accuracy," *Nuclear Engineering and Design*, 211, 245–272, 2002.
14. D'Auria, F., Eramo, A., Frogheri, M., and Galassi, G.M., "Accuracy quantification in SPE-1 to SPE-4," organized by IAEA, *Proc. Int. Conf. on Nuclear Engineering (ICONE-4)*, New Orleans, Louisiana, Vol. 3, 1996.

APPENDIX A

ACCURACY MEASURES FOR L2-5 TEST IN TIME INTERVAL 0–100 SECONDS

CONTENTS

I. ORIGINAL FAST FOURIER TRANSFORM BASED METHOD A-4

II. FAST FOURIER TRANSFORM BASED METHOD IMPROVED BY SIGNAL MIRRORING A-11

Tables

Table I-1 Accuracy Measures for CEA Calculation with Original FFTBM. A-4
Table I-2 Accuracy Measures for GID Calculation with Original FFTBM. A-4
Table I-3 Accuracy Measures for GRS Calculation with Original FFTBM. A-5
Table I-4 Accuracy Measures for IRSN Calculation with Original FFTBM. A-5
Table I-5 Accuracy Measures for JNES Calculation with Original FFTBM. A-6
Table I-6 Accuracy Measures for KAERI Calculation with Original FFTBM. A-6
Table I-7 Accuracy Measures for KFKI Calculation with Original FFTBM. A-7
Table I-8 Accuracy Measures for KINS Calculation with Original FFTBM. A-7
Table I-9 Accuracy Measures for NRI-K Calculation with Original FFTBM. A-8
Table I-10 Accuracy Measures for NRI-M Calculation with Original FFTBM. A-8
Table I-11 Accuracy Measures for PSI Calculation with Original FFTBM. A-9
Table I-12 Accuracy Measures for TAEK Calculation with Original FFTBM. A-9
Table I-13 Accuracy Measures for UPC Calculation with Original FFTBM. A-10
Table I-14 Accuracy Measures for UPI Calculation with Original FFTBM. A-10
Table II-1 Accuracy Measures for CEA Calculation with Improved FFTBM. A-11
Table II-2 Accuracy Measures for GID Calculation with Improved FFTBM. A-11
Table II-3 Accuracy Measures for GRS Calculation with Improved FFTBM. A-12
Table II-4 Accuracy Measures for IRSN Calculation with Improved FFTBM. A-12
Table II-5 Accuracy Measures for JNES Calculation with Improved FFTBM. A-13
Table II-6 Accuracy Measures for KAERI Calculation with Improved FFTBM. A-13
Table II-7 Accuracy Measures for KFKI Calculation with Improved FFTBM. A-14
Table II-8 Accuracy Measures for KINS Calculation with Improved FFTBM. A-14
Table II-9 Accuracy Measures for NRI-K Calculation with Improved FFTBM. A-15
Table II-10 Accuracy Measures for NRI-M Calculation with Improved FFTBM. A-15
Table II-11 Accuracy Measures for PSI Calculation with Improved FFTBM. A-16
Table II-12 Accuracy Measures for TAEK Calculation with Improved FFTBM. A-16
Table II-13 Accuracy Measures for UPC Calculation with Improved FFTBM. A-17
Table II-14 Accuracy Measures for UPI Calculation with Improved FFTBM. A-17

ABBREVIATIONS

A0	contribution of zero frequency amplitude component in percentage
AA	average amplitude
AMMIN	AA based on magnitudes, not considering phase
CEA	Commissariat à l'Energie Atomique
EDO	Experimental Design Office
GID	EDO "Gidropress"
GRS	Gesellschaft für Anlagen- und Reaktor Sicherheit (GRS) mbH
IRSN	Institut de Radioprotection et de Sûreté Nucléaire
JNES	Japan Nuclear Energy Safety
KAERI	Korea Atomic Energy Research Institute
KFKI	Központi Fizikai Kutató Intézet
KINS	Korea Institute of Nuclear Safety
NRI	Nuclear Research Institute
PSI	Paul Scherrer Institute
TAEK	Türkiye Atom Enerjisi Kurumu
UPC	Universitat Politècnica de Catalunya
UPI	University of Pisa
VA	variable accuracy

Subscripts

dif	difference
exp	experimental

I. ORIGINAL FAST FOURIER TRANSFORM BASED METHOD

Table I-1 Accuracy Measures for CEA Calculation with Original FFTBM

Calculation		Window 0–100 s						
CEA	Variable	AA	VA	*I*	AMMIN	fraction A0	AA_{exp}	AA_{dif}
1	P1	0.125317	0.138302	0.391783	0.090041	0.011398	0.092367	0.011575
2	P2	0.076823	0.055957	0.223395	0.062795	0.265155	0.024468	0.00188
3	P3	0.146882	0.162102	0.344385	0.109256	0.294715	0.039266	0.005767
4	P4	0.093479	0.103165	0.451952	0.064381	0.127436	0.127714	0.011939
5	P5	0.063593	0.1078	0.508101	0.042168	0.018878	3.004864	0.191089
6	P6	0.210502	0.356834	0.511556	0.139262	0.105666	3.172731	0.667867
7	P7	0.352581	0.59768	0.172971	0.300588	0.188643	3.202652	1.129194
8	P8	0.024746	0.041948	0.654144	0.01496	0.37236	2.132043	0.052759
9	P9	0.403267	0.089011	0.496651	0.269446	0.030703	4.072386	1.64226
10	P10	0.865179	0.190965	0.900228	0.455303	0.000864	1.146323	0.991775
11	P11	0.196551	0.140562	0.089063	0.180477	0.256126	20.907	4.109296
12	P12	0.355552	0.254271	0.053528	0.337487	0.290154	30.52846	10.85444
13	P13	0.955056	0.258234	0.4864	0.642529	0.046794	0.810833	0.774391
14	P14	1.439387	0.389191	0.742958	0.82583	0.03381	0.827981	1.191786
15	P16	0.536187	0.639085	1.274555	0.235733	0.110448	7.176047	3.847703
16	P18	0.499013	0.594777	0.303958	0.382691	0.122759	3.222118	1.607879
17	P19	0.716008	0.853415	0.309828	0.546643	0.106172	3.241802	2.321158
18	P20	0.224976	0.26815	0.539994	0.146089	0.013018	3.235821	0.727982
	total	0.291192			0.203854			

Table I-2 Accuracy Measures for GID Calculation with Original FFTBM

Calculation		Window 0–100 s						
GID	Variable	AA	VA	*I*	AMMIN	fraction A0	AA_{exp}	AA_{dif}
1	P1	0.082393	0.090931	0.42856	0.057676	0.099276	0.092367	0.00761
2	P2	0.587521	0.427943	0.142306	0.514329	0.060096	0.024468	0.014376
3	P3	0.179549	0.198153	0.193935	0.150384	0.078299	0.039266	0.00705
4	P4	0.032436	0.035797	0.183942	0.027397	0.133646	0.127714	0.004143
5	P5	0.076883	0.130329	0.470494	0.052284	0.074851	3.004864	0.231023
6	P6	0.197552	0.334882	0.610214	0.122687	0.030421	3.172731	0.626781
7	P7	0.28444	0.482171	0.728136	0.164594	0.0565	3.202652	0.910964
8	P8	NA	NA	NA	NA	NA	NA	NA
9	P9	0.669672	0.147812	3.68698	0.142879	0.017727	4.072386	2.727164
10	P10	0.645398	0.142455	0.552942	0.415597	0.00064	1.146323	0.739835
11	P11	0.170088	0.121637	0.008555	0.168645	0.193647	20.907	3.556032
12	P12	0.51294	0.366826	0.085147	0.472692	0.266781	30.52846	15.65928
13	P13	4.705256	1.272237	0.508289	3.119599	0.012783	0.810833	3.815177
14	P14	0.903181	0.244208	0.957425	0.461413	0.025216	0.827981	0.747817
15	P16	0.387229	0.461541	0.615652	0.239674	0.052967	7.176047	2.778777
16	P18	0.550875	0.656592	0.478891	0.372492	0.057033	3.222118	1.774985
17	P19	0.681829	0.812676	0.327268	0.513708	0.129185	3.241802	2.210353
18	P20	0.541346	0.645234	0.389418	0.389621	0.16777	3.235821	1.7517
	total	0.412993			0.347876			

Table I-3 Accuracy Measures for GRS Calculation with Original FFTBM

Calculation		Window 0–100 s						
GRS	Variable	AA	VA	*I*	AMMIN	fraction A0	AA_{exp}	AA_{dif}
1	P1	0.052953	0.05844	0.662973	0.031843	0.009996	0.092367	0.004891
2	P2	0.050301	0.036639	0.22727	0.040986	0.19617	0.024468	0.001231
3	P3	0.046279	0.051074	0.298897	0.035629	0.088406	0.039266	0.001817
4	P4	0.033329	0.036782	0.50958	0.022078	0.184502	0.127714	0.004257
5	P5	0.08395	0.142308	0.393803	0.060231	0.164754	3.004864	0.252257
6	P6	0.311528	0.528089	0.593336	0.195519	0.072503	3.172731	0.988394
7	P7	0.494108	0.83759	0.375228	0.359292	0.117685	3.202652	1.582455
8	P8	0.014927	0.025303	0.76339	0.008465	0.11638	2.132043	0.031824
9	P9	1.166972	0.257578	2.166693	0.368514	0.024264	4.072386	4.752361
10	P10	2.360307	0.520975	0.512743	1.560283	0.007589	1.146323	2.705674
11	P11	0.061591	0.044046	0.024338	0.060128	0.250394	20.907	1.287683
12	P12	0.401236	0.286941	0.112048	0.360808	0.142937	30.52846	12.24911
13	P13	0.634571	0.171579	0.222375	0.51913	0.075166	0.810833	0.514531
14	P14	0.948934	0.256579	0.501136	0.632144	0.026327	0.827981	0.7857
15	P16	0.603574	0.719404	0.98136	0.304626	0.103845	7.176047	4.331275
16	P18	1.100491	1.311682	0.284809	0.85654	0.228864	3.222118	3.54591
17	P19	1.050651	1.252278	0.256394	0.836243	0.287316	3.241802	3.406003
18	P20	0.347371	0.414034	1.213124	0.156959	0.106028	3.235821	1.124029
	total	0.386185			0.266193			

Table I-4 Accuracy Measures for IRSN Calculation with Original FFTBM

Calculation		Window 0–100 s						
IRSN	Variable	AA	VA	*I*	AMMIN	fraction A0	AA_{exp}	AA_{dif}
1	P1	0.130025	0.143498	0.484573	0.087584	0.003989	0.092367	0.01201
2	P2	0.046897	0.034159	0.436979	0.032636	0.080019	0.024468	0.001147
3	P3	0.139209	0.153634	0.284899	0.108342	0.316628	0.039266	0.005466
4	P4	0.094489	0.10428	0.473322	0.064133	0.129615	0.127714	0.012068
5	P5	0.1215	0.205962	0.644493	0.073883	0.099181	3.004864	0.365091
6	P6	0.127369	0.21591	0.580425	0.080592	0.027535	3.172731	0.404107
7	P7	0.237121	0.401957	0.733562	0.136782	0.119917	3.202652	0.759415
8	P8	0.024462	0.041467	1.08553	0.011729	0.277444	2.132043	0.052154
9	P9	0.577665	0.127504	0.581245	0.365323	0.020215	4.072386	2.352474
10	P10	0.848922	0.187377	0.914811	0.443345	0.000672	1.146323	0.973139
11	P11	0.219163	0.156733	0.157437	0.189352	0.243622	20.907	4.582038
12	P12	0.375776	0.268734	0.102863	0.340727	0.219851	30.52846	11.47185
13	P13	0.815834	0.22059	0.284124	0.635323	0.058437	0.810833	0.661505
14	P14	1.314795	0.355503	1.040841	0.644242	0.007083	0.827981	1.088626
15	P16	0.483709	0.576536	1.423791	0.199567	0.096902	7.176047	3.471116
16	P18	0.319801	0.381172	0.576156	0.202899	0.00901	3.222118	1.030435
17	P19	0.367894	0.438495	0.677712	0.219283	0.025382	3.241802	1.19264
18	P20	0.245802	0.292973	0.6941	0.145093	0.001653	3.235821	0.795372
	total	0.239249			0.146775			

Table I-5 Accuracy Measures for JNES Calculation with Original FFTBM

Calculation		Window 0–100 s						
JNES	Variable	AA	VA	*I*	AMMIN	fraction A0	AA_{exp}	AA_{dif}
1	P1	0.122946	0.135685	0.48258	0.082927	0.085675	0.092367	0.011356
2	P2	0.335039	0.244038	0.030705	0.325058	0.235355	0.024468	0.008198
3	P3	0.167406	0.184752	0.383059	0.12104	0.218683	0.039266	0.006573
4	P4	0.119752	0.13216	0.484763	0.080654	0.135031	0.127714	0.015294
5	P5	0.198729	0.336876	0.519914	0.13075	0.003326	3.004864	0.597153
6	P6	0.187297	0.317497	0.559091	0.120132	0.039849	3.172731	0.594243
7	P7	0.236295	0.400556	0.569417	0.150562	0.094883	3.202652	0.75677
8	P8	0.054401	0.092218	0.241136	0.043832	0.438121	2.132043	0.115985
9	P9	0.775679	0.171211	0.399577	0.554224	0.020599	4.072386	3.158866
10	P10	1.702814	0.375851	1.312278	0.736422	0.030234	1.146323	1.951974
11	P11	0.105292	0.075299	0.256486	0.083799	0.015916	20.907	2.201348
12	P12	0.32024	0.229018	0.066186	0.300361	0.28745	30.52846	9.776445
13	P13	0.641787	0.173531	0.202941	0.533515	0.076865	0.810833	0.520383
14	P14	0.922596	0.249457	0.579576	0.584078	0.078393	0.827981	0.763893
15	P16	0.429385	0.511787	0.601596	0.268098	0.093347	7.176047	3.081285
16	P18	0.483976	0.576854	0.38722	0.348882	0.161953	3.222118	1.559428
17	P19	0.839236	1.000292	0.359334	0.617388	0.205426	3.241802	2.720638
18	P20	0.460023	0.548304	0.381705	0.332938	0.207316	3.235821	1.488551
	total	0.319744			0.224198			

Table I-6 Accuracy Measures for KAERI Calculation with Original FFTBM

Calculation		Window 0–100 s						
KAERI	Variable	AA	VA	*I*	AMMIN	fraction A0	AA_{exp}	AA_{dif}
1	P1	0.087288	0.096332	0.391718	0.062719	0.08944	0.092367	0.008063
2	P2	0.037958	0.027648	0.448465	0.026205	0.033889	0.024468	0.000929
3	P3	0.106203	0.117207	0.324808	0.080165	0.169578	0.039266	0.00417
4	P4	0.062419	0.068887	0.334943	0.046758	0.193971	0.127714	0.007972
5	P5	0.090249	0.152986	0.440381	0.062656	0.135224	3.004864	0.271186
6	P6	0.104129	0.176514	0.531153	0.068007	0.092258	3.172731	0.330372
7	P7	0.220699	0.37412	0.652748	0.133535	0.160342	3.202652	0.706822
8	P8	0.035996	0.061019	0.823863	0.019736	0.082793	2.132043	0.076745
9	P9	0.660296	0.145743	2.780263	0.174669	0.015012	4.072386	2.688979
10	P10	0.275904	0.060899	0.428631	0.193125	0.064604	1.146323	0.316275
11	P11	0.283581	0.202801	0.102955	0.25711	0.149058	20.907	5.928834
12	P12	0.34792	0.248813	0.063313	0.327203	0.32659	30.52846	10.62145
13	P13	0.834978	0.225767	0.135456	0.735368	0.073896	0.810833	0.677028
14	P14	1.208797	0.326842	0.910195	0.632813	0.011395	0.827981	1.000861
15	P16	0.285422	0.340196	0.585273	0.180046	0.089465	7.176047	2.048199
16	P18	0.23898	0.284842	0.587302	0.150557	0.050674	3.222118	0.770021
17	P19	0.286482	0.34146	0.697671	0.16875	0.009565	3.241802	0.928718
18	P20	0.249246	0.297078	1.039658	0.1222	0.026631	3.235821	0.806516
	total	0.197175	3.549153		0.128862			

Table I-7 Accuracy Measures for KFKI Calculation with Original FFTBM

Calculation		Window 0–100 s						
KFKI	Variable	AA	VA	*I*	AMMIN	fraction A0	AA_{exp}	AA_{dif}
1	P1	0.057774	0.063761	0.57536	0.036674	0.037248	0.092367	0.005336
2	P2	0.056569	0.041204	0.16043	0.048748	0.157171	0.024468	0.001384
3	P3	0.061302	0.067654	0.358264	0.045132	0.138664	0.039266	0.002407
4	P4	0.036815	0.04063	0.434754	0.025659	0.21252	0.127714	0.004702
5	P5	0.086473	0.146585	0.310425	0.065988	0.190833	3.004864	0.259839
6	P6	0.106561	0.180638	0.669979	0.06381	0.057437	3.172731	0.33809
7	P7	0.2371	0.401922	0.752974	0.135256	0.133652	3.202652	0.75935
8	P8	0.010846	0.018386	0.440898	0.007527	0.102586	2.132043	0.023124
9	P9	0.626122	0.1382	2.024413	0.207023	0.009795	4.072386	2.549811
10	P10	0.505531	0.111583	0.551316	0.325872	0.006018	1.146323	0.579502
11	P11	0.077974	0.055763	0.012116	0.077041	0.235055	20.907	1.630206
12	P12	0.338304	0.241936	0.078292	0.31374	0.25799	30.52846	10.32789
13	P13	0.443754	0.119985	0.536681	0.288775	0.101078	0.810833	0.359811
14	P14	1.149578	0.31083	0.7396	0.660829	0.051934	0.827981	0.951829
15	P16	0.375135	0.447126	0.726839	0.217238	0.049237	7.176047	2.691984
16	P18	0.864375	1.030254	0.27805	0.676323	0.170749	3.222118	2.785118
17	P19	0.964233	1.149276	0.284851	0.750463	0.216703	3.241802	3.125853
18	P20	0.41048	0.489254	0.895625	0.216541	0.087653	3.235821	1.32824
	total	0.280832			0.193758			

Table I-8 Accuracy Measures for KINS Calculation with Original FFTBM

Calculation		Window 0–100 s						
KINS	Variable	AA	VA	*I*	AMMIN	fraction A0	AA_{exp}	AA_{dif}
1	P1	0.168472	0.185928	0.476759	0.114082	0.056312	0.092367	0.015561
2	P2	0.062127	0.045252	0.94452	0.03195	0.042204	0.024468	0.00152
3	P3	0.114574	0.126446	0.40403	0.081604	0.203451	0.039266	0.004499
4	P4	0.045347	0.050046	0.313436	0.034525	0.21457	0.127714	0.005791
5	P5	0.404041	0.684913	0.343472	0.300744	0.250958	3.004864	1.214089
6	P6	0.107093	0.18154	0.519998	0.070456	0.084119	3.172731	0.339778
7	P7	0.221937	0.376218	0.544943	0.143654	0.155087	3.202652	0.710788
8	P8	0.020428	0.034629	0.448388	0.014104	0.1526	2.132043	0.043554
9	P9	0.356403	0.078666	0.319726	0.270058	0.037326	4.072386	1.451409
10	P10	0.991559	0.21886	0.770879	0.559925	0.009363	1.146323	1.136647
11	P11	0.225419	0.161207	0.111286	0.202846	0.177744	20.907	4.712845
12	P12	0.404191	0.289055	0.068836	0.37816	0.373997	30.52846	12.33933
13	P13	0.804497	0.217525	0.222652	0.657993	0.074057	0.810833	0.652313
14	P14	1.02036	0.275891	0.638386	0.622784	0.035174	0.827981	0.844839
15	P16	0.381236	0.454398	0.615083	0.236048	0.091216	7.176047	2.73577
16	P18	0.376898	0.449228	0.518477	0.248208	0.03789	3.222118	1.214411
17	P19	0.498874	0.594612	0.64717	0.302868	0.146456	3.241802	1.617252
18	P20	0.373166	0.444779	0.650309	0.226119	0.122622	3.235821	1.207497
	total	0.270511			0.184817			

Table I-9 Accuracy Measures for NRI-K Calculation with Original FFTBM

Calculation		Window 0–100 s						
NRI-K	Variable	AA	VA	*I*	AMMIN	fraction A0	AA_{exp}	AA_{dif}
1	P1	0.121585	0.134183	0.516363	0.080182	0.000641	0.092367	0.01123
2	P2	0.052365	0.038142	0.427627	0.036679	0.065181	0.024468	0.001281
3	P3	0.116611	0.128694	0.349754	0.086394	0.007648	0.039266	0.004579
4	P4	0.049788	0.054947	0.357369	0.03668	0.116409	0.127714	0.006359
5	P5	0.060709	0.102911	0.447292	0.041947	0.041214	3.004864	0.182422
6	P6	0.091976	0.155914	0.586473	0.057975	0.0087	3.172731	0.291816
7	P7	0.230096	0.390048	0.589636	0.144748	0.105925	3.202652	0.736917
8	P8	0.024516	0.041558	0.289768	0.019008	0.25237	2.132043	0.052269
9	P9	0.353881	0.07811	0.270098	0.278625	0.000131	4.072386	1.44114
10	P10	0.542266	0.119691	0.672785	0.324169	0.007685	1.146323	0.621612
11	P11	0.034956	0.024999	0.299831	0.026893	0.012409	20.907	0.730828
12	P12	0.20557	0.147013	0.043338	0.197031	0.241056	30.52846	6.27575
13	P13	0.861551	0.232952	0.20411	0.715508	0.062481	0.810833	0.698574
14	P14	1.023881	0.276843	0.479195	0.692188	0.041479	0.827981	0.847755
15	P16	0.508028	0.605521	1.478403	0.204982	0.094797	7.176047	3.64563
16	P18	0.718596	0.856499	0.180847	0.608543	0.148526	3.222118	2.315401
17	P19	0.854162	1.018081	0.163245	0.734292	0.204253	3.241802	2.769024
18	P20	0.490546	0.584685	0.3975	0.351017	0.186828	3.235821	1.587318
	total	0.277266			0.201947			

Table I-10 Accuracy Measures for NRI-M Calculation with Original FFTBM

Calculation		Window 0–100 s						
NRI-M	Variable	AA	VA	*I*	AMMIN	fraction A0	AA_{exp}	AA_{dif}
1	P1	0.123309	0.136085	0.471286	0.08381	0.009574	0.092367	0.01139
2	P2	0.049085	0.035753	0.225015	0.040069	0.062695	0.024468	0.001201
3	P3	0.051749	0.057111	0.680975	0.030785	0.083493	0.039266	0.002032
4	P4	0.033993	0.037516	0.473792	0.023065	0.220267	0.127714	0.004341
5	P5	0.09961	0.168855	0.288013	0.077337	0.187218	3.004864	0.299316
6	P6	0.341229	0.578436	0.755438	0.194384	0.102755	3.172731	1.082627
7	P7	0.22555	0.382342	0.732847	0.130162	0.010833	3.202652	0.722358
8	P8	0.011393	0.019313	0.442575	0.007898	0.136854	2.132043	0.02429
9	P9	0.446399	0.098531	0.252345	0.35645	0.015976	4.072386	1.817908
10	P10	0.813306	0.179516	0.62854	0.499408	0.002026	1.146323	0.932312
11	P11	0.041246	0.029497	0.323663	0.031161	0.168476	20.907	0.862333
12	P12	0.248151	0.177463	0.071886	0.231508	0.273069	30.52846	7.575653
13	P13	0.839762	0.22706	0.152647	0.728552	0.052292	0.810833	0.680907
14	P14	1.005103	0.271766	0.579972	0.636153	0.036967	0.827981	0.832207
15	P16	0.337136	0.401834	0.517859	0.222113	0.092579	7.176047	2.419301
16	P18	0.476474	0.567913	0.327881	0.358823	0.084232	3.222118	1.535256
17	P19	1.162685	1.385812	0.222183	0.951318	0.221548	3.241802	3.769194
18	P20	0.303404	0.361629	1.0687	0.146664	0.077199	3.235821	0.98176
	total	0.284246			0.201256			

Table I-11 Accuracy Measures for PSI Calculation with Original FFTBM

Calculation		Window 0–100 s						
PSI	Variable	AA	VA	*I*	AMMIN	fraction A0	AA_{exp}	AA_{dif}
1	P1	0.14766	0.16296	0.542452	0.095731	0.03127	0.092367	0.013639
2	P2	0.126883	0.09242	0.220129	0.103992	0.380247	0.024468	0.003105
3	P3	0.068947	0.076091	0.248432	0.055227	0.039886	0.039266	0.002707
4	P4	0.08976	0.09906	0.397535	0.064227	0.091993	0.127714	0.011464
5	P5	0.093713	0.158858	0.312952	0.071376	0.065924	3.004864	0.281595
6	P6	0.12163	0.206182	0.376601	0.088355	0.059621	3.172731	0.385899
7	P7	0.22121	0.374986	0.570136	0.140886	0.081961	3.202652	0.708459
8	P8	0.032624	0.055303	0.304516	0.025009	0.257579	2.132043	0.069556
9	P9	0.489069	0.107949	0.403282	0.348518	0.019511	4.072386	1.991676
10	P10	0.85347	0.188381	0.71642	0.497239	0.010359	1.146323	0.978353
11	P11	0.056775	0.040602	0.280542	0.044336	0.025463	20.907	1.186987
12	P12	0.405337	0.289874	0.212755	0.334228	0.240104	30.52846	12.3743
13	P13	0.881032	0.238219	0.159404	0.759901	0.054513	0.810833	0.71437
14	P14	1.215099	0.328546	0.922855	0.631924	0.055339	0.827981	1.006079
15	P16	0.510844	0.608878	0.631375	0.313137	0.056652	7.176047	3.665839
16	P18	0.528446	0.629859	0.306697	0.404414	0.21699	3.222118	1.702716
17	P19	0.602311	0.717899	0.27882	0.47099	0.327835	3.241802	1.952574
18	P20	0.378195	0.450774	0.435791	0.263406	0.246335	3.235821	1.223772
	total	0.268158			0.19053			

Table I-12 Accuracy Measures for TAEK Calculation with Original FFTBM

Calculation		Window 0–100 s						
TAEK	Variable	AA	VA	*I*	AMMIN	fraction A0	AA_{exp}	AA_{dif}
1	P1	0.179764	0.198391	0.476459	0.121754	0.082956	0.092367	0.016604
2	P2	0.049388	0.035973	0.642136	0.030075	0.050785	0.024468	0.001208
3	P3	0.096723	0.106745	0.43694	0.067311	0.112476	0.039266	0.003798
4	P4	0.068056	0.075108	0.402615	0.048521	0.236249	0.127714	0.008692
5	P5	0.175827	0.298055	0.089808	0.161338	0.255299	3.004864	0.528338
6	P6	0.136296	0.231043	0.548814	0.088	0.177602	3.172731	0.432431
7	P7	0.257374	0.436289	0.620384	0.158835	0.18729	3.202652	0.824279
8	P8	0.026232	0.044467	0.324649	0.019803	0.23564	2.132043	0.055927
9	P9	0.426358	0.094107	0.201193	0.354946	0.009488	4.072386	1.736294
10	P10	0.635359	0.140239	0.717669	0.369896	0.021957	1.146323	0.728327
11	P11	0.192755	0.137847	0.173013	0.164324	0.374535	20.907	4.029919
12	P12	0.192629	0.137758	0.267693	0.151953	0.241804	30.52846	5.880677
13	P13	0.812102	0.219581	0.166089	0.696432	0.06482	0.810833	0.658479
14	P14	1.011509	0.273498	0.585951	0.637793	0.048901	0.827981	0.837511
15	P16	0.421822	0.502773	0.90702	0.221194	0.023937	7.176047	3.027016
16	P18	0.880803	1.049835	0.222529	0.720477	0.127582	3.222118	2.838052
17	P19	0.950797	1.133262	0.166418	0.815143	0.23468	3.241802	3.082296
18	P20	0.342909	0.408716	0.762272	0.194584	0.050909	3.235821	1.109594
	total	0.306871			0.226801			

Table I-13 Accuracy Measures for UPC Calculation with Original FFTBM

Calculation		Window 0–100 s						
UPC	Variable	AA	VA	*I*	AMMIN	fraction A0	AA_{exp}	AA_{dif}
1	P1	0.087652	0.096734	0.345105	0.065163	0.107984	0.092367	0.008096
2	P2	0.087159	0.063486	0.324746	0.065793	0.319884	0.024468	0.002133
3	P3	0.226689	0.250178	0.276748	0.177552	0.04034	0.039266	0.008901
4	P4	0.182109	0.200978	0.408911	0.129255	0.155198	0.127714	0.023258
5	P5	0.137164	0.232514	0.369824	0.100133	0.170392	3.004864	0.412159
6	P6	0.101093	0.171369	0.510111	0.066944	0.11158	3.172731	0.320741
7	P7	0.230268	0.390341	0.611579	0.142884	0.160767	3.202652	0.73747
8	P8	0.015379	0.026069	0.484579	0.010359	0.092063	2.132043	0.032788
9	P9	0.752199	0.166028	0.514547	0.49665	0.023455	4.072386	3.063246
10	P10	2.266162	0.500195	0.084873	2.088874	0.065808	1.146323	2.597754
11	P11	0.1259	0.090037	0.298696	0.096943	0.264601	20.907	2.632188
12	P12	0.192475	0.137647	0.153581	0.16685	0.400921	30.52846	5.875961
13	P13	0.923047	0.249579	0.065873	0.866001	0.066354	0.810833	0.748437
14	P14	0.891563	0.241066	0.495698	0.596085	0.034481	0.827981	0.738198
15	P16	0.359062	0.427969	1.406281	0.149219	0.064802	7.176047	2.576649
16	P18	0.233764	0.278625	0.524202	0.153368	0.11897	3.222118	0.753215
17	P19	0.958668	1.142643	0.254569	0.764141	0.166386	3.241802	3.107811
18	P20	0.234832	0.279898	0.905545	0.123236	0.046878	3.235821	0.759874
	total	0.274742			0.198579			

Table I-14 Accuracy Measures for UPI Calculation with Original FFTBM

Calculation		Window 0–100 s						
UPI	Variable	AA	VA	*I*	AMMIN	fraction A0	AA_{exp}	AA_{dif}
1	P1	0.120216	0.132673	0.431978	0.083951	0.016903	0.092367	0.011104
2	P2	0.029314	0.021352	0.517831	0.019313	0.006261	0.024468	0.000717
3	P3	0.070005	0.077258	0.550066	0.045162	0.014026	0.039266	0.002749
4	P4	0.115849	0.127853	0.394542	0.083073	0.132984	0.127714	0.014796
5	P5	0.094317	0.159883	0.348576	0.069938	0.103518	3.004864	0.283411
6	P6	0.091223	0.154638	0.617834	0.056386	0.034597	3.172731	0.289427
7	P7	0.231416	0.392287	0.713008	0.135093	0.12621	3.202652	0.741145
8	P8	0.024189	0.041004	0.310968	0.018451	0.251293	2.132043	0.051571
9	P9	0.480747	0.106112	0.28185	0.375042	0.003372	4.072386	1.957789
10	P10	0.893154	0.19714	0.80736	0.494176	0.007618	1.146323	1.023843
11	P11	0.090095	0.064431	0.367624	0.065877	0.031561	20.907	1.883613
12	P12	0.213088	0.152389	0.105864	0.192689	0.349853	30.52846	6.505258
13	P13	0.922732	0.249494	0.34446	0.686322	0.051861	0.810833	0.748182
14	P14	1.027638	0.277859	0.657101	0.620142	0.042326	0.827981	0.850865
15	P16	0.349301	0.416334	1.233852	0.156367	0.044769	7.176047	2.506601
16	P18	0.711032	0.847484	0.254864	0.566621	0.196289	3.222118	2.291029
17	P19	0.777408	0.926597	0.17537	0.661416	0.219534	3.241802	2.520202
18	P20	0.18975	0.226164	0.656954	0.114517	0.07239	3.235821	0.613996
	total	0.253942			0.179959			

II. FFTBM IMPROVED BY SIGNAL MIRRORING

Table II-1 Accuracy Measures for CEA Calculation with Improved FFTBM

Calculation		Window 0–100 s						
CEA	Variable	AA	VA	*I*	AMMIN	fraction A0	AA_{exp}	AA_{dif}
1	P1	0.217078	0.239571	0.004409	0.216125	0.009828	0.030982	0.006725
2	P2	0.083258	0.060644	0.183735	0.070335	0.250487	0.011973	0.000997
3	P3	0.293369	0.323767	0.082189	0.271088	0.27867	0.010416	0.003056
4	P4	0.236101	0.260566	0.159377	0.203645	0.10192	0.031674	0.007478
5	P5	0.096816	0.164119	0.269931	0.076238	0.015208	1.227415	0.118834
6	P6	0.332419	0.563503	0.345903	0.246986	0.082218	1.293564	0.430006
7	P7	0.411512	0.697577	0.261212	0.326283	0.187823	1.380685	0.568168
8	P8	0.025042	0.04245	0.208794	0.020717	0.366545	1.072209	0.02685
9	P9	0.404493	0.089281	0.079871	0.374576	0.024919	2.506108	1.013704
10	P10	0.959294	0.211739	0.225665	0.782673	0.000668	0.669841	0.642574
11	P11	0.324033	0.23173	0.050846	0.308354	0.316725	5.137662	1.66477
12	P12	0.378875	0.27095	0.032752	0.36686	0.394402	10.55885	4.000486
13	P13	1.020489	0.275926	0.242973	0.821007	0.037314	0.47675	0.486518
14	P14	1.464666	0.396026	0.372618	1.067061	0.026536	0.519373	0.760708
15	P16	0.587065	0.699727	0.586843	0.369958	0.090263	4.017688	2.358644
16	P18	0.708245	0.844162	0.210746	0.584966	0.095495	1.462038	1.035481
17	P19	1.036154	1.234999	0.330601	0.778712	0.083392	1.42883	1.480488
18	P20	0.329562	0.392808	0.751826	0.188125	0.010205	1.411689	0.46524
	total	0.388864			0.304954			

Table II-2 Accuracy Measures for GID Calculation with Improved FFTBM

Calculation		Window 0–100 s						
GID	Variable	AA	VA	*I*	AMMIN	fraction A0	AA_{exp}	AA_{dif}
1	P1	0.152882	0.168723	0.009392	0.15146	0.079911	0.030982	0.004737
2	P2	0.756896	0.551314	0.075386	0.703837	0.047759	0.011973	0.009062
3	P3	0.259394	0.286272	0.138593	0.22782	0.102356	0.010416	0.002702
4	P4	0.076336	0.084246	0.108052	0.068892	0.114713	0.031674	0.002418
5	P5	0.124295	0.2107	0.263936	0.09834	0.056783	1.227415	0.152562
6	P6	0.299833	0.508264	0.502203	0.199596	0.024628	1.293564	0.387853
7	P7	0.427034	0.72389	0.355929	0.314938	0.043733	1.380685	0.589599
8	P8	NA	NA	NA	NA	NA	NA	NA
9	P9	0.689477	0.152184	0.562348	0.441308	0.014017	2.506108	1.727904
10	P10	0.716096	0.158059	0.164501	0.614938	0.000495	0.669841	0.47967
11	P11	0.208714	0.149261	0.03474	0.201707	0.321718	5.137662	1.072302
12	P12	0.476698	0.340907	0.021141	0.466828	0.415799	10.55885	5.03338
13	P13	5.098523	1.378571	0.423321	3.582132	0.010052	0.47675	2.43072
14	P14	0.862333	0.233163	0.296508	0.665119	0.021092	0.519373	0.447872
15	P16	0.449621	0.535906	0.214428	0.370232	0.040818	4.017688	1.806435
16	P18	0.775937	0.924845	0.334348	0.58151	0.044704	1.462038	1.13445
17	P19	0.978951	1.166819	0.230327	0.795684	0.10227	1.42883	1.398755
18	P20	0.802917	0.957002	0.385336	0.579583	0.129891	1.411689	1.133469
	total	0.535556			0.465254			

Table II-3 Accuracy Measures for GRS Calculation with Improved FFTBM

Calculation		Window 0–100 s						
GRS	Variable	AA	VA	*I*	AMMIN	fraction A0	AA_{exp}	AA_{dif}
1	P1	0.102707	0.113349	0.015792	0.10111	0.007698	0.030982	0.003182
2	P2	0.056376	0.041064	0.031934	0.054632	0.179199	0.011973	0.000675
3	P3	0.092033	0.101569	0.284971	0.071623	0.083956	0.010416	0.000959
4	P4	0.083324	0.091957	0.090306	0.076422	0.149076	0.031674	0.002639
5	P5	0.134754	0.228428	0.216275	0.110792	0.125882	1.227415	0.165398
6	P6	0.483227	0.819145	0.230291	0.392774	0.057433	1.293564	0.625084
7	P7	0.515158	0.873273	0.48003	0.348073	0.131169	1.380685	0.711271
8	P8	0.01547	0.026224	0.101652	0.014042	0.111864	1.072209	0.016587
9	P9	1.098199	0.242398	0.651727	0.664879	0.02099	2.506108	2.752205
10	P10	2.498109	0.551391	0.723391	1.449531	0.006148	0.669841	1.673335
11	P11	0.088859	0.063547	0.040381	0.08541	0.353818	5.137662	0.456529
12	P12	0.357334	0.255545	0.025687	0.348385	0.232473	10.55885	3.773037
13	P13	0.662126	0.17903	0.080028	0.613063	0.061379	0.47675	0.315668
14	P14	0.909275	0.245855	0.138616	0.798579	0.021943	0.519373	0.472253
15	P16	0.701668	0.836323	0.321031	0.531152	0.07993	4.017688	2.819085
16	P18	1.554102	1.852345	0.240389	1.252915	0.17893	1.462038	2.272157
17	P19	1.473331	1.756073	0.273298	1.157098	0.232884	1.42883	2.105139
18	P20	0.490393	0.584503	0.568713	0.312609	0.086244	1.411689	0.692283
	total	0.492335			0.378836			

Table II-4 Accuracy Measures for IRSN Calculation with Improved FFTBM

Calculation		Window 0–100 s						
IRSN	Variable	AA	VA	*I*	AMMIN	fraction A0	AA_{exp}	AA_{dif}
1	P1	0.235697	0.260119	0.006346	0.234211	0.003287	0.030982	0.007302
2	P2	0.056081	0.040849	0.131183	0.049578	0.068507	0.011973	0.000671
3	P3	0.270075	0.298059	0.049104	0.257434	0.308223	0.010416	0.002813
4	P4	0.242685	0.267832	0.124584	0.2158	0.101941	0.031674	0.007687
5	P5	0.186169	0.315586	0.243579	0.149704	0.079387	1.227415	0.228507
6	P6	0.19956	0.338285	0.206586	0.165392	0.021594	1.293564	0.258143
7	P7	0.341547	0.578975	0.312638	0.260199	0.096746	1.380685	0.471568
8	P8	0.023827	0.04039	0.238122	0.019244	0.283747	1.072209	0.025547
9	P9	0.589887	0.130202	0.13881	0.517986	0.016115	2.506108	1.478321
10	P10	0.945894	0.208781	0.212455	0.780148	0.000517	0.669841	0.633598
11	P11	0.384426	0.27492	0.091785	0.352108	0.283148	5.137662	1.975051
12	P12	0.417615	0.298655	0.029504	0.405646	0.286539	10.55885	4.409531
13	P13	0.873574	0.236202	0.131077	0.772338	0.046499	0.47675	0.416476
14	P14	1.235288	0.334005	0.415539	0.872663	0.006021	0.519373	0.641575
15	P16	0.529863	0.631547	0.495309	0.35435	0.079155	4.017688	2.128823
16	P18	0.440464	0.524992	0.325993	0.332177	0.007222	1.462038	0.643976
17	P19	0.538057	0.641314	0.602165	0.335831	0.019726	1.42883	0.768792
18	P20	0.360991	0.430268	0.769491	0.204008	0.001292	1.411689	0.509607
	total	0.325055			0.253313			

Table II-5 Accuracy Measures for JNES Calculation with Improved FFTBM

Calculation		Window 0–100 s						
JNES	Variable	AA	VA	*I*	AMMIN	fraction A0	AA_{exp}	AA_{dif}
1	P1	0.234715	0.259036	0.007132	0.233053	0.067027	0.030982	0.007272
2	P2	0.203477	0.14821	0.008609	0.20174	0.396756	0.011973	0.002436
3	P3	0.361335	0.398776	0.530478	0.236093	0.191341	0.010416	0.003764
4	P4	0.306673	0.33845	0.20226	0.25508	0.106511	0.031674	0.009714
5	P5	0.278829	0.47266	0.398924	0.199317	0.002907	1.227415	0.342239
6	P6	0.289532	0.490801	0.410116	0.205325	0.031675	1.293564	0.374528
7	P7	0.363222	0.615718	0.397462	0.259916	0.07173	1.380685	0.501495
8	P8	0.043185	0.073206	0.092498	0.039529	0.54979	1.072209	0.046304
9	P9	0.82305	0.181667	0.132567	0.726712	0.015804	2.506108	2.062653
10	P10	1.70166	0.375596	1.153259	0.790272	0.025938	0.669841	1.139841
11	P11	0.206094	0.147387	0.121733	0.183729	0.016577	5.137662	1.058844
12	P12	0.337515	0.241372	0.038662	0.324952	0.395048	10.55885	3.563772
13	P13	0.683345	0.184767	0.142757	0.59798	0.061508	0.47675	0.325785
14	P14	0.904649	0.244605	0.253813	0.721519	0.063851	0.519373	0.46985
15	P16	0.493337	0.588012	0.234211	0.399718	0.072699	4.017688	1.982074
16	P18	0.667397	0.795474	0.310381	0.509315	0.129666	1.462038	0.975759
17	P19	1.215663	1.448957	0.323824	0.918296	0.161194	1.42883	1.736975
18	P20	0.672203	0.801203	0.529314	0.439545	0.162919	1.411689	0.948942
	total	0.433661			0.327613			

Table II-6 Accuracy Measures for KAERI Calculation with Improved FFTBM

Calculation		Window 0–100 s						
KAERI	Variable	AA	VA	*I*	AMMIN	fraction A0	AA_{exp}	AA_{dif}
1	P1	0.165778	0.182956	0.010205	0.164104	0.070337	0.030982	0.005136
2	P2	0.045964	0.03348	0.053939	0.043612	0.028652	0.011973	0.00055
3	P3	0.204975	0.226214	0.256026	0.163194	0.165934	0.010416	0.002135
4	P4	0.158587	0.17502	0.058983	0.149754	0.15422	0.031674	0.005023
5	P5	0.123417	0.209211	0.196049	0.103187	0.121275	1.227415	0.151483
6	P6	0.159827	0.270931	0.259798	0.126867	0.073856	1.293564	0.206746
7	P7	0.322978	0.547498	0.217954	0.265181	0.127323	1.380685	0.445931
8	P8	0.026363	0.044689	0.369041	0.019257	0.112612	1.072209	0.028267
9	P9	0.660725	0.145837	0.734014	0.381038	0.012213	2.506108	1.655847
10	P10	0.291021	0.064235	0.052877	0.276405	0.05251	0.669841	0.194937
11	P11	0.384827	0.275207	0.046604	0.367691	0.223928	5.137662	1.97711
12	P12	0.430634	0.307965	0.027964	0.41892	0.382188	10.55885	4.547001
13	P13	0.889928	0.240624	0.111863	0.800393	0.059074	0.47675	0.424273
14	P14	1.200857	0.324695	0.600688	0.750213	0.009161	0.519373	0.623693
15	P16	0.312883	0.372928	0.313324	0.238238	0.073027	4.017688	1.257068
16	P18	0.315898	0.376521	0.649973	0.191457	0.042325	1.462038	0.461855
17	P19	0.411059	0.489944	0.454187	0.282673	0.007577	1.42883	0.587334
18	P20	0.343449	0.40936	0.487809	0.230842	0.022193	1.411689	0.484844
	total	0.260962			0.204529			

Table II-7 Accuracy Measures for KFKI Calculation with Improved FFTBM

Calculation		Window 0–100 s						
KFKI	Variable	AA	VA	*I*	AMMIN	fraction A0	AA_{exp}	AA_{dif}
1	P1	0.109811	0.12119	0.0156	0.108125	0.02927	0.030982	0.003402
2	P2	0.05727	0.041715	0.021288	0.056077	0.158941	0.011973	0.000686
3	P3	0.128502	0.141817	0.203915	0.106737	0.124928	0.010416	0.001338
4	P4	0.088517	0.097689	0.082414	0.081777	0.178546	0.031674	0.002804
5	P5	0.136813	0.23192	0.202886	0.113738	0.147929	1.227415	0.167927
6	P6	0.164992	0.279687	0.182619	0.139514	0.045582	1.293564	0.213428
7	P7	0.355601	0.602799	0.16443	0.305386	0.103556	1.380685	0.490973
8	P8	0.01322	0.02241	0.039803	0.012714	0.083843	1.072209	0.014174
9	P9	0.64922	0.143298	0.503312	0.43186	0.00769	2.506108	1.627014
10	P10	0.550214	0.121445	0.271876	0.4326	0.00474	0.669841	0.368556
11	P11	0.107047	0.076554	0.02518	0.104418	0.349051	5.137662	0.54997
12	P12	0.350334	0.25054	0.027476	0.340966	0.360853	10.55885	3.699129
13	P13	0.468138	0.126578	0.11993	0.418006	0.081636	0.47675	0.223185
14	P14	1.122835	0.303599	0.339769	0.838081	0.042465	0.519373	0.58317
15	P16	0.421431	0.502306	0.215487	0.346718	0.039217	4.017688	1.693177
16	P18	1.193997	1.423133	0.224253	0.975286	0.136476	1.462038	1.745669
17	P19	1.400923	1.66977	0.28939	1.0865	0.169533	1.42883	2.001681
18	P20	0.597556	0.71223	0.616824	0.369586	0.069142	1.411689	0.843563
	total	0.381593			0.305385			

Table II-8 Accuracy Measures for KINS Calculation with Improved FFTBM

Calculation		Window 0–100 s						
KINS	Variable	AA	VA	*I*	AMMIN	fraction A0	AA_{exp}	AA_{dif}
1	P1	0.317655	0.350569	0.002546	0.316848	0.044607	0.030982	0.009842
2	P2	0.079056	0.057584	0.043129	0.075788	0.033956	0.011973	0.000947
3	P3	0.22585	0.249251	0.248442	0.180905	0.194921	0.010416	0.002352
4	P4	0.111122	0.122636	0.078417	0.103042	0.176877	0.031674	0.00352
5	P5	0.580557	0.984135	0.173003	0.494932	0.214205	1.227415	0.712585
6	P6	0.167504	0.283946	0.140649	0.14685	0.066083	1.293564	0.216677
7	P7	0.327375	0.554951	0.180274	0.277372	0.122177	1.380685	0.452001
8	P8	0.021824	0.036996	0.08172	0.020176	0.142292	1.072209	0.0234
9	P9	0.352896	0.077892	0.078206	0.327299	0.030688	2.506108	0.884395
10	P10	1.085341	0.23956	0.176149	0.922792	0.007333	0.669841	0.727006
11	P11	0.320825	0.229436	0.099931	0.291677	0.254602	5.137662	1.648288
12	P12	0.462025	0.330414	0.0252	0.450668	0.473908	10.55885	4.878453
13	P13	0.856764	0.231657	0.093153	0.783755	0.05925	0.47675	0.408462
14	P14	1.023401	0.276714	0.200158	0.852722	0.028008	0.519373	0.531527
15	P16	0.436387	0.520132	0.184446	0.368431	0.071305	4.017688	1.753266
16	P18	0.510322	0.608256	0.334138	0.38251	0.030896	1.462038	0.74611
17	P19	0.714421	0.851524	0.571506	0.454609	0.116243	1.42883	1.020787
18	P20	0.544067	0.648477	0.736152	0.313375	0.096578	1.411689	0.768053
	total	0.369674			0.298348			

Table II-9 Accuracy Measures for NRI-K Calculation with Improved FFTBM

Calculation		Window 0–100 s						
NRI-K	Variable	AA	VA	*I*	AMMIN	fraction A0	AA_{exp}	AA_{dif}
1	P1	0.231934	0.255966	0.003611	0.231099	0.000502	0.030982	0.007186
2	P2	0.070055	0.051027	0.093947	0.064038	0.049882	0.011973	0.000839
3	P3	0.163319	0.180242	0.082049	0.150935	0.010313	0.010416	0.001701
4	P4	0.129155	0.142538	0.152692	0.112046	0.090647	0.031674	0.004091
5	P5	0.095342	0.16162	0.173595	0.081239	0.032186	1.227415	0.117024
6	P6	0.148113	0.251075	0.28586	0.115186	0.006639	1.293564	0.191594
7	P7	0.338836	0.57438	0.355519	0.249968	0.083589	1.380685	0.467826
8	P8	0.024549	0.041615	0.018799	0.024096	0.251061	1.072209	0.026322
9	P9	0.357502	0.078909	0.069394	0.334303	0.000105	2.506108	0.895938
10	P10	0.54551	0.120407	0.155233	0.472208	0.00655	0.669841	0.365405
11	P11	0.078908	0.056431	0.191458	0.066228	0.011207	5.137662	0.405404
12	P12	0.237139	0.169589	0.047789	0.226324	0.302676	10.55885	2.50392
13	P13	0.908611	0.245676	0.133656	0.801488	0.050479	0.47675	0.43318
14	P14	1.02472	0.27707	0.144958	0.894985	0.0331	0.519373	0.532212
15	P16	0.554021	0.660341	0.598595	0.346567	0.077782	4.017688	2.225882
16	P18	0.988613	1.178335	0.146279	0.862454	0.119195	1.462038	1.445391
17	P19	1.201202	1.431721	0.172229	1.024716	0.165088	1.42883	1.716314
18	P20	0.738962	0.880773	0.409639	0.524221	0.142416	1.411689	1.043184
	total	0.375429			0.306813			

Table II-10 Accuracy Measures for NRI-M Calculation with Improved FFTBM

Calculation		Window 0–100 s						
NRI-M	Variable	AA	VA	*I*	AMMIN	fraction A0	AA_{exp}	AA_{dif}
1	P1	0.221764	0.244743	0.003725	0.220941	0.007951	0.030982	0.006871
2	P2	0.051813	0.03774	0.032779	0.050169	0.060807	0.011973	0.00062
3	P3	0.10131	0.111807	0.203628	0.08417	0.080544	0.010416	0.001055
4	P4	0.081244	0.089663	0.074884	0.075584	0.186168	0.031674	0.002573
5	P5	0.137078	0.232369	0.113466	0.12311	0.166852	1.227415	0.168252
6	P6	0.536165	0.908884	0.363738	0.393158	0.080354	1.293564	0.693564
7	P7	0.332437	0.563532	0.328688	0.250199	0.008541	1.380685	0.45899
8	P8	0.014006	0.023743	0.112566	0.012589	0.110891	1.072209	0.015018
9	P9	0.46617	0.102895	0.061962	0.438971	0.012454	2.506108	1.168272
10	P10	0.837258	0.184802	0.271875	0.658286	0.001687	0.669841	0.560829
11	P11	0.092589	0.066215	0.111757	0.083282	0.153003	5.137662	0.475694
12	P12	0.30351	0.217053	0.034148	0.293488	0.323384	10.55885	3.204716
13	P13	0.882434	0.238598	0.106269	0.797667	0.0424	0.47675	0.4207
14	P14	1.005855	0.271969	0.153257	0.872187	0.029502	0.519373	0.522414
15	P16	0.379748	0.452624	0.246143	0.304738	0.073544	4.017688	1.525707
16	P18	0.645308	0.769147	0.229737	0.524753	0.068667	1.462038	0.943465
17	P19	1.723486	2.054234	0.214571	1.419007	0.169881	1.42883	2.462568
18	P20	0.442652	0.5276	0.50875	0.29339	0.060762	1.411689	0.624887
	total	0.394312			0.320563			

Table II-11 Accuracy Measures for PSI Calculation with Improved FFTBM

Calculation		Window 0–100 s						
PSI	Variable	AA	VA	*I*	AMMIN	fraction A0	AA_{exp}	AA_{dif}
1	P1	0.272856	0.301128	0.002682	0.272126	0.025274	0.030982	0.008454
2	P2	0.132016	0.096159	0.120966	0.11777	0.374163	0.011973	0.001581
3	P3	0.153491	0.169395	0.241797	0.123604	0.033836	0.010416	0.001599
4	P4	0.232175	0.256233	0.27091	0.182684	0.071841	0.031674	0.007354
5	P5	0.12594	0.213489	0.257063	0.100186	0.060163	1.227415	0.154581
6	P6	0.176784	0.299676	0.169029	0.151223	0.050404	1.293564	0.228681
7	P7	0.331512	0.561965	0.201261	0.27597	0.063554	1.380685	0.457714
8	P8	0.029767	0.050459	0.082643	0.027494	0.281223	1.072209	0.031916
9	P9	0.507266	0.111966	0.099348	0.461425	0.015314	2.506108	1.271264
10	P10	0.898958	0.198421	0.279003	0.702859	0.008432	0.669841	0.602159
11	P11	0.122245	0.087423	0.09553	0.111585	0.024109	5.137662	0.628052
12	P12	0.343884	0.245927	0.03413	0.332535	0.409928	10.55885	3.631019
13	P13	0.911855	0.246553	0.129562	0.807264	0.044877	0.47675	0.434727
14	P14	1.198659	0.324101	0.315725	0.911025	0.044803	0.519373	0.622551
15	P16	0.571915	0.68167	0.390346	0.411347	0.045279	4.017688	2.297776
16	P18	0.757719	0.90313	0.373082	0.551838	0.167083	1.462038	1.107814
17	P19	0.865622	1.031741	0.411218	0.613386	0.25928	1.42883	1.236827
18	P20	0.563088	0.671149	0.422234	0.395918	0.189988	1.411689	0.794906
	total	0.358366			0.28083			

Table II-12 Accuracy Measures for TAEK Calculation with Improved FFTBM

Calculation		Window 0–100 s						
TAEK	Variable	AA	VA	*I*	AMMIN	fraction A0	AA_{exp}	AA_{dif}
1	P1	0.331574	0.365931	0.002442	0.330766	0.067173	0.030982	0.010273
2	P2	0.058826	0.042848	0.055888	0.055713	0.043652	0.011973	0.000704
3	P3	0.233364	0.257545	0.227311	0.190143	0.088041	0.010416	0.002431
4	P4	0.168228	0.185659	0.054797	0.159488	0.193061	0.031674	0.005328
5	P5	0.185449	0.314366	0.116911	0.166038	0.296866	1.227415	0.227623
6	P6	0.206096	0.349365	0.083765	0.190167	0.144319	1.293564	0.266599
7	P7	0.372284	0.631079	0.162655	0.320202	0.150465	1.380685	0.514007
8	P8	0.023816	0.040371	0.069191	0.022274	0.25855	1.072209	0.025535
9	P9	0.448123	0.098911	0.063146	0.421507	0.007349	2.506108	1.123044
10	P10	0.659074	0.145473	0.133414	0.581495	0.018147	0.669841	0.441475
11	P11	0.312652	0.223591	0.027238	0.304362	0.470736	5.137662	1.606301
12	P12	0.365564	0.261431	0.082948	0.337563	0.184556	10.55885	3.859931
13	P13	0.861712	0.232995	0.059747	0.81313	0.052049	0.47675	0.410821
14	P14	1.015	0.274442	0.170522	0.867134	0.03892	0.519373	0.527164
15	P16	0.493706	0.588452	0.259324	0.392041	0.0183	4.017688	1.983557
16	P18	1.215473	1.44873	0.197323	1.015159	0.102076	1.462038	1.777067
17	P19	1.354052	1.613904	0.286065	1.052865	0.187305	1.42883	1.934711
18	P20	0.4974	0.592854	0.396076	0.356284	0.040302	1.411689	0.702174
	total	0.425997			0.359303			

Table II-13 Accuracy Measures for UPC Calculation with Improved FFTBM

Calculation		Window 0–100 s						
UPC	Variable	AA	VA	*I*	AMMIN	fraction A0	AA_{exp}	AA_{dif}
1	P1	0.164587	0.181641	0.010221	0.162922	0.085892	0.030982	0.005099
2	P2	0.09564	0.069663	0.029089	0.092936	0.298459	0.011973	0.001145
3	P3	0.355136	0.391934	0.166209	0.304522	0.048631	0.010416	0.003699
4	P4	0.463952	0.512026	0.123148	0.413082	0.123054	0.031674	0.014695
5	P5	0.212457	0.360147	0.302364	0.163132	0.134917	1.227415	0.260772
6	P6	0.156388	0.265103	0.129517	0.138456	0.088627	1.293564	0.202298
7	P7	0.338232	0.573356	0.217379	0.277836	0.127188	1.380685	0.466992
8	P8	0.017124	0.029028	0.061436	0.016133	0.082363	1.072209	0.018361
9	P9	0.778733	0.171885	0.279822	0.608469	0.018443	2.506108	1.951588
10	P10	2.147637	0.474034	0.054002	2.037603	0.059533	0.669841	1.438575
11	P11	0.240529	0.172013	0.150553	0.209055	0.282353	5.137662	1.235757
12	P12	0.286608	0.204966	0.027572	0.278918	0.389985	10.55885	3.026252
13	P13	0.923863	0.2498	0.059923	0.871632	0.056486	0.47675	0.440451
14	P14	0.884488	0.239153	0.185736	0.74594	0.027758	0.519373	0.459379
15	P16	0.40384	0.48134	0.298248	0.311065	0.051555	4.017688	1.622503
16	P18	0.321711	0.383449	0.347969	0.238663	0.095444	1.462038	0.470353
17	P19	1.360614	1.621726	0.166391	1.166517	0.133251	1.42883	1.944087
18	P20	0.352381	0.420006	0.524959	0.231076	0.035873	1.411689	0.497453
	total	0.377848			0.318913			

Table II-14 Accuracy Measures for UPI Calculation with Improved FFTBM

Calculation		Window 0–100 s						
UPI	Variable	AA	VA	*I*	AMMIN	fraction A0	AA_{exp}	AA_{dif}
1	P1	0.218847	0.241523	0.003475	0.218089	0.013868	0.030982	0.00678
2	P2	0.037899	0.027605	0.052458	0.03601	0.004958	0.011973	0.000454
3	P3	0.130647	0.144184	0.125518	0.116077	0.014194	0.010416	0.001361
4	P4	0.275549	0.3041	0.188389	0.231867	0.112939	0.031674	0.008728
5	P5	0.133828	0.226859	0.200889	0.111441	0.089477	1.227415	0.164262
6	P6	0.142247	0.24113	0.106877	0.128512	0.027262	1.293564	0.184005
7	P7	0.341735	0.579294	0.188683	0.28749	0.099319	1.380685	0.471828
8	P8	0.023329	0.039547	0.022238	0.022822	0.259552	1.072209	0.025014
9	P9	0.500574	0.110488	0.080581	0.463245	0.002636	2.506108	1.254493
10	P10	0.956947	0.211221	0.211551	0.789853	0.006096	0.669841	0.641002
11	P11	0.187863	0.134349	0.056761	0.177773	0.030857	5.137662	0.965179
12	P12	0.281422	0.201257	0.039184	0.27081	0.3837	10.55885	2.971489
13	P13	0.968259	0.261804	0.209952	0.800246	0.04211	0.47675	0.461617
14	P14	1.028306	0.27804	0.187316	0.866076	0.033782	0.519373	0.534074
15	P16	0.376762	0.449065	0.488415	0.25313	0.03714	4.017688	1.513712
16	P18	0.98083	1.169058	0.320347	0.742858	0.157105	1.462038	1.434011
17	P19	1.005378	1.198317	0.237849	0.812197	0.192949	1.42883	1.436514
18	P20	0.271297	0.32336	0.137742	0.238452	0.05814	1.411689	0.382987
	total	0.341178			0.281724			